Università degli Studi di Salerno

DIPARTIMENTO DI FISICA E. R. CAIANIELLO

Dottorato di Ricerca in Matematica,Fisica ed Applicazioni

PhD Thesis in Physics

Unveiling spin-orbit coupling effects on the electronic states of multi-orbital Transition Metal Oxides

Delia Guerra

Advisors:

Prof. Canio Noce

Dr. Filomena Forte

Phd School Coordinator:

Prof. Roberto Scarpa

Alle donne della mia vita:

mia mamma Titti e mia sorella Edda

Abstract

Transition Metal Oxides (TMOs) show a wealth of intriguing properties which are governed by the interplay of charge, spin, and orbital degrees of freedom. Moreover, the comprehension of the features of strongly correlated TMOs with significant Spin Orbit Coupling (SOC) represents a challenging work and the interplay between large SOC and lattice geometry is undoubtedly a relevant ingredient in the exploration of such features. The most dramatic example of that occurs in iridates, where SOC deeply impacts the magnetic state, changing the character of the multiplet state within the t_{2g} manifold in the case of an octahedral arrangement of the ions. Corresponding effects in e_g manifold have rarely been considered, due to the conventional wisdom that e_g subshells ensure a perfectly quenched orbital momentum.
In the first part of the thesis, we study the influence of SOC on the magnetic state of a d^1 TM ion located in a tetrahedral environment, proving that its effect can be strongly enhanced in the case of distorted geometry. Under this condition, our theoretical research reveals that SOC can induce a substantial anisotropic unquenched orbital angular momentum and can affect the hierarchy of the lowest energy levels involved in the magnetic superexchange.
Since particular geometries can give rise to novel SOC effects, the structure

of the insulating compound $KOsO_4$, whose Os^{7+} ions are characterized by an e^1 configuration, seems to be particularly relevant for our study. $KOsO_4$ crystallizes in a scheelite-like structure, consisting in isolated and quite distorted tetrahedra; the isolated tetrahedra imply a reduction of the hopping connectivity and, as a consequence, the effects of the local energy scales are emphasized. Furthermore, the Os ions are covalently bonded to the oxygens in a tetrahedral configuration, which is distorted. The competition between strong electronic correlations, SOC and tetrahedral deformations has been analyzed through a study based on an exact diagonalization approach, which allows to completely characterize the local magnetic moment and the nature of the static spin/orbital correlations over finite clusters. Our study reveals that an entangled spin-orbital state emerges, marked by a strong anisotropy. Moreover, results show a link between the bond direction and the sign of the superexchange coupling per spin component, which reminds a Kitaev-like coupling.

The choice of a specific geometry may enhance the influence of SOC on the magnetic state of a system. However, there are also other strategies in order to emphasize the effects of the SOC; one of them is to lower the connectivity, thus enhancing the interplay between the local energy scales, which include SOC. In the second part of the thesis, we consider a trilayered structure composed by TM ions stacked in the z direction, where the hopping connectivity is highly damped. The tight-binding Hamiltonian model which describes the trilayer shows both time-reversal and inversion symmetries, which ensure the Kramer's degeneracy of its eigenstates, and a layer-interchange symmetry, related to the particular structure of the system. We analyze the evolution

and eventually the closing of the energy gaps of the trilayer, opening the possibility to find novel topological nodal semimetals, which are protected by the layer-interchange symmetry. We simulate different local environment by modifying the value of the parameters of the model, verifying that transitions between different topological configurations occur in the limit of weak and strong SOC regime.

Acknowledgements

The PhD has been a life path for me, it has given me the opportunity to learn lot of things, not only related to the physics research. At the end of this journey, I would like to thank all the people who supported me, directly or not, in making this final work.

I think that in these last three years I have had the opportunity to collaborate with the excellence of the Physics Department of Salerno University: I would like to express my profound gratitude to my advisor Prof. Canio Noce for his patience, for his constant motivation, for his paternal advices and for his immense knowledge, which has always been for me a source of improvement.

I would like to thank my advisor Dr. Fiona Forte for her strong support and her impeccable guidance, which helped me during the whole research and writing of this thesis: I am in debt with her, because everything I have learned I owe to her.

Beside my advisors, I would like to thank Prof. Ileana Rabuffo, with whom I started my teaching experience at Salerno University, for her precious comments, her unmistakable style in the teaching of Physics and also for her emotional sensitivity in my regards. I would like to thank Prof. Roberta Citro: all the Training Courses in Vietri organized by her will remain in my

mind and in my heart as beautiful experiences. I would like to thank Dr. Mario Cuoco for his advices and for his support in the realization of the last chapter of the thesis. Finally, I thank the reviewers of this thesis work, Dr. Paola Gentile and Dr.Paolo Barone, for all the improvements and food for thought.

I thank my fellow labmates Antonella, Gaetano, Giulio, Maria Vittoria and Vittorio for the stimulating discussions and for their psychological and technical support: among other things, this thesis is written in Latex also thanks to them! I thank also my best friend Gabriella for her essential support. Although it can be considered unusual, I thank my four-legged friends Naní, Monet, Brera, Schopy, Giulietta and Sidera: they give me much more than everyone can imagine.

Last, but not least, I would like to thank my amazing family: I thank my sister for always being next to me in all the phases of my life, I thank my mum for all that she taught me and for giving me the opportunity to get where I am now: you are both the most beautiful gift that life could give me. I thank also all my family members who are not physically here: my granmothers, my dad and my daddy, because what I am also owe to them.

I think that any comment would be reductive for them: I love you all, this important goal is mine as yours!

Contents

Chapter 1

Introduction

1.1 Electronic correlations and spin-orbit coupling in transition metal oxides

In the last years, Transition Metal Oxides (TMOs) have been one of the main topics of the solid state research since they represent a paradigmatic example of complex materials: the subtle interplay between charge, spin and orbital lattice degrees of freedom which characterizes these compounds is the reason why many of the usual theoretical simplifications are not applicable [1]. Most of TMOs are characterized by partially filled d orbitals and by multiple valence states; furthermore, they manifest a rich variety of phase transitions and an extreme sensitivity to intrinsic or external perturbations, all linked to an amazing "tunability" of ground state properties. TMOs show also unusual features related to the details of the structure of the atoms or ions and many different structures can be realized with them, such as layered ones. Last,

but not least, TMOs are at the center of an intense investigation because of their possible applications in electronic and sensing devices[2]: the rich variety of highly diversified ground states and the complex interplay between the different degrees of freedom open the way to the possibility of tuning the device response as function of the external perturbation in unexpected ways. TMOs possess puzzling properties which are still matter of study to the present day: unconventional superconductivity with high critical temperature (high-T_c) [3] is one of them and it still remains to be understood; other remarkable phenomena include colossal magnetoresistance [4], the occurrence of exciting magnetic and non-magnetic phases such as the spin-orbital liquids, which are strongly correlated states of matter that emerge from quantum frustration between spin and orbital degrees of freedom [5], and also phase transitions which include, for example, the metal insulator transition [6]. All the above mentioned phenomena are a direct consequence of strong electronic correlations which characterize the TMOs; these are due to the large on-site Coulomb and exchange interactions among the TM valence electrons. The hallmark of the strong correlation is the presence of unusual insulating properties (referred as "Mott physics") which cannot be understood in terms of the standard band-theory of solids. Many $3d$ TMOs show in fact an insulating behavior even though the valence shells are partially filled. The large U leads to the formation of magnetic moments at each of the TM lattice sites and the interactions between these moments, which can be ferromagnetic (FM) or antiferromagnetic (AFM), give rise to fascinating magnetic orbital phases either with or without long-range order [7].

Beside $3d$ TMOs, relevant attention has been focused on the $4d$ and $5d$ com-

pounds, which are characterized by more extended orbitals than $3d$'s and, as a consequence, a reduced on-site Coulomb interaction strength. The most relevant feature of these elements is that they are characterized by a stronger intrinsic spin-orbit coupling than $3d$'s. Spin-orbit coupling (SOC) is a relativistic effect which couples the spin and the orbital momentum of electrons and it has been shown that it stabilizes new exotic states of matter. The most striking example of this new physics is constituted by the topological insulators: these systems are insulating in the bulk, but have interesting metallic "edge states" on their surface [8] originating from the combined effect of strong spin-orbit interaction and the electronic band structure. SOC is usually considered as a small perturbation in the discussion of electrons in solids, however in heavy elements it needs not to be weak, since it increases proportionally to Z^4, where Z is the atomic number. In Fig. 1.1, there is a schematic representation of the energy scales of the major interactions of TMOs. In $3d$ TMOs, which have been the traditional playground for the study of correlated electron physics, SOC is much smaller than the Coulomb interaction U and can be considered as a perturbation; on the right part of the Figure 1.1 it is evident that, considering $5d$ TMOs, the energy scales of U, SOC and crystal field D are comparable. Upon descending the periodic table from $3d$ to $4d$ to the $5d$ series, there are several competing trends since U and SOC meets on the same energy scale and several intriguing phenomena arises. The research is currently open and the experimental evidences and theoretical perspectives allow to describe a picture which is summed up in terms of correlation strength U and SOC λ, scaled to the typical kinetic energy scale t, in the phase diagram of Fig. 1.2 [9]. Con-

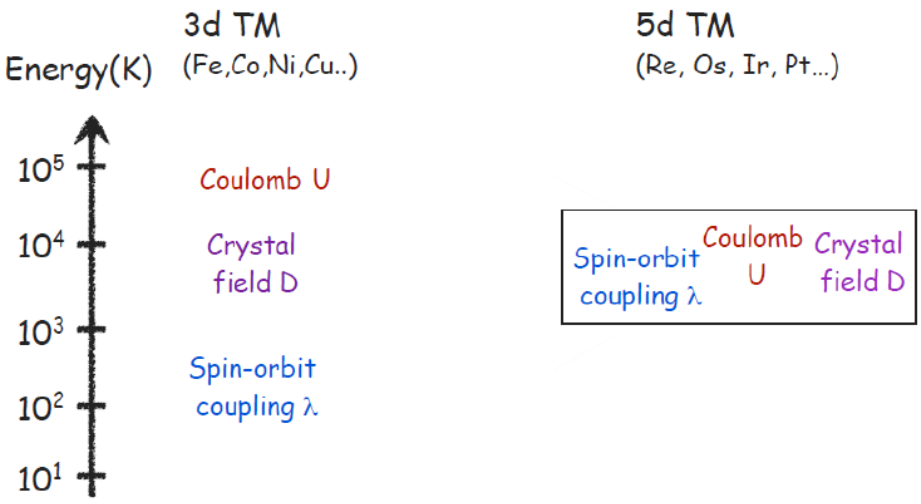

Figure 1.1: Schematic representation of the competing energy scales in TMOs; in $3d$ TMOs (left), the Coulomb interaction U is dominating on the other microscopic mechanisms, while in $5d$ compounds (right) these energy scales are comparable.

ventional oxide materials composed by $3d$ TM reside on the left-hand side of the diagram, where SOC is weak and a metal-insulator transition associated with the paradigmatic Mott physics may occur when U is comparable to the bandwidth. Upon increasing λ, a metallic or semiconducting state at small U may be converted to a semimetal or a topological insulator. When both U and λ are present, several arguments [10, 11] suggest that they tend to cooperate rather than compete in generating insulating states. Furthermore, U opens up possibilities for new types of topological phases For sizable SOC, topological Mott insulating phases emerge whose full characterization is still matter of investigation and debate [12, 13]. In general,in the limit of strong λ we can distinguish two specific regimes; the first is characterized by weak or intermediate correlations, where electrons remain delocalized enough

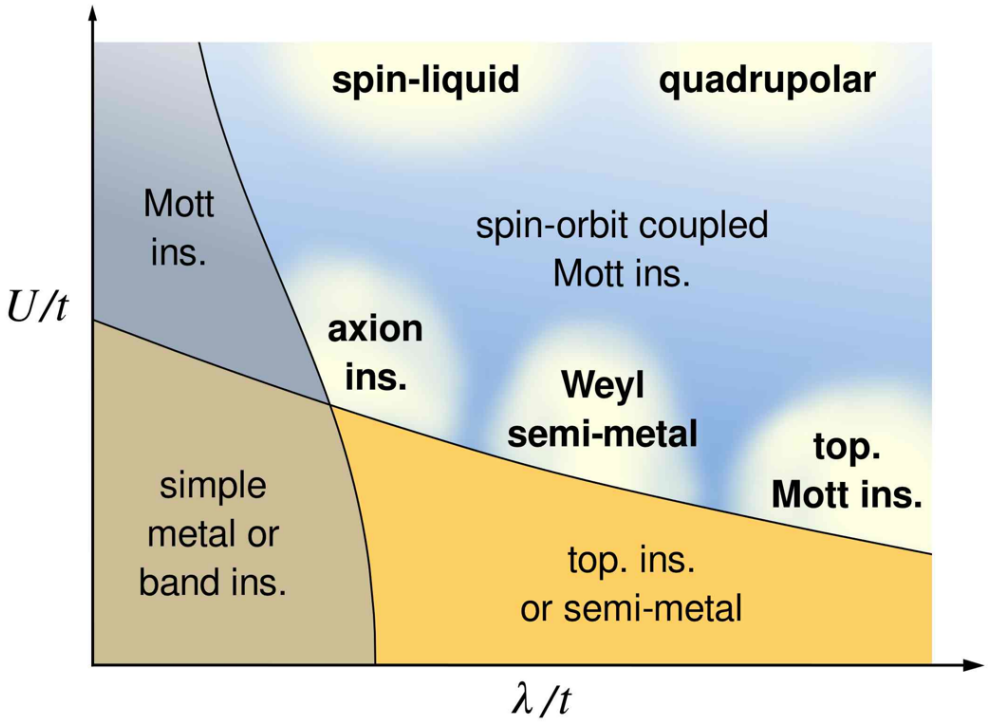

Figure 1.2: Generic phase diagram for TMOs; the x axis represents the SOC parameter λ while the y axis is constituted by electronic correlations U, both expressed in unit of kinetic energy t. The figure has been taken from Ref. [9]

and band topology continues to play an important role. In this region, new types of topological phases emerge: they include Weyl semimetals or axion insulators, which can arise in the presence of spontaneous magnetic order. The pyroclore iridates, for example, belong to this regime: these compounds comprise a large family for which experiments have revealed thermal phase transitions and evolution from metallic to insulating states and many key theoretical ideas have been introduced, including topological Mott insulators [8, 14], Weyl semimetals [15] and axion insulators [16].

The second regime is constituted by the strong Mott limit, where $\frac{U}{t}$ is large and electron band topology no longer plays a role, because the electronic

states are not extended. One can observe that insulating states may be obtained in the intermediate regime from the combined influence of SOC and correlations: these may be considered spin-orbit assisted Mott insulators [17], where the term "Mott" denotes any state which is insulating by virtue of electronic correlations. In this context, SOC still offers new physics by fully or partially lifting the orbital degeneracy of partially filled d shells by entangling the orbital and spin degrees of freedom. This provides a distinct mechanism to avoid the Jahn Teller effect and classical orbital ordering. The orbital degeneracy may be fully lifted by SOC, as it happens in iridates in the strong Mott and strong SOC limit, or partially lifted, which is the case of many d^1 or d^2 ions. An example of the former is constituted by honeycomb iridates [18, 19], while double perovskites [20, 21] is an example of the latter; in either cases, strong SOC results in strong anisotropic exchange interactions and, for the case of partial degeneracy lifting, these have an highly non-trivial multipolar nature. These unusual interactions can promote large quantum fluctuations and lead to novel quantum ground states which are not possible without SOC: quantum spin liquid and quadrupolar (spin orbital coupled) ordered phases have been suggested to occur in this regime [22, 23]. $4d$ and $5d$ TM belong to this region, which is not only difficult to access from a theoretical and computational point of view but also for materials science perspectives to synthetize compounds exhibiting microscopic conditions with both large U and λ.

1.2 Motivation of the Thesis

It is clear that heavy TMOs, which are characterized by significant SOC, are a challenging problem, since the correlations effects are often of intermediate or large strength, making them competitive with those of SOC. Particular attention has been focused on $5d$ TMOs, since the overlapping energy scales and competing interactions offer wide-ranging opportunities for the discovery of new physics and also new device paradigms.

At single ion level, SOC may greatly simplify the multiplet description by fully lifting the orbital degeneracy. The most dramatic example of the relevance of such SOC effect in $5d$ TMOs occurs in iridates: considering a TMO_6 octahedron, for example, the $5d$ states are split into t_{2g} and e_g orbital states by the crystal field energy and, in general, this energy is sufficiently large to yield a t_{2g} ground state. SOC is responsible to change the character of the multiplet state within the t_{2g} manifold as it has been intensively studied for TMOs containing Ir^{4+} : in these compounds, strong SOC split the t_{2g} band into an effective total angular momentum $J_{eff} = \frac{1}{2}$ doublet and $J_{eff} = \frac{3}{2}$ quartet, as it is shown in Fig.1.3 [17]. Since Ir^{4+} ions provide five

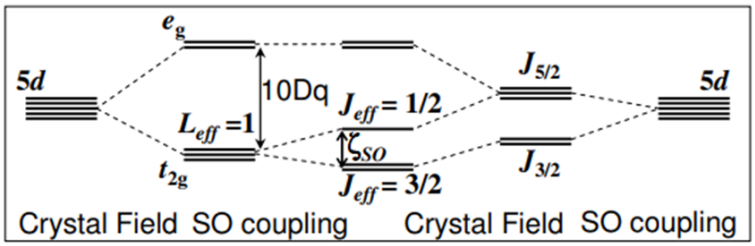

Figure 1.3: Splitting of the $5d$ levels due to CF and SOC

$5d$ electrons to bonding states, four of them fill $J_{eff} = \frac{3}{2}$ band and one re-

maining electron fills the $J_{eff} = \frac{1}{2}$ band,reducing the system to an effective Kramers doublet with $J_{eff} = \frac{1}{2}$. In addition, a relevant consideration is that even a small U opens a Mott gap: this explains why these compounds can be insulating [8]. When an ion having this configuration is embedded in a lattice, SOC can give rise to different kind of magnetic interactions which depend on the geometry; indeed, the local angular momentum L is very sensitive to the lattice degree of freedom, then complex magnetic behaviors can arise when the combined effect of strong SOC, electronic correlations and hopping connectivity is considered. A relevant example is definitively given by the hexagonal iridates such as Na_2IrO_3 and Li_2IrO_3, characterized by a layered structure consisting of an honeycomb lattice of Ir^{4+} ions. In the ideal limit, the edge sharing of neighboring IrO_6 octahedra, and also the structure of the entangled $J_{eff} = \frac{1}{2}$ orbitals, lead to a cancellation of the usually dominant antiferromagnetic oxygen-mediated exchange interactions [24]. A sub-dominant term is generated by the Hund's coupling, which takes the form of highly anisotropic exchange and is described by the following Hamiltonian:

$$H = -K \sum_{\alpha=x,y,z} \sum_{<ij>\in\alpha} S_i^\alpha S_j^\alpha \tag{1.1}$$

where S_i are the effective spin-$\frac{1}{2}$ operators and α labels both spin components and the three orientations of links on the honeycomb lattice. Hamiltonian (1.1) is known as Kitaev model. In such model, effective spin-$\frac{1}{2}$ operators are coupled to their three nearest neighbours by ferromagnetic Ising interaction, with bond-dependent easy axes parallel to the x,y and z axes. The orthogonal anisotropy of the three nearest neighbour bonds creates a conflict between

these bonds, giving rise to strong magnetic frustration of competing exchange interactions that cannot be simultaneously satisfied, generating a large degeneracy of the system ground state. The model has raised a considerable interest since it can be exactly solved by mapping the spins into Majorana fermions [25]. The ground state associated to (1.1) is a quantum spin liquid, in which interacting spins remain quantum disordered without spontaneous symmetry breaking. Then, the model describes a state with no magnetic order and elementary excitations which are charge-neutral "spin" carrying Majorana fermions that are their own antiparticles. It is amazing that the Kitaev exchange form of (1.1), which is very unnatural for conventional magnetic systems, arises organically from the geometry and entanglement in the strong SOC limit.

The above considerations tell us that the interplay between large SOC and the lattice geometry is a crucial ingredient in determining the magnetic state of heavy TMOs. Then, we can explore the SOC effects by considering several orbital configurations which support this idea. The most common orbital configuration is depicted in Fig. 1.3 and it is relative to an octahedral structure, where the crystal field separates the d orbitals into two sets of manifolds with an energy difference Δ_O; here, the t_{2g} orbitals are lower in energy and SOC acts on them at the first order,leading to a splitting of these levels. Corresponding effects in an e_g manifold have rarely been considered due to the conventional wisdom that the orbital angular momentum is quenched in these states. This means that, at the first order, SOC does not act on e_g states and that some influence of it may appear only at higher orders. In particular, SOC modifies the ground state only via virtual processes in-

volving the t_{2g} subspace and acting across the crystal field splitting Δ_O, thus determining magnetic anistropy [26]. However, particular cases which lead to conclusions in contrast to this conventional scenario can be treated. In tetrahedral complexes, the d orbitals again split into two orbital subspaces with an energy difference Δ_t, where the hierarchy of e_g and t_{2g} orbitals is reversed with respect to the octahedral case. Considering $5d$ TM encaged in TMO_4 tetrahedra, the crystal field splitting then naturally favors the occupancy of the lower e manifold, with a crystal field energy which is relatively small in size and lower than the octahedral case; this evidence is expected since the ligand ions in tetrahedral symmetry are not oriented directly towards the d orbitals. Under these conditions, SOC corrections can be amplified and can lead to interesting effects. To support this idea, in the first part of the thesis we analyze the effects of a large SOC on the magnetic state of a d^1 TM ion located in a tetrahedral environment. We verify that, while in the ideal tetrahedral geometry SOC acts only as a perturbation on the atomic energy levels set by the crystal field splitting, its effect can be strongly enhanced in the case of a distorted geometry. We consider the specific case where the tetrahedron is compressed along the z direction and the results of our study show that large SOC not only induces a substantial anisotropic unquenched orbital angular momentum, but its interplay with crystal field parameters significantly affects also the hierarchy of the lowest energy levels which are involved in the magnetic superexchange.

In order to analyze the emergence of this unquenched orbital angular momentum component in the e_g subspace and to examine what kind of interactions are generated when particular geometries are considered, our analysis natu-

rally focused on the $KOsO_4$, which represents an ideal candidate in many respects. $KOsO_4$ is a Mott insulator which crystallizes in a tetragonal scheelite-like structure consisting in isolated and quite compressed OsO_4 tetrahedra. The geometric structure of the compound seems to be particularly relevant for our purpose. On one side, the isolated tetrahedra imply a reduction of the connectivity and, as a consequence, the effects of the local energy scales (Coulomb correlations, SOC and crystal field energy) are emphasized. Furthermore, in the scheelite structure the Os ions reside on lattice sites which constitute a substantially elongated diamond sublattice, where each Os atom is covalently bonded to the oxygens in a tetrahedral configuration. The particular 3D arrangement perfectly allows for dominant hopping connectivity between the lowest e and the highest t_2 sector; this provides another important route to magnify the SOC correction that now come into play at leading order in the superexchange processes involving t_2 orbitals. Therefore, the prospect of an anisotropic exchange in the $KOsO_4$ is concrete, due to its peculiar lattice geometry. In our study, we analyze the competition between strong electron correlations, SOC and tetrahedral deformations in the e^1 configuration of the Os^{7+} ions and prove that, due to the peculiar hopping connectivity and the character of the structural deformation, an entangled spin/orbital state emerges, marked by magnetic anisotropy. Moreover, we demonstrate that SOC plays an active role in setting the boundary between nearest neighbour antiferromagnetic and anisotropic ferromagnetic exchange, which have a specific Ising-like character that depends on the orientation of each given bond. This result prefigures a link between the bond direction and the sign (FM-AFM) of the superexchange coupling per spin component, that

reminds a Kitaev-type coupling, where competing components are active at the same time.

Another strategy in order to magnify the effect of SOC is to achieve microscopic conditions which can lower the kinetic energy, thus enhancing the $\frac{\lambda}{t}$ ratio. This can be reached, for example, considering disconnected structures, which can be conveniently realized in systems where the TMO_x units are rather isolated, allowing for extremely low kinetic connection between the heavy TM. The second part of the thesis deals with this idea: we consider a trilayered structure that reminds compounds associated to the Ruddlesden-Popper series $A_{n+1}B_nX_{3n+1}$ (A=rare earth element, B=TM, X=oxygen), where the building block is made of TM ions, which form a three-site chain along the z direction. The term "disconnected" has to be intended in this context to indicate that the in-plane itineracy is supposed to be highly damped, promoting the interplay between the local energy scales, which are dominant. In the considered structure, we neglect the Coulomb interaction at the first order and limit ourselves to explore the competition between SOC, intra-cell delocalization and lattice deformations, in determining the electronic structure. Such study is very timely and relevant in many respects. First of all, it is connected with the concept of topological band theory and the existence of symmetry-protected topological phases. In the past few years, it has been realized that not only internal symmetries such as time reversal, but also crystal symmetries, for example crystal reflection or rotation, can lead to the protection of topological states [27, 28, 29]. Additional symmetries can generate richer topological structures, as it has been

recently shown for semimetals [30]. The trilayer- model Hamiltonian upon examination is indeed a manifestation of combined internal (time-reversal) as well as crystal lattice symmetries. Specifically, the combination of time-reversal and spatial inversion symmetries is known to be the prerequisite ensuring the Kramer's degeneracy for every eigenstate at any wavevector $\mathbf{k}$. In addition, our trilayer problem has an additional characteristic symmetry, namely the "layer-interchange" symmetry, which leaves the Hamiltonian unchanged upon interchanging the outer layer flavours. As we will demonstrate, this allows to label the eigenstates with a layer-parity index $\mathscr{F} = \pm 1$.

In the second instance, the limit of an almost isolated trilayer allows to investigate in a well controlled manner the evolution and eventually the closing of the energy gaps in a weakly dispersing electronic structure, by using the SOC as the driving tuning parameter which is able to lift the degeneracy of the spin/orbital entangled states.This kind of analysis opens the way to the search for novel topological nodal semimetals, which are realized in presence of large SOC and protected by layer interchange symmetry. In our search, we make a systematic analysis in weak and strong SOC regime in order to analyze the evolution of the nodal lines, simulating different local environments spanning from the ideal undistorted octahedra to the compressed/elongated octahedra, by modifying the on-site CF parameters, and we characterize the transitions between different topological electronic configurations.

1.3 Overview of the Thesis

The principal aim of this thesis is to bring out the effect of SOC by facing two specific problems which offer novel and unconventional perspectives towards possible emerging phases driven by large SOC in TMOs. The first part of the thesis is focused upon the influence of SOC on the magnetic states of correlated TMs in tetrahedral compounds, and aims at demonstrating that SOC may play a non trivial role in correlated TMOs with nominal e_g^1 configuration, contrary to the conventional wisdom that the orbital angular momentum is quenched in the e_g subspace. One of the most important findings relates to the possibility to achieve frustrated ferromagnetic nearest neighbor exchange when the interplay between SOC, structural deformations and peculiar lattice geometry occur, as in $KOsO_4$.

In the second part, we explore the possibility to emphasize SOC effects in uncorrelated systems which consists of a trilayer building block, made by three t_{2g} ions oriented along the z direction, which is assumed to be almost disconnected within the xy plane. One of the major result concerns the characterization of the symmetry protected nodal lines which arise from the band crossing between energy states which belongs to different layer interchange symmetry sectors. Those transitions are explored as a function of the driving microscopic parameters represented by SOC and crystal field amplitudes.

In **Chapter 2**, after a brief review of the crystal field theory and the derivation of the SOC relative to d orbitals, we analyze a model Hamiltonian which is suitable to describe $5d$ TMOs containing TMO_4 tetrahedra, where the crystal field splitting leads to partially filled e_g orbitals. The first stage of this

analysis is based on single ion calculations for the ideal tetrahedral symmetry, and subsequently for the distorted tetrahedron, which is a fundamental prerequisite to unveil the effects of SOC and the formation of anisotropic local orbital momentum.

The case of $KOsO_4$ is analyzed in **Chapter 3**, carrying out a study where we use ab-initio calculations derived microscopic parameters as an input for our exact diagonalization study on a two-site cluster of a model Hamiltonian which contains on-site intra-orbital and inter-orbital Coulomb repulsion, the Hund's coupling, the on-site energy, the nearest neighbor intra- and inter-orbital hopping and the SOC.

In **Chapter 4**, we consider a pioneering exploration of a representative material platform allowing for low-connectivity between orbitals of the heavy TM; this purpose is reached by considering a trilayered structure consisting of a building block made by three TM ions connected along the z direction. We present a tight-binding Hamiltonian, which includes the in-plane hopping, the intra-cell hopping,the on-site energy and the SOC, while electronic correlations are neglected at the first order. We evaluate the evolution of the transitions which characterize band crossings between different layer- parity sectors as function of SOC, crystal field and intra-cell hopping parameters.

Chapter 2

Effects of Spin Orbit Coupling in a TM oxides with tetrahedral arrangement

The first part of the chapter provides the theoretical background about SOC and crystal field theory. SOC is introduced as a relativistic effect in a semi-classical framework in order to justify the Z^4 dependence upon the atomic number. Next,we discuss crystal field effects using group theory arguments. Both the derivations privilege qualitative topics, while for a more complete and rigorous discussion we refer to Appendix A and to the references indicated in the text. In the second part of the chapter, general remarks about SOC in TM ions are given. In TMOs, especially those composed by 4d and 5d TM ions, the interplay between these two energy scales may be relevant. In particular, we analyze the effects of a large SOC on the magnetic state of a d^1 TM ion located in a tetrahedral environment and we demonstrate that,

while in the ideal tetrahedral symmetry SOC acts only as a perturbation on the atomic energy levels set by crystal field splitting, its effects are strongly enhanced in the case of distorted geometries. We consider the specific case in which the tetrahedron is compressed along the z direction and show that, increasing the degree of flattening, a large SOC can induce an anisotropic unquenched orbital momentum and can affect the hierarchy of the lowest energy levels involved in the magnetic superexchange.

2.1 Semiclassical derivation of Spin Orbit Coupling

Spin orbit coupling (SOC) is a relativistic interaction of a particle's spin with its orbital angular momentum. It manifests itself in lifting the degeneracy of one-electron energy levels in atoms, molecules, and solids. In addition to the rigorous analytical derivation proposed in Appendix A, we present here a quantitative description of SOC for an electron bound to an hydrogen-like atom, in a framework of classical electrodynamics. The magnetic moment of an electron with spin $\mathbf{s}$ is given by:

$$\boldsymbol{\mu} = -\frac{g}{\hbar}\mu_B \mathbf{s} \tag{2.1}$$

where $g \sim 2$ is the g factor of the electron and $\mu_B = \frac{e\hbar}{2m_0 c}$ (m the mass of the electron and e its charge) is the Bohr magneton. In the electron's rest frame, the nucleus with charge Ze moves around the electron. According to Lorentz transformation of the electric field $\mathbf{E}$, which is due to the nucleus

and through which the electron travels, the latter "sees" a magnetic field $\mathbf{B}$. Indicating with $\mathbf{v}$ the velocity of the electron around the nucleus, one has that:

$$\mathbf{B} = -\frac{1}{c}\mathbf{v} \wedge \mathbf{E} = \frac{1}{m_0 c}(\mathbf{E} \wedge \mathbf{p}) \tag{2.2}$$

Where $\mathbf{p} = m_0\mathbf{v}$ is the electron momentum and the anticommutativity of the cross product is used. The electric field $\mathbf{E}$ can be expressed in terms of the electrostatic potential V:

$$\mathbf{E} = -\frac{\mathbf{r}}{r}\frac{dV}{dr} \tag{2.3}$$

In Eq. (2.3), we have used the central field approximation, assuming that the potential is spherically symmetric. This approximation is exact for hydrogen like systems as the one we are considering. The energy of the electron in the the magnetic field $\mathbf{B}$ due to its magnetic moment then can be written as:

$$h_{SOC} = -\boldsymbol{\mu} \cdot \mathbf{B} = \frac{e}{m_0^2 c^2}\mathbf{s} \cdot (-\frac{\mathbf{r}}{r}\frac{dV}{dr} \wedge \mathbf{p}) \tag{2.4}$$

Considering a Coulomb potential, $V = \frac{Ze}{r}$, and remembering from classical mechanics that $\mathbf{r} \wedge \mathbf{p} = \mathbf{l}$, where $\mathbf{l}$ is the electron angular momentum, spin orbit energy is definitively given by:

$$h_{SOC} = \frac{Ze^2}{m_0^2 c^2}\frac{1}{r^3}\mathbf{l} \cdot \mathbf{s} = \zeta \mathbf{l} \cdot \mathbf{s} \tag{2.5}$$

The result (2.5) is coherent with the one of the analytical derivation proposed in the Appendix A, except for the fact that it is twice larger than (A.47). A factor 2 at the denominator of (2.5) has to be added in order to make consistent the two derivations. This correction,called Thomas factor,

is due to the fact that, two years before the advent of Dirac theory, L.H. Thomas argued that a more careful treatment of SOC in the framework of classical electrodynamics would take into account the energy associated with the precession of the electron spin; this would result in reduction of the energy (2.5) by a factor of two, in agreement with (A.47) [31].

2.1.1 Atomic energy correction of SOC

In order to calculate explicitly the value of the energy associated to the SOC, it is useful to remind that for an electronic state with quantum numbers n and l one has[32]:

$$< \frac{1}{r^3} >= \frac{Z^3}{a_0^3 n^3 l(l+\frac{1}{2})(l+1)} \tag{2.6}$$

Where a_0 is the Bohr radius. In addition, in presence of SOC, it can be shown that $\mathbf{s}$ and $\mathbf{l}$ are no longer separately conserved, but their coupling produces the total angular momentum $\mathbf{j} = \mathbf{l} + \mathbf{s}$. It follows that $\mathbf{l} \cdot \mathbf{s} = \frac{1}{2}(\mathbf{j}^2 - \mathbf{l}^2 - \mathbf{s}^2)$. Hence, the value of $\mathbf{l} \cdot \mathbf{s}$ is given by:

$$< \mathbf{l} \cdot \mathbf{s} >= \frac{1}{2}[j(j+1) - l(l+1) - s(s+1)] \tag{2.7}$$

Using Eq. (2.6) and Eq. (2.7), from Eq. (2.5) we calculate the value of the energy of the SOC, which results:

$$E_{SOC} = \frac{Z^4 e}{4m^2c^2} \frac{j(j+1) - l(l+1) - s(s+1)}{l(l+\frac{1}{2})(l+1)a_0^3 n^3} \tag{2.8}$$

Eq. (2.8) show that spin orbit correction scales as Z^4, where Z is the atomic number of the involved nucleus.

For a many-electron atom, the contribution to the Hamiltonian of the SOC can be obtained by summing (2.5) over all electrons in this way:

$$H_{SOC} = \sum_i \zeta_i \mathbf{l}_i \cdot \mathbf{s}_i \tag{2.9}$$

There are two schemes which can be taken in consideration to describe many-electron states. The first of them is called jj coupling scheme and it is used especially for $4f$ and $5f$ elements; in this scheme, the total angular momentum $\mathbf{j}_i = \mathbf{l}_i + \mathbf{s}_i$ associated to a single electron is calculated, then the total angular momentum $\mathbf{J} = \sum_i \mathbf{j}_i$ is given by the sum over all the total angular momentum of any single electron. The other scheme, called LS or Russel Saunders scheme and used for TM ions, is based firstly on the individuation of $\mathbf{S} = \sum_i \mathbf{s}_i$ and $\mathbf{L} = \sum_i \mathbf{l}_i$, which are respectively the spin and orbital angular momentum of the system. After determining $\mathbf{S}$ and $\mathbf{L}$, SOC is included. According to LS scheme, the full SOC is written as:

$$H_{SOC} = \lambda \mathbf{L} \cdot \mathbf{S} \tag{2.10}$$

The constant λ is composed by all the partial SOC constant ζ_i; for one shell, all the ζ_i are equal each other, then the coupling constant can be written as [33]:

$$\lambda = \pm \frac{\zeta}{2S} \tag{2.11}$$

the sign + is used for less than half filled shells, the sign - for more than half filled shells. Since from the relativistic derivation we know that ζ is a

positive quantity, we have that $\lambda > 0$ for less than half filled shells, $\lambda < 0$ for more than half filled shells.

The interaction (2.10) gives us different energies for terms with different $\mathbf{J} = \mathbf{L} + \mathbf{S}$, which is the total angular momentum obtained by the sum of the spin and orbital angular momentum of the system. According to (2.10) and to the rules of quantum mechanics, in a state with given $\mathbf{J}$ the contribution to the energy due to SOC is:

$$\langle \mathbf{L} \cdot \mathbf{S} \rangle = \frac{J(J+1) - L(L+1) - S(S+1)}{2} \tag{2.12}$$

The SOC has hence the effect to split the atomic energy levels into multiplets, each of which is associated to a well-defined value of the total angular momentum $\mathbf{J}$. As a result, a level with given values of $\mathbf{L}$ and $\mathbf{S}$ is split into a number of levels with different values of $\mathbf{J}$. This splitting is called fine structure of the level.

The ground state of this structure can be determined according to the Hund's rules, whose statements are the following:

- electrons fill levels so as to make the largest possible total spin $\mathbf{S}$, according to the Pauli principle;
- among all the possible configuration in which the spin is maximized, the ground state is the state which has the maximum possible value of the orbital angular momentum $\mathbf{L}$;
- in light of the previous results, for less than half filled shells $\lambda > 0$ and the ground state is the one with the smallest possible value of $\mathbf{J}$, while

for more than half filled shells $\lambda < 0$ and the lowest level is the one with the maximum value of $\mathbf{J}$.

2.2 Crystal field theory

In this section, a brief description of the crystal field theory is given, without the claim to be rigorous. For a more detailed description of the representation theory of point groups, refer to [34, 35].

Transition Metals (TMs) are defined as elements whose atoms have partially filled d shells. When a TM is isolated, the corresponding d orbitals are five-fold degenerate. Conversely, when a TM is placed in a solid, its spherical symmetry O_3 is replaced by the symmetry defined by the crystal structure. A typical structure found in many compounds with TMs is the perovskite ABO_3 reported in Fig. 2.1, where a transition metal ion B is centered inside a regular oxygen O octahedron hosted by a cubic lattice of A which are constituted, for example, by rare-earth ions. The symmetries associated to this kind of structure can be described by the O_h point group [34, 35]. Symmetry operators are reduced to a finite number h = 48, including the identity $\hat{E}$ and the following rotation operators, whose relative rotation axes are indicated in Fig. 2.1: $8\times\hat{C}_3$, which represent the rotation by 120° about a 3-fold axis,$3\times\hat{C}_2$, which are rotation by 180° about a 4-fold axis,$6\times\hat{C}_4$, which are rotation by 180° about a 2-fold axis and $6\times\hat{C}_2'$, which represent a rotation by 90° about a 4-fold axis. Each of them can be further coupled to an inversion operator $\hat{i}$. These symmetry operators can be represented by matrices of different dimensions. A matrix representation is called reducible if every matrix

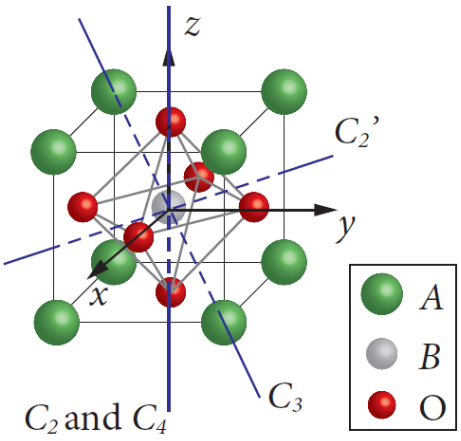

Figure 2.1: A cubic perovskite cell ABO_3 and its rotational symmetry axes

in the representation can be written in the same block form through the same similarity transformation; if this cannot be done, the representation is said to be irreducible. There is an infinite number of equivalent representations of a group, and thus a large arbitrariness in the form of the representation. However, the trace of a matrix, called character, is invariant under a similarity transformation; it is therefore useful to classify matrix representations through their characters. Furthermore, a reducible representation can be decomposed in irreducible ones using the orthogonality relations of characters. One can show that, if $\chi(g_i)$ are the characters of the reducible representation, they must be given by a linear combination of the characters of irreducible representation:

$$\chi(g_i) = \sum_j a_j \chi_j(g_i) \tag{2.13}$$

where the a_j coefficients are determined from orthogonality relations [36]. Hence, the reducible representation Γ can be written as:

$$\Gamma = a_1\Gamma_1 \oplus a_2\Gamma_2 \oplus ... = \bigoplus_j a_j\Gamma_j \tag{2.14}$$

The characters of all possible irreducible representations for the O_h point group are tabulated in Table 2.1 [34], where A, E, and T denote one-, two-, and three-dimensional representations. For operators coupled with inversion $\hat{i}$, the values can remain unaltered or change sign for even (denoted by subscript g, which stands for the German word gerade) or odd (u, ungerade) representations, respectively. Regarding the perovskite structure of Fig. 2.1,

Table 2.1: Characters for the O_h point group

O_h	E	$8C_3$	$3C_2$	$6C_4$	$6C_2^{'}$
A_1	1	1	1	1	1
A_2	1	1	1	-1	-1
E	2	-1	2	0	0
T_1	3	0	-1	1	-1
T_2	3	0	-1	-1	1

for an electron of the TM ion B, the symmetry of the Hamiltonian are determined by the potential relative to the site B and the neighboring ligands O, which can be assumed to be point charges. Considering a d electron, its wave function is $\Psi \propto e^{im\varphi}$, where m is the magnetic quantum number $|m| \leq l$ and l=2 is the angular momentum. A rotation of an angle Φ of this wave function around an arbitrary axis can be represented by a diagonal matrix

$\Gamma_l(\Phi)$= diag($e^{il\Phi}$,$e^{i(l-1)\Phi}$,...,$e^{-il\Phi}$), whose character can be easily calculated:

$$\chi(\Phi) = Tr\Gamma_l(\Phi) = \sum_{m=-l}^{l} e^{-im\phi} = \frac{\sin[(l+\frac{1}{2})\Phi]}{\sin(\frac{\Phi}{2})} \tag{2.15}$$

This result is valid for any direction of the rotation axis and for any d-dimensional basis set obtained by making linear combination of the spherical harmonics $Y^l_m(\theta,\phi)$ functions, because the trace of a matrix is invariant under basis transformation. The character for each symmetry operation in O_h is then given by:

		E	$8C_3$	$3C_2$	$6C_4$	$6C_2'$
χ_{Γ_2}	=	5	-1	1	-1	1

The number n of its irreducible components can be calculated by $n_i=\sum_R \chi_i \cdot \chi_{\Gamma_2}$, where χ_i is the character of the irreducible representations given in Table 2.1.

Recalling Eq. (2.14), the symmetry representation for a d electron with octahedral coordination (O_h symmetry) is then :

$$\Gamma_2 = E \oplus T_2 \tag{2.16}$$

Eq. (2.16) implies that the original five-fold degeneracy is removed in the O_h point group and the d orbitals are split into two levels e_g and t_{2g}, with two- and three-fold degeneracy respectively. The subscript g is added because d orbital are even under inversion.

A conventionally used set of real basis functions for d electrons is shown in Fig. 2.2. Their expressions in terms of spherical harmonics are given in Eq.

(2.17), using the notation $|l, m\rangle$, with $l = 2$ is the angular momentum and m, which is the projection of l along the z axis, assumes values from -l to l:

$$
\begin{aligned}
d_{xy} &= \frac{1}{i\sqrt{2}}(|2,2\rangle - |2,-2\rangle) \\
d_{xz} &= -\frac{1}{\sqrt{2}}(|2,1\rangle - |2,-1\rangle) \\
d_{yz} &= -\frac{1}{i\sqrt{2}}(|2,1\rangle + |2,-1\rangle) \\
d_{z^2} &= |2,0\rangle \\
d_{x^2-y^2} &= \frac{1}{\sqrt{2}}(|2,2\rangle + |2,-2\rangle)
\end{aligned}
\tag{2.17}
$$

The first three wavefunctions belong to the t_{2g} subspace, while the last two are part of the e_g subspace.

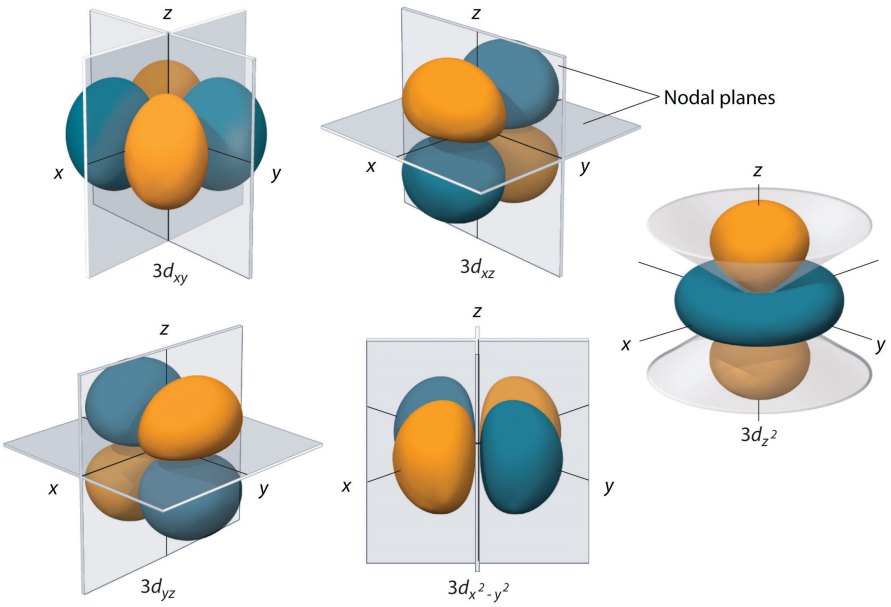

Figure 2.2: Angular distribution of the d orbitals

The lifting of degeneracy is evident looking at the shape of the orbitals: the e_g orbitals point directly to the neighboring negatively-charged ligand oxygens, therefore experience stronger Coulomb repulsion compared to the t_{2g} ones and are thus energetically less stable. The resulting energy difference is called Crystal Field (CF) splitting Δ_{CF}. The hierarchy of the two orbital subspaces is inverted when TM ion is placed, for example, in a tetrahedral arrangement. An octahedron and a tetrahedron are related geometrically: octahedral coordination results when ligands are placed in the centers of cube faces, while tetrahedral coordination results when ligands are placed on alternate corners of a cube. The regular tetrahedron belongs to the point group T_d and symmetry operations are reduced to a finite number h=24; these include the identity $\hat{E}$, $8\times\hat{C}_3$,$3\times\hat{C}_2$ as in the case of the octahedron, $6\times\hat{S}_4$=$6\times\hat{C}_4\hat{\sigma}_h$, where σ_h is a symmetry operator that indicates a reflection in a plane of symmetry perpendicular to the main symmetry axis, and finally $6\times\hat{\sigma}_d$, where σ_d is a reflection in a plane which contains the symmetry axis. The symmetry operations for a T_d point group are thus very closely related to those of the O_h one, the most important difference is that the T_d point group does not possess a symmetry center and thus has no inversion operation [34]. In the case of a tetrahedral coordination then, the *d* orbitals are split into two levels as in an octahedral configuration, but the e doublet lies lower than the t_2 triplet, which can qualitatively be understood by observing that now the t_2 electrons experience a stronger Coulomb repulsion than e electrons and are higher in energy. Note that the subscript g is removed since there is not inversion in T_d. Concerning these two particular configurations, the splitting which separates the two orbital subspaces in a tetrahedral arrangement Δ_t is

smaller than the splitting Δ_o which characterizes an octahedral coordination with the same ligands. In the simplest cases, the relation between the two CF splittings is given by [33] :

$$\Delta_t = \frac{4}{9}\Delta_o \tag{2.18}$$

The two arrangements are schematically shown in Fig.2.3:

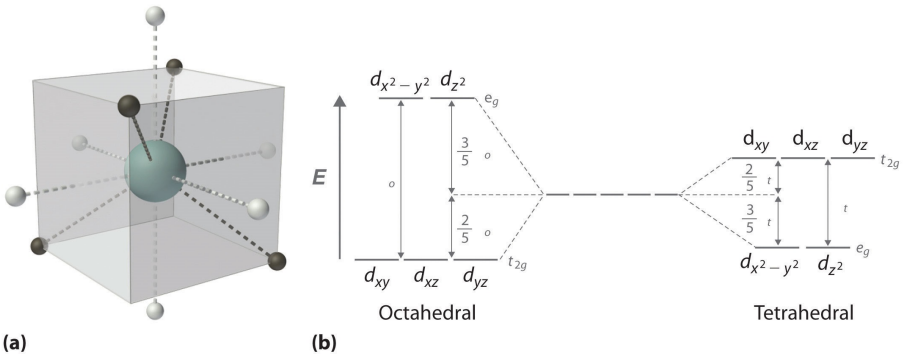

Figure 2.3: (a) Schematical representation of a TM ion in an octahedral (white) and tetrahedral (grey) environment and (b) the relative crystal field splittings

Distortions of the structure can further reduce the symmetry and this can lead to additional CF splitting. The most common distortion of the octahedral cristalline field is the tetragonal distortion, which causes further splitting in the orbital subspaces schematically shown in Fig. 2.4.

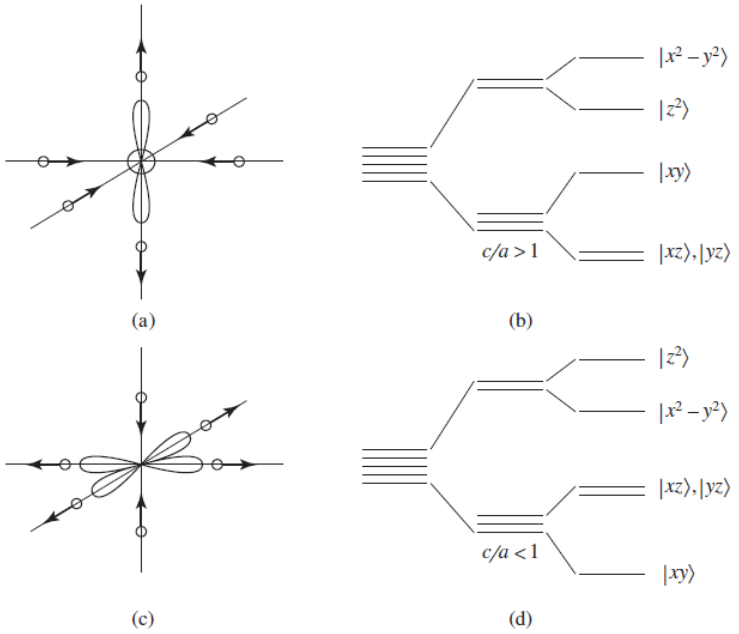

Figure 2.4: Tetragonal (a) elongation and (c) compression of a TMO_6 octahedral structure and corresponding (b) (d) splitting of d levels

2.3 Spin orbit coupling in TM oxides

2.3.1 T-P equivalence

The matrix elements of orbital angular momentum $l = 2$ for a single electron in the five fold degenerate d-orbitals respect to the basis $\{ d_{yz}, d_{xz}, d_{xy}, d_{z^2}, d_{x^2-y^2} \}$ are [37]:

$$l_x^d = \begin{pmatrix} 0 & 0 & 0 & -\sqrt{3}i & -i \\ 0 & 0 & i & 0 & 0 \\ 0 & -i & 0 & 0 & 0 \\ \sqrt{3}i & 0 & 0 & 0 & 0 \\ i & 0 & 0 & 0 & 0 \end{pmatrix} \tag{2.19}$$

$$l_y^d = \begin{pmatrix} 0 & 0 & -i & 0 & 0 \\ 0 & 0 & 0 & \sqrt{3}i & -i \\ i & 0 & 0 & 0 & 0 \\ 0 & -\sqrt{3}i & 0 & 0 & 0 \\ 0 & i & 0 & 0 & 0 \end{pmatrix} \tag{2.20}$$

$$l_z^d = \begin{pmatrix} 0 & i & 0 & 0 & 0 \\ -i & 0 & 0 & 0 & 0 \\ 0 & 0 & 0 & 0 & 2i \\ 0 & 0 & 0 & 0 & 0 \\ 0 & 0 & -2i & 0 & 0 \end{pmatrix} \tag{2.21}$$

As we can see in the (2.19),(2.20) and (2.21), the orbital momentum is quenched in the e_g subspace

$$\langle e_g | \mathbf{l} | e_g \rangle = 0 \tag{2.22}$$

This implies that SOC has no effect at first order on e_g orbitals. Looking at the analogous matrices in the basis of the p orbitals:

$$l_x^p = \begin{pmatrix} 0 & 0 & 0 \\ 0 & 0 & -i \\ 0 & i & 0 \end{pmatrix} \tag{2.23}$$

$$l_y^p = \begin{pmatrix} 0 & 0 & i \\ 0 & 0 & 0 \\ -i & 0 & 0 \end{pmatrix} \tag{2.24}$$

$$l_z^p = \begin{pmatrix} 0 & -i & 0 \\ i & 0 & 0 \\ 0 & 0 & 0 \end{pmatrix} \tag{2.25}$$

and comparing them with the matrix elements of l in the t_{2g} subspace (2.19),(2.20) and (2.21), it is evident that we can map these states with $l = 2$ onto the p-states with $l = 1$ in this way:

$$\mathbf{l}(t_{2g}) = -\mathbf{l}(p) \tag{2.26}$$

This relation is called $T-P$ equivalence. According to it, the orbital angular momentum in t_{2g} states is partially quenched from $l = 2$ to $l = 1$. This equivalence can be conveniently used when there is a large splitting within the d orbitals due to the crystal field, neglecting the off-diagonal terms of (2.19),(2.20) and (2.21) [38]. Using (2.26), we can express the spin orbit interaction on t_{2g} levels mapping the t_{2g} orbital states through an effective orbital angular momentum $\widetilde{l} = 1$:

$$H_{SOC} = \widetilde{\lambda}\widetilde{\mathbf{l}} \cdot \mathbf{S} \tag{2.27}$$

where $\widetilde{\lambda} = -\lambda$ [39]. According to this equality, the second Hund's rule for the t_{2g} subshell in this mapping is reversed: the ground state for less-than-half filled shells is the state with maximum total angular momentum $\widetilde{J}$, while for more-than-half filled shells the ground state is the state with smaller $\widetilde{J}$. The effect of the spin orbit coupling on these levels at the first order is to produce a splitting of them.For example, considering the configuration t_{2g}^1,

where $\widetilde{l} = 1$ and $S = \frac{1}{2}$, the total degeneracy is $(2\widetilde{l}+1)(2S+1) = 6$. This six levels are split by spin orbit coupling in a quartet with $\widetilde{J} = \widetilde{l} + S = \frac{3}{2}$, which is the ground state according to Hund's rule, and a doublet $\widetilde{J} = \widetilde{l} - S = \frac{1}{2}$. If we considered the "complementary" configuration t_{2g}^5, with one hole in the subspace, the situation would not change but the doublet would be the ground state. This is what seems to occur in $5d^5$ iridates, that are the most dramatic example in which a quite strong SOC changes the character of the multiplet state, thus reducing the magnetic state of Ir^{4+} to an effective Kramers doublet with effective total angular momentum $j = 1/2$, as we have mentioned in the Introduction.

2.4 SOC matrix in d orbitals

In order to calculate SOC matrix elements for a S=$\frac{1}{2}$ electron in the t_{2g} subspace,we rewrite H_{SOC} in terms of x, y and z components of the spin and the angular momentum:

$$H_{SOC} = \lambda \mathbf{L} \cdot \mathbf{S} = \lambda(L_x S_x + L_y S_y + L_z S_z) \tag{2.28}$$

Indeed, we can construct the matrix element using the following relations for spin and angular momentum operators:

$$L_x = \frac{1}{2}(L_+ + L_-) \qquad L_y = \frac{1}{2i}(L_+ - L_-) \tag{2.29}$$

$$S_x = \frac{1}{2}(S_+ + S_-) \qquad S_y = \frac{1}{2i}(S_+ - S_-) \tag{2.30}$$

L_+ and L_- are raising and lowering operators for the angular momentum respectively and their action on a generic state with quantum numbers k, l, m is:

$$L_\pm \psi_{k,l,m}(\mathbf{r}) = \sqrt{l(l+1) - m(m \pm 1)}\psi_{k,l,m\pm1}(\mathbf{r}) \tag{2.31}$$

The S_+ and S_- operators act on the spin in the following way:

$$S_+ |\uparrow\rangle = 0 \tag{2.32}$$

$$S_+ |\downarrow\rangle = |\uparrow\rangle \tag{2.33}$$

$$S_- |\uparrow\rangle = |\downarrow\rangle \tag{2.34}$$

$$S_- |\downarrow\rangle = 0 \tag{2.35}$$

Adding to these relations the others that are related to the z component of angular momentum and spin:

$$L_z \psi_{k,l,m}(\mathbf{r}) = m\psi_{k,l,m}(\mathbf{r}) \tag{2.36}$$

$$S_z |\uparrow\rangle = \frac{1}{2} |\uparrow\rangle \qquad S_z |\downarrow\rangle = -\frac{1}{2} |\downarrow\rangle \tag{2.37}$$

we can calculate element by element the SOC matrix.We assume $\hbar = 1$ for all the dissertation. Taking in consideration Eq. (2.29), we can rewrite the Hamiltonian in this way:

$$H_{SOC} = \lambda[\frac{1}{2}(L_+S_- + L_-S_+) + L_zS_z] \tag{2.38}$$

If we apply this operator to the representation of the d orbitals (2.17), the H_{SOC} matrix which we obtain in the t_{2g} subspace and in the

$\{ d_{yz} \uparrow, d_{yz} \downarrow, d_{xz} \uparrow, d_{xz} \downarrow, d_{xy} \uparrow, d_{xy} \downarrow \}$ basis is:

$$H_{SOC}^{t_{2g}} = \frac{\lambda}{2} \begin{pmatrix} 0 & 0 & i & 0 & 0 & -1 \\ 0 & 0 & 0 & -i & 1 & 0 \\ -i & 0 & 0 & 0 & 0 & i \\ 0 & i & 0 & 0 & i & 0 \\ 0 & 1 & 0 & -i & 0 & 0 \\ -1 & 0 & -i & 0 & 0 & 0 \end{pmatrix} \tag{2.39}$$

We can construct with the same procedure also the matrix which couples the t_{2g} and the e_g states:

$$H_{SOC}^{e_g - t_{2g}} = \frac{\lambda}{2} \begin{pmatrix} 0 & -\sqrt{3}i & 0 & -i \\ -\sqrt{3}i & 0 & -i & 0 \\ 0 & \sqrt{3} & 0 & -1 \\ -\sqrt{3} & 0 & 1 & 0 \\ 0 & 0 & 2i & 0 \\ 0 & 0 & 0 & -2i \end{pmatrix} \tag{2.40}$$

Here , columns of the matrix are written in the order $\{ d_{z^2} \uparrow, d_{z^2} \downarrow, d_{x^2-y^2} \uparrow, d_{x^2-y^2} \downarrow \}$ basis, while the order of the basis of the t_{2g} orbitals remains unchanged.

2.4.1 General remarks about the effect of spin orbit coupling on d orbitals

SOC turns out to be a fundamental ingredient in determining the multiplet structure of t_{2g} TM compounds. The study of the effects of SOC on these

kind of compound has been carried on for a long time, as we have mentioned in the Introduction, and currently we know that it is very different, depending on the class of TM that we consider.

In $3d$ TMOs, the Coulomb interaction is about U $\sim$ 5 eV, the SOC energy $\lambda \sim$ 20 meV [40]. The $3d$ states are not five-fold degenerate in a crystal and, very often, TM ions are surrounded by six oxygen ions, making an octahedral structure; here, the energy splitting within the t_{2g} and e_g subspaces assumes typically an intermediate value of the previous energetic scales. Since SOC is smaller that the other energy scales, the electronic state is fully described by a spin-only Hamiltonian and the Hund's rule determines the ground state value of $\mathbf{L}$ and $\mathbf{S}$. In this picture, SOC is treated as a small perturbation, which primarily can give rise to magnetic anisotropy [41]. Since the SOC magnitude grows as Z^4 (see Eq. (2.8)), for $4d$ and $5d$ TM oxides it can play a major role. $4d$ TMs are systems with less correlated wide bands, because of the weaker electronic correlations compared to the $3d$ case. For the $4d$ TMOs like ruthenates, where $\lambda \sim$ 0.1-0.2 eV, the situation is controversial:on one hand, in band-structure calculations [42, 43] and in spin-sensitive photoemission [44] the effect of SOC is clearly observed; on the other hand, Dynamical Mean Field Theory approach [45, 46] reveal that ruthenates are Hund's metals and their magnetic behavior can be successfully described without taking in consideration SOC. $4d$ TM ions naturally bridge two different regimes of the strongly correlated $3d$ compounds and $5d$ compounds.

In $5d$ TM compounds, the situation is well-defined:$5d$ orbitals are expected to be more extended and the Coulomb interaction value is further reduced compared to the $3d$ and $4d$ cases.Moreover, the typical value of SOC is $\lambda \sim$

0.5 eV [47], so its effect cannot be neglected at all. $5d$ TMOs may possess an unquenched orbital momentum which is rigidly tied to the spin direction by the large intra-atomic SOC. In particular, in the case of a metal ion in an octahedral environment (TMO_6), an increasing experimental evidence indicates that it is necessary to take into account a quite large SOC to achieve the correct magnetic state within the t_{2g} manifold. As we have already discussed previously, the most dramatic example occurs in $5d$ iridates, where a quite strong SOC changes the character of the multiplet:after splitting of the energy levels due to CF, SOC further splits the t_{2g} orbitals with spin degeneracy, thus reducing the magnetic state of Ir^{4+} to an effective Kramers doublet with effective total angular momentum $J_{eff} = \frac{1}{2}$. Conversely, the SOC in $5d^3$ osmium-based compounds can be treated perturbatively, although it is anyhow necessary to account for the SOC-induced anisotropy, which is essential in the selection of the the magnetic ground state [48, 49, 50, 51].

Systems with active e_g degrees of freedom offer a completely different playground. As we have seen in the previous section,the orbital momentum is fully quenched within these orbitals , hence SOC modifies the ground state only via virtual processes involving the t_{2g} orbitals and, therefore, acting across the CF splitting. However, this effect may be considerably enhanced in $5d$ metal oxides containing TMO_4 tetrahedra, since the CF splitting naturally favors the occupancy of the lower e_g manifold. In addition, the CF energy, although being the largest energy scale, is relatively small in size, as stated by (2.18).

2.5 Interplay between SOC and distortions in a tetrahedral environment

2.5.1 Ideal tetrahedral symmetry

In order to understand the role that SOC plays on magnetism in TMO_4 tetrahedra, it is a good starting point to consider an ionic d^1 configuration having spin $S = \frac{1}{2}$, where both the Coulomb interaction and the Hund's coupling within the d subspace are neglected. A schematic representation of the ideal

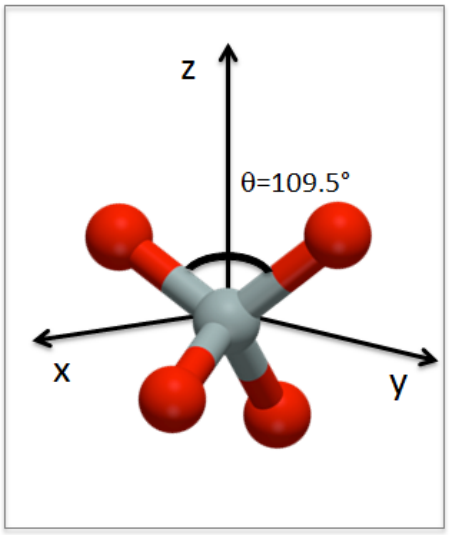

Figure 2.5: Tetrahedral arrangement, where the TM ion is located at the origin of the coordinate system and the angle formed by the edges of the ideal tetrahedron is 109.5°

tetrahedral geometry is reported in Fig. 2.5, with a TM ion surrounded by a cage of four O ligands. We firstly consider the equilibrium position of the tetrahedron, which means that the angle between the edges of it is equal to 109.5°. The energies of the d orbitals are affected by the arrangement of the four negative charges leading to the CF splitting of the d levels into two

different subspaces. The top three are the d_{xy},d_{xz} and d_{yz} orbitals, which constitute the t_2 sector, while the bottom two are the $d_{x^2-y^2}$ and d_{z^2} which span the e manifold (Fig. 2.6(a)).

The Hamiltonian is composed only by the two interaction terms which characterizes our simplified scheme, which are the CF and SOC:

$$H = H_{CF} + H_{SOC} = \sum_{\alpha} \epsilon_{\alpha} n_{\alpha} + \lambda \mathbf{L} \cdot \mathbf{S} \tag{2.41}$$

where α labels the d orbitals, $\epsilon_{yz} = \epsilon_{xz} = \epsilon_{xy} \equiv \epsilon_{t_2}$ and $\epsilon_{x^2-y^2} = \epsilon_{z^2} \equiv \epsilon_e$ stand for the on-site energies of the t_2 and the e in the ideal tetrahedron, respectively, and λ is the positive SOC parameter. Furthermore, $\mathbf{S}$ is the spin one-half operator while $\mathbf{L}$ is the angular momentum operator for a single electron in one of the five-fold degenerate d-orbitals, whose component are given in (2.19),(2.20) and (2.21) in matrix representation. We have calculated in (2.39) and (2.40) the contribution of SOC to the Hamiltonian, then we have all the ingredients to construct the matrix representation of the Hamiltonian (2.41) in the basis $(d_{yz,\uparrow}, d_{yz,\downarrow}, d_{xz,\uparrow}, d_{xz,\downarrow}, d_{xy,\uparrow}, d_{xy,\downarrow}, d_{z^2,\uparrow}, d_{z^2,\downarrow}, d_{x^2-y^2,\uparrow}, d_{x^2-y^2,\downarrow})$:

$$\begin{pmatrix}
\Delta_t & 0 & \frac{i\lambda}{2} & 0 & 0 & -\frac{\lambda}{2} & 0 & -\frac{\sqrt{3}i\lambda}{2} & 0 & -\frac{i\lambda}{2} \\
0 & \Delta_t & 0 & -\frac{i\lambda}{2} & \frac{\lambda}{2} & 0 & -\frac{\sqrt{3}i\lambda}{2} & 0 & -\frac{i\lambda}{2} & 0 \\
-\frac{i\lambda}{2} & 0 & \Delta_t & 0 & 0 & \frac{i\lambda}{2} & 0 & \frac{\sqrt{3}\lambda}{2} & 0 & -\frac{\lambda}{2} \\
0 & \frac{i\lambda}{2} & 0 & \Delta_t & \frac{i\lambda}{2} & 0 & -\frac{\sqrt{3}\lambda}{2} & 0 & \frac{\lambda}{2} & 0 \\
0 & \frac{\lambda}{2} & 0 & -\frac{i\lambda}{2} & \Delta_t & 0 & 0 & 0 & i\lambda & 0 \\
-\frac{\lambda}{2} & 0 & -\frac{i\lambda}{2} & 0 & 0 & \Delta_t & 0 & 0 & 0 & -i\lambda \\
0 & \frac{\sqrt{3}i\lambda}{2} & 0 & -\frac{\sqrt{3}\lambda}{2} & 0 & 0 & 0 & 0 & 0 & 0 \\
\frac{\sqrt{3}i\lambda}{2} & 0 & \frac{\sqrt{3}\lambda}{2} & 0 & 0 & 0 & 0 & 0 & 0 & 0 \\
0 & \frac{i\lambda}{2} & 0 & \frac{\lambda}{2} & -i\lambda & 0 & 0 & 0 & 0 & 0 \\
\frac{i\lambda}{2} & 0 & -\frac{\lambda}{2} & 0 & 0 & i\lambda & 0 & 0 & 0 & 0
\end{pmatrix} \tag{2.42}$$

where $\Delta_t = \epsilon_{t_2} - \epsilon_e$ is a positive constant measuring the energy gap between the e and the t_2 orbitals. As it is evident from (2.42), the effect of SOC is to produce an entanglement between spin and orbital degrees of freedom in the electronic wavefunction;however, in the case of a tetrahedral d^1 configuration, the e manifold is constituted only by vanishing matrix elements. This implies that SOC can have an effect on the e orbitals only at second order in a perturbative expansion in $\frac{\lambda}{\Delta_t}$. The conditions of the specific case which we are considering (strong SOC and modest CF) allow us to imagine that these second order corrections may be relevant.

In order to bring out an effect of SOC on e orbitals, one can treat the SOC term perturbatively, adding it as a perturbation to the Hamiltonian composed by the CF energy terms. Considering the e subspace as the ground state of the system, then ϵ_e=0 and $\epsilon_{t_2} = \Delta_t$, we divide each terms of Eq.

(2.41) by Δ_t :

$$\frac{1}{\Delta_t}H = \tilde{H} = \sum_{\alpha} n_\alpha + \frac{\lambda}{\Delta_t}\mathbf{L}\cdot\mathbf{S} \tag{2.43}$$

note that here $\alpha = xy, xz$ and yz in light of the previous assumption. Now, defining:

$$\delta = \frac{\lambda}{\Delta_t} < 1 \tag{2.44}$$

we perform a perturbative calculation on $\tilde{H}$ in the parameter δ, projecting $\tilde{H}$ in the e subspace through the Lowdin procedure (see Appendix B). The result of the projection is that SOC produces an energy gain that grows increasing δ:

$$\Delta E_{SOC} = \frac{3}{2}\Delta_t\delta^2 + [\delta^3] \tag{2.45}$$

This means that the e-t_2 SOC matrix elements in (2.42) contribute with an energy correction to the dominant energy scale that is proportional to the ratio $\frac{\lambda^2}{\Delta_t}$ and that is the same for each of the e orbitals. As a result, the energies of the e levels have been modified by SOC correction, but they are still degenerate. It is evident that there is an internal symmetry that SOC is not able to remove. Conversely, the same procedure carried out in the t_2 subspace confirms that SOC splits the t_2 orbitals,which are characterized by an unquenched projection of L. The evolution of the energy levels obtained by diagonalizing the matrix of Eq.(2.42) is schematically shown in Fig. 2.6(b): as one can see, the SOC affects neither the degree of degeneracy nor the hierarchy of the lower four-fold degenerate levels. We point out that, as a consequence of the spin-orbital mixing provided by the SOC, a non-vanishing

orbital angular momentum arises, which is fully isotropic. Therefore, the

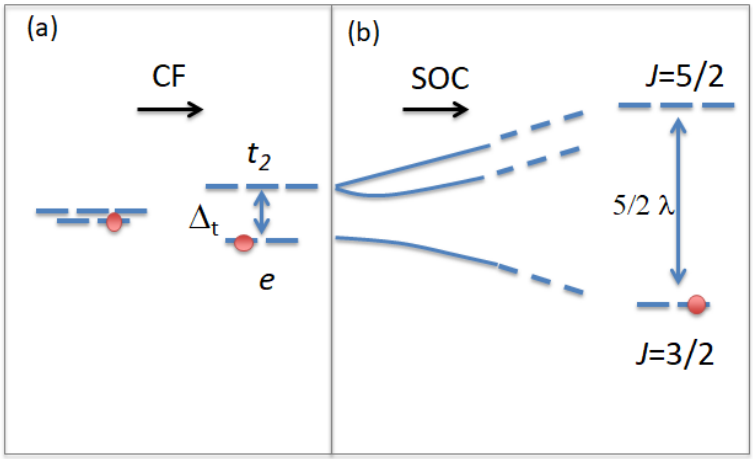

Figure 2.6: (a) Shift of the e_g orbitals with respect to the t_2 ones by Δ_t. (b) Evolution of the energy levels in presence of SOC

effect of SOC on e orbital in the ideal tetrahedron symmetry is simply an alteration of their energy, because they remain fully degenerate.

2.5.2 Tetrahedral distortions

Distortions of the tetrahedral structure may have a role, because they can lead to a symmetry lowering and also magnetocristalline anisotropy. Although these are second-order effect, they are not completely negligible. It is a good starting point to consider the interplay between SOC and the tetrahedral distortions and how they affect the spin-entangled ground state. In doing that, we will assume that the tetrahedron is firstly deformed as to remove the orbital degeneracy and then achieves a new lower energy ground state. Then, we proceed starting from the limit of zero spin orbit coupling to investigate how the energy levels are affected when we turn on the spin orbit interaction.

As reported in detail in Appendix C, a generic tetrahedron has nine normal modes, classified according to the symmetry of the tetrahedron.We consider a local deformation related to a specific static normal mode, that can be obtained by varying the O-TM-O angle without affecting the TM-O length, which is left as a free parameter. It is possible to visualize these deformations as a squashed or a squeezed tetrahedron along the z direction, depending on the variation of the angle θ between the edges of the tetrahedron respect to the ideal angle (see Fig. 2.7). These distortions, which are attributable to the static Jahn Teller effect, induce a partial lifting of the orbital degeneracy even in the absence of SOC. In particular, we expect that the configuration in which the tetrahedron is squashed, which means that the variation of the angle is $\delta\theta > 0$, supports energetically the orbitals which have an apical component instead of planar one, while for a squeezed tetrahedron, in which $\delta\theta < 0$, it is the contrary. To get an estimate of the modified on-site energies E_α, we calculate the potential energy that the d^1 electron, treated as a point charge located at the origin, experiences because of four negative point charges located at the O sites. It is well-know that the potential acting on a TM ion from the surrounding ligand ions is given by:

$$V(\mathbf{r}) = \sum_i \frac{Z_i e^2}{|\mathbf{r} - \mathbf{R_i}|} \tag{2.46}$$

where $\mathbf{r}$ is the position vector of the TM ion, $\mathbf{R_i}$ and $Z_i e$ are respectively the position vector of the i-th ligand ion and its charge. This potential is called CF potential. We calculate its value for a distorted tetrahedral structure, using then the position vectors assumed by ligands after the distortion. For

this reason, we have written the potential and the position vectors in spherical coordinates and we have used the expression of the Laplace expansion for the inverse distance between vectors $\mathbf{r}$ and $\mathbf{R_i}$ [36]:

$$\frac{1}{|\mathbf{r}-\mathbf{R_i}|} = \sum_{l=0}^{\infty} \frac{4\pi}{2l+1} \sum_{m=-l}^{l} (-1)^m \frac{r_<^l}{r_>^{l+1}} Y_l^{-m}(\theta,\varphi) Y_l^m(\theta',\varphi') \tag{2.47}$$

where $\mathbf{r}$ has coordinates (r,θ,φ) and $\mathbf{R_i}$ has (r',θ',φ'), with homogeneous polynomials of degree l in (x,y,z); $\mathrm{r}_<$ and $\mathrm{r}_>$ are respectively the smaller and larger of $\mathbf{r}$ and $\mathbf{R_i}$ and the function Y_l^m represents a normalized spherical harmonic function. In this way, we obtain an expression for the potential in the distorted structure we are dealing with. In order to calculate the CF energy levels arising from our distorted tetrahedral structure, we have to evaluate the following integral for each orbitals:

$$E_\alpha = \int \Psi^*(\mathbf{r},\theta,\varphi) V \Psi(\mathbf{r},\theta,\varphi) r^2 \sin\theta dr d\theta d\varphi \tag{2.48}$$

where $\Psi(\mathbf{r},\theta,\varphi)$ are the wavefunctions of the d orbitals (2.17) written here in spherical coordinates. By evaluating the averages of the potential over the d orbitals, we obtain the dependence on the deviation angle of the on-site energies, which are reported in Fig.2.7; note that the energies of the levels are rescaled at the ground state energy and renormalized to the value of Δ_t.

From Fig. 2.7, it is evident that tetrahedral distortions have opened a gap in the e and t_2 subspace. For positive deformations, reported on the right

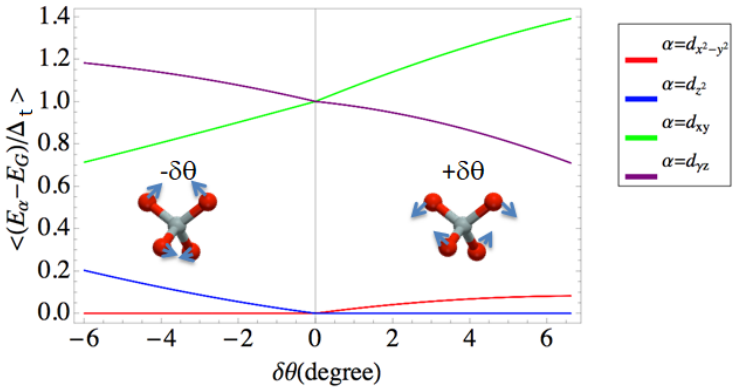

Figure 2.7: Energy levels arising for squeezed (left) and squashed (right) tetrahedra along the z direction as a function of the deviation δ_θ from the ideal position constituted by an angle of $\theta = 109.5°$. E_G is the ground state energy.

of Fig. 2.7, the ground state of the system is constituted by the d_{z^2} orbital, while for negative deformations which are on the left of Fig. 2.7, the lower energy level is the $d_{x^2-y^2}$ orbital, as we expected. The gap which emerges in the e and t_2 subspaces is not of the same amount in the two regions and it is not symmetrical, as one can see evidently in Fig. 2.8.

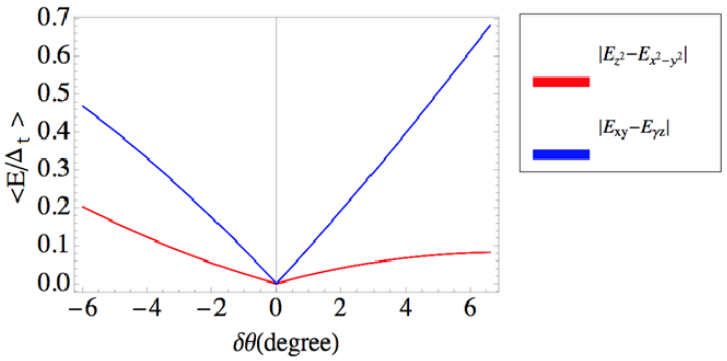

Figure 2.8: Evolution of the energy gap in the e and t_2 subspaces as a function of deviation δ_θ from the ideal position.

We have then demonstrated that, in the case of both squashed and

squeezed tetrahedra, the degeneracy in the e subspace is lifted. When the tetrahedron is squashed, the d_{z^2} orbital is shifted lower with respect to the $d_{x^2-y^2}$ one by an amount Δ_e, while when the tetrahedron is squeezed the opposite ordering occours. In the t_2 sector, an energy gap Δ_{t_2} separates the d_{xy} orbital from the manifold of degenerate d_{yz} and d_{xz} ones. The relative ratio Δ_{t_2}/Δ_e is always greater than 1 in both regions and raises up to several units when the deformation angle increases. Hereafter, we use the ratio Δ_{t_2}/Δ_e to parametrize the degree of distortion instead of the angular deviation $\delta\theta$.

The competition between the SOC and the tetrahedral distortions is analyzed in the following, for the particular case of squashed tetrahedra. We use a typical value of $\Delta_e/\Delta_t = 0.2$ and follow the evolution of the lowest energy eigenvalues as functions of λ/Δ_t and Δ_{t_2}/Δ_e. This evolution is reported in Fig. 2.9.

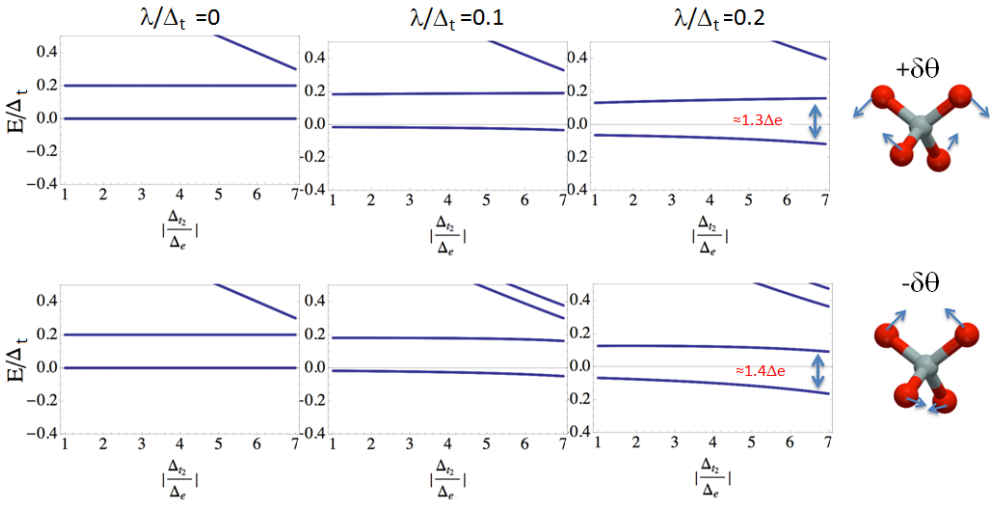

Figure 2.9: Lower energy levels emerging by the interplay between SOC and CF splitting as a function of the ratio between the gaps opened by distortions in the e and t_2 subspaces.

We observe that the original gap Δ_e due to distortions is amplified by the SOC and grows both with the ratio Δ_{t_2}/Δ_e and with λ/Δ_t and it increases by an amount $\sim 1.3\Delta_e$ for a squashed tetrahedron and by $\sim 1.4\Delta_e$ for a squeezed one, as is more evident in Fig. 2.10, where the energy difference among the e orbitals in presence of distortions as a function of the ratio between the "intra" CF splittings for different value of the ratio $\frac{\lambda}{\Delta_t}$ is reported.

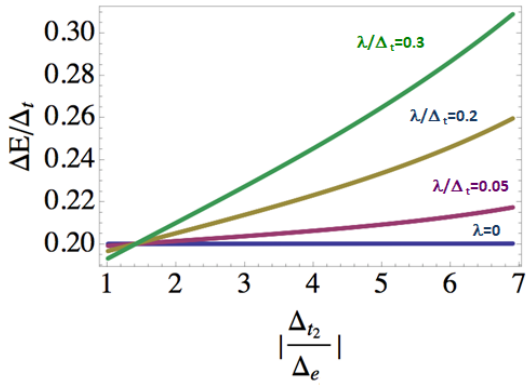

Figure 2.10: Evaluation of the energy difference ΔE among the two lowest eigenvalues of Fig.2.9 for various values of the ratio $\frac{\lambda}{\Delta_t}$

We deduce that, in the presence of tetrahedral distortions, SOC can play a relevant role in setting the energy gap among the lowest energy levels that are involved in the exchange processes. The hierarchy of the lowest energy levels that are involved in the magnetic exchange is strongly affected by SOC and, due to the symmetry breaking in the orbital space, the emerging angular momentum is highly anisotropic due to the preferential action of the L_x and L_y components over the CF-selected d_{z^2} ground state, as reported in Fig. 2.11.

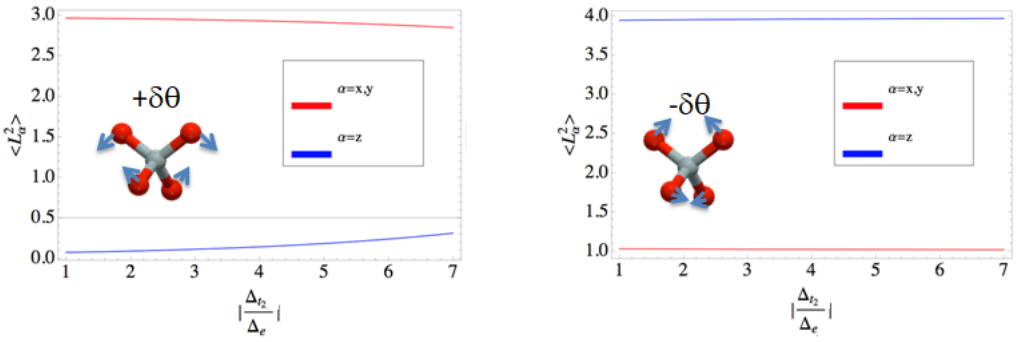

Figure 2.11: Evolution of the local angular momentum components in presence of SOC and deformation

2.6 Summary and conclusion

In this chapter, a brief overview of the CF theory in d orbitals and general remarks about the effect of SOC in TM oxides was provided. In particular, we have analyzed the effects of a large SOC on the magnetic state of a d^1 TM ion located in a tetrahedral environment. Our results show that in the ideal tetrahedral symmetry SOC acts only as a perturbation on the atomic energy levels, set by the CF splitting. Instead, its effects are strongly enhanced in the case of distorted geometries. We have considered the specific case in which the tetrahedron is compressed along the z direction and we have shown that moderate values of the ratio $\frac{\lambda}{\Delta_t}$ can be considered as source of unquenched angular momentum in d^1 systems with tetrahedral coordination. The interplay between SOC and CF parameters may enhance the gap within the set of lowest energy levels in the presence of tetrahedral distortions and leads to magnetic anisotropy.This mechanism is expected to play a relevant role in the magnetic exchange processes of heavy TM oxides in the

d^1 configuration.

Chapter 3

$KOsO_4$ as a case of study

In Chapter 2, we have seen that there is the possibility to strongly enhance at the ionic level the quantum effects of SOC on the e manifold in 5d TMOs oxides containing TMO_4 tetrahedra. We have shown that in a d^1 configuration SOC produces an additional symmetry lowering in presence of a distorted tetrahedral structure. This can lead to an unquenched orbital angular momentum and can affect the hierarchy of the lowest energy levels.

In this chapter, we consider the specific case of the $KOsO_4$ compound to investigate the competition between strong electron correlations, SOC and tetrahedral deformations in the nominally e^1 configuration of the Os^{7+} ions. In this study, we refer to ab-initio calculations based on first-principles Density Functional Theory (DFT) which are reported in Ref. [52]. We characterize the nature of the spin/orbital exchange by performing exact diagonalization (ED) calculations on a two-site cluster and using DFT results as input microscopic parameters of the Hamiltonian. The results show that the SOC is assisting the formation of an AFM ground state but, at the same time,

is responsible for the appearance of a non-vanishing orbital momentum and of a magnetic in-plane and out-of-plane anisotropy. Hence, an entangled spin/orbital state, marked by anisotropic exchange, emerges in a suitable realistic region of interaction parameters. We also show that, due to the peculiar interplay between SOC, Hund's coupling and hopping connectivity, the system is on the verge of developing short range ferromagnetic correlations (FM) marked by strong directionality.

3.1 Ab initio study of $KOsO_4$

In this section, we summarize some results, which have been obtained via ab initio downfolding approach, concerning the on-site energy levels and hopping parameters of $KOsO_4$. These first-principles density functional theory (DFT) calculations have been performed by using the VASP [53] package. As explained in Ref. [52], the core and the valence electrons were treated with the Projector Augmented Wave (PAW) method [54] and a cutoff of 400 eV for the plane wave basis. All the calculation are performed using a 12×12×6 k-point Monkhorst-Pack grid [55]. For the treatment of exchange-correlation, the Local Spin Density Approximation (LSDA) and the Perdew-Zunger[56] parametrization of the Ceperly-Alder[57] data has been considered. In all cases, the tetrahedron method with Blöchl corrections[58] was used for the Brillouin zone integrations. The internal degrees of freedom are optimized by minimizing the total energy to be less than 10^{-5} eV. After obtaining the Bloch wave functions in density functional theory, the maximally localized Wannier functions (MLWF) [59, 60] are constructed using the WANNIER90

code[61]. To extract the character of the electronic bands at low energies, the Slater-Koster interpolation scheme was used. Such an approach is applied to determine the real space Hamiltonian matrix elements in the maximally localized Wannier function basis.

As a second step, to catch the insulating phase, the Hubbard U effects on the Os sites were included within the GGA+U [62] approach using the rotational invariant scheme proposed in [63].

3.1.1 Crystal structure

Both susceptibility and specific heat measurements indicate that $KOsO_4$ compound is a Mott insulator [64]. It has been often synthesized from a mixture of KO_2 and Os metal as a precursor for preparation of the superconductor KOs_2O_6 [65], but further investigations of its physical properties are lacking to date. $KOsO_4$ crystallizes in a tetragonal scheelite-like structure (space group: $I\,4_1/a$, No. 88) [66] schematically reported in Fig. 3.1, with lattice parameters $a = 5.562\mathring{A}$ and $c = 12.664\mathring{A}$. The scheelite structure consists of isolated tetrahedra OsO_4, which are quite well separated. In this compound, the Os atoms sit at the 4a sites $(0, \frac{1}{4}, \frac{1}{8})$, while the O atoms lie on the 16f sites $(0.1320, 0.0160, 0.2028)$. Moreover, the tetrahedra are quite distorted, namely the O-Os-O bond angles are 114° or 107° while the ideal angle for a regular tetrahedron is 109.5° [64]. The $S = 1/2$ spins reside on the sites of an elongated diamond sublattice.

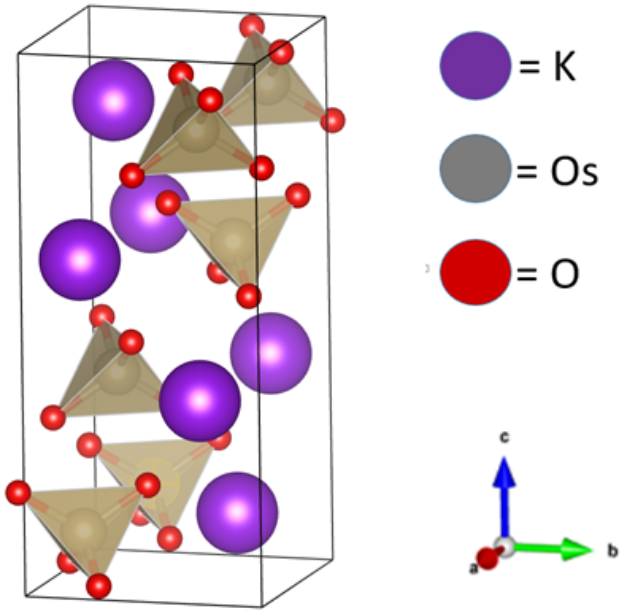

Figure 3.1: Schematical structure of $KOso_4$, consisting in isolated tetrahedra which are quite distorted

3.1.2 Electronic parameters for the paramagnetic phase

We report here the calculation in the paramagnetic (PM) phase at U=0 to have the bare electronic structure. We specify that the (x, y) plane is rotated by an angle $\theta = 73.3°$ with respect to the (a, b) plane of the crystal unit cell and that the on-site energy of the d_{z^2} orbital is assumed as zero. Ab-initio calculations show that the energy of the $d_{x^2-y^2}$ orbital with respect to the ground state z^2 is 99 meV, the energies of d_{xz} and d_{yz} orbitals are equal to 1446 meV, while the energy of the d_{xy} orbital is 1837 meV, as reported in Table 3.1. It is evident that the d_{z^2} sector is separated in energy from the $d_{x^2-y^2}$ orbital by and energy gap of $\sim$ 100 meV; the degeneracy in the e manifold is lifted by the deformation of the OsO_4 tetrahedra, namely the compression along the z axis. This distortion is related to the Jahn Teller

Table 3.1: On-site energy of the Os atoms in the PM case. The on-site energy of the $3z^2$-r^2-like WF is set to zero. ε_0^α is the energy on site for the orbital α. The unit is meV.

	xy	x^2-y^2	xz	yz	$3z^2$-r^2
xy	1837	0	0	0	0
x^2-y^2	0	99	0	0	0
xz	0	0	1446	0	0
yz	0	0	0	1446	0
$3z^2$-r^2	0	0	0	0	0

effect.

Hopping parameters along the xz direction are reported in Table 3.2, while the hopping parameters along the yz direction are reported in Table 3.3 . We indicate them with $t_{1,2}^{\mu,\nu}$, which stands for the hopping integral between the orbital μ at the site 1 and the orbital ν at the neighboring site 2. Hopping amplitudes along different bonds are all equal in magnitude, but can have opposite sign, that changes according to the symmetries and the rotation by 90° degrees that exchanges x and y (see Table 3.2 and 3.3). We also remark that ab-initio calculations in [52] show that the hopping is mostly between nearest neighbors, the largest second neighbour being the $d_{x^2-y^2}/d_{x^2-y^2}$ along x or y, which is estimated around 30 meV. The distance Os-Os for the second-neighbour is $5.562\mathring{A}$, enough to neglect all other hopping terms.

Ab-initio calculation in the magnetic phase, where the FM and the AFM behavior is simulated, have been done [52] and the energy difference $\Delta E = E_{FM} - E_{AFM}$ between these two magnetic phases per Os atom is also reported. Results are shown in Fig. 3.4. The energy difference turns out to increase as a function of the Coulomb repulsion U and to decrease as we

Table 3.2: Hopping integrals between the nearest-neighbor Os atoms in the PM case. Hopping integrals $t_{1,2}^{\alpha,\beta}$ from the site 1 with orbital α to neighboring site 2 with orbital β along the xz direction. The center Os site has coordinates (0.500, 0.250, 0.375). The Os site NN1 has coordinates (0.000, 0.250, 0.125). The energy unit is meV.

	xy	x^2-y^2	xz	yz	$3z^2$-r^2
xy	65	83	-40	55	-138
x^2-y^2	83	35	-123	27	3
xz	-40	-123	4	-28	29
yz	55	27	-28	50	-37
$3z^2$-r^2	-138	3	29	-37	55

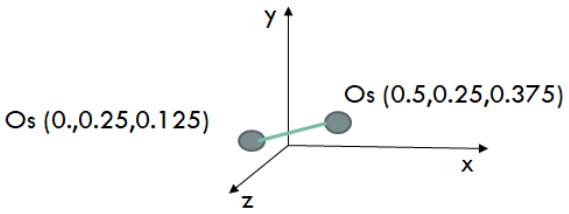

Figure 3.2: Representation of the nearest-neighbor Os atoms of Table 3.2

Table 3.3: Hopping integrals between the Os atoms for the nearest-neighbor in the PM case. Hopping integrals $t_{1,2}^{\alpha,\beta}$ from the site 1 with orbital α to neighboring site 2 with orbital β along the yz direction. The center Os site has coordinates (0.500, 0.250, 0.375). The Os site NN4 has coordinates (0.500,-0.250,0.625). The unit is meV.

	xy	x^2-y^2	xz	yz	$3z^2$-r^2
xy	65	83	-55	-40	138
x^2-y^2	83	35	-27	-123	-3
xz	-55	-27	50	28	-37
yz	-40	-123	28	4	-29
$3z^2$-r^2	138	-3	-37	-29	55

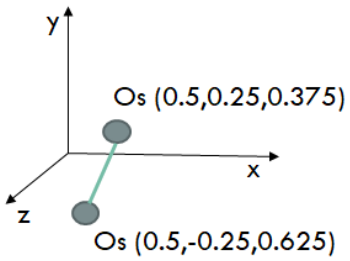

Figure 3.3: Representation of the nearest-neighbor Os atoms of Table 3.3

increase the Hund's parameter J_H. In the range of suitable J_H for the Os atoms, and for the characteristic value of U=2 eV implemented in this calculation, the system is always an antiferromagnet with low Néel temperature but, according to these calculations, ΔE varies from 12-13 to 8-10 meV, for J_H varying from 0 to 500 meV: this reduction of ΔE suggests that the system the system may evolve towards a FM state.

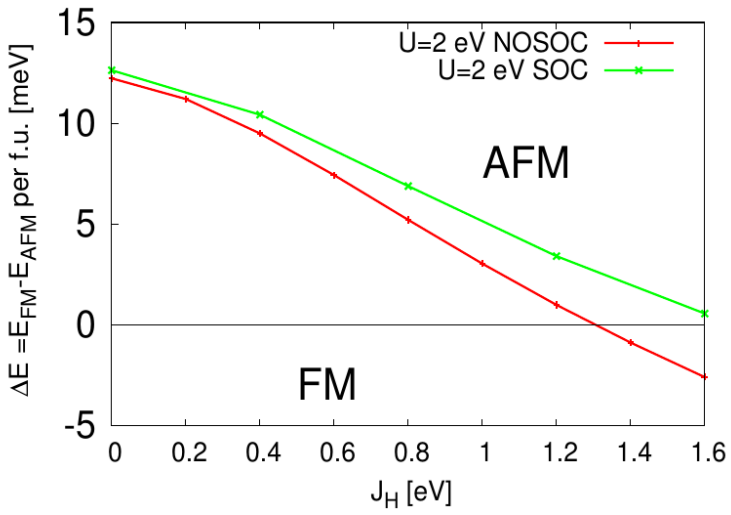

Figure 3.4: Energy difference per formula unit as function of J_H with SOC (green line) and without SOC (red line). The magnetic energy scale is comparable with the spin orbit energy scale in a wide range of the parameters U and J_H.

3.2 Hamiltonian model and Exact Diagonalization

DFT calculations presented in the previous section revealed that $KOsO_4$ has two lower e bands that are split by the tetrahedral deformation and connected via effective hopping amplitudes, which are weak among homologous channels. In such limit, the emergence of an AFM ground state is understood in terms of a superexchange picture favoring AFM correlations among the z^2 bands on the bipartite lattice of the Os ions. As we have seen in the previous chapter [67], the atomic SOC, in presence of a squashed tetrahedral deformation, acts as a source of additional symmetry lowering for SOC-induced lower bands. This interplay is expected to assist the formation of a stronger AFM phase, due to the amplified energy gap among the lowest energy effective z^2 and $x^2 - y^2$ bands.

However, this tendency can be counteracted by the non-trivial interplay between SOC, CF energy and non-vanishing hopping amplitudes, which are dominated by the off-diagonal sector connecting the e and t_2 sectors.

The Hamiltonian model we have chosen in order to investigate this interplay is a multi-band Hubbard model with the addition of a SOC term

$$
\begin{aligned}
H =& U \sum_{i,\mu} n_{i\mu\uparrow} n_{i\mu\downarrow} + \sum_{i,\mu<\nu} (U'_{\mu\nu} - \frac{1}{2} J_{\mu\nu}) n_{i\mu} n_{i\nu} + \sum_{i,\mu} \varepsilon_\mu n_{i\mu} \\
& - 2 \sum_{i,\mu<\nu} J_{\mu\nu} \boldsymbol{S}_{i\mu} \cdot \boldsymbol{S}_{i\nu} + \sum_{i,\mu>\nu} J_{\mu\nu} (d^\dagger_{i\mu\uparrow} d^\dagger_{i\mu\downarrow} d_{i\nu\downarrow} d_{i\nu\uparrow} + d^\dagger_{i\nu\uparrow} d^\dagger_{i\nu\downarrow} d_{i\mu\downarrow} d_{i\mu\uparrow}) \\
& - \sum_{i\neq j,\mu} t_\mu (d^\dagger_{i\mu} d_{j\mu} + h.c.) - \sum_{i\neq j,\mu\neq\nu} \widetilde{t}_{\mu\nu} (d^\dagger_{i\mu} d_{j\nu} + h.c.) + \lambda \boldsymbol{L} \cdot \boldsymbol{S}
\end{aligned}
\tag{3.1}
$$

where i and j stand for the site indices, μ and ν denote the orbitals and $d_{i\mu}$ is the annihilation operator for an electron located at the site i in the orbital μ. U parametrizes the on-site intra-orbital Coulomb repulsion, $U'_{\mu\nu}$ the on-site inter-orbital Coulomb repulsion between orbitals μ and ν, $J_{\mu\nu}$ the Hund's coupling between electrons located in different orbitals at the same site, ε_μ the on-site energy for an electron occupying the orbital μ. Finally, t_μ is the nearest-neighbor orbital-conserving hopping integral for the orbital μ, $\widetilde{t}_{\mu\nu}$ is the nearest-neighbor hopping integral between orbitals μ and ν. The last term in (3.1) represents the spin-orbit interaction with coupling constant λ, $\boldsymbol{L}$ and $\boldsymbol{S}$ being the total orbital angular momentum and spin operators, respectively. The exact relation, dictated by the full symmetry in the d orbital space:

$$
U = U'_{\mu\nu} + 2J_{\mu\nu} \tag{3.2}
$$

has been considered. Furthermore, the cartesian components of the orbital angular momentum $\mathbf{L}$ of a d-electron, already written in matrix form

in Chapter 2, are expressed by:

$$L_x = \sqrt{3}\mathrm{i}d^\dagger_{yz}d_{z^2} + \mathrm{i}(d^\dagger_{yz}d_{x^2-y^2} - d^\dagger_{xz}d_{xy}) + h.c.\ , \tag{3.3}$$

$$L_y = -\sqrt{3}\mathrm{i}d^\dagger_{xz}d_{z^2} + \mathrm{i}(d^\dagger_{yz}c_{xy} + d^\dagger_{xz}d_{x^2-y^2}) + h.c.\ , \tag{3.4}$$

$$L_z = -\mathrm{i}(d^\dagger_{yz}d_{xz} + 2d^\dagger_{xy}d_{x^2-y^2}) + h.c.\ . \tag{3.5}$$

We perform an exact diagonalization (ED) study of the following Hamiltonian on two sites ($i, j = 1, 2$) for a Os d^1 configuration on each site, analyzing the evolution of the relevant correlation functions and the magnetic (spin and orbital) order parameters as functions of SOC λ to characterize the magnetic exchange regimes and the occurrence of magnetic anisotropy.
We use the DFT results of previous section as microscopic parameters of the Hamiltonian: hopping integrals along the xz direction of Table 3.2 are t_μ and $\tilde{t}_{\mu\nu}$ and on-site energies of Table 3.1 are ε_μ. Concerning the others, according to Ref. [68], we can express U, $U_{\mu\nu}$ and $J_{\mu\nu}$ in terms of Racah parameters A, B and C. The value of the intra-orbital Coulomb repulsion U is identical for all the orbitals and it is given by:

$$U = A + 4B + 3C \tag{3.6}$$

We have chosen $U = 2$ eV, which is a reasonable value for $5d$ transition metal oxides [69, 70]. On the other hand, the inter-orbital Coulomb repulsion $U_{\mu\nu}$ and the Hund's coupling $J_{\mu\nu}$ are anisotropic, so their value depends on

the involved orbitals. The value of the Hund's coupling for each pair of orbitals is given in Table 3.4 in terms of the Racah parameters, while we have used Eq. (3.2) for the inter-orbital Coulomb repulsion.

Table 3.4: Interorbital exchange parameters $J_{\mu\nu}$ as functions of Racah parameters B and C

	xy	yz	xz	x^2-y^2	$3z^2$-r^2
xy	0	3B+C	3B+C	C	4B+C
yz	3B+C	0	3B+C	3B+C	B+C
xz	3B+C	3B+C	0	3B+C	3B+C
x^2-y^2	C	3B+C	3B+C	0	4B+C
$3z^2$-r^2	4B+C	B+C	B+C	4B+C	0

We choose to parametrize the orbital dependent $J_{\mu\nu}$ in terms of the parameter J_H, which is referred to the Hund's coupling among t_2 orbitals. For our ED calculations, both theoretical [71] and experimental results [72] indicate that $J_H = 0.3$ eV is a realistic value for $5d$ TM ions. In addition, we have considered a typical value of the ratio C/B relative to transition metal ions [73]; these two elements allow us to determine the Hund's coupling (Table 3.4) and the inter-orbital Coulomb repulsion (Eq. (3.2)) for each pair of orbitals[68], then we can evaluate the following quantities (local electronic density and charge correlations, spin and orbital moment, spin and orbital correlations) as functions of SOC diagonalizing the Hamiltonian of Eq. (3.1).

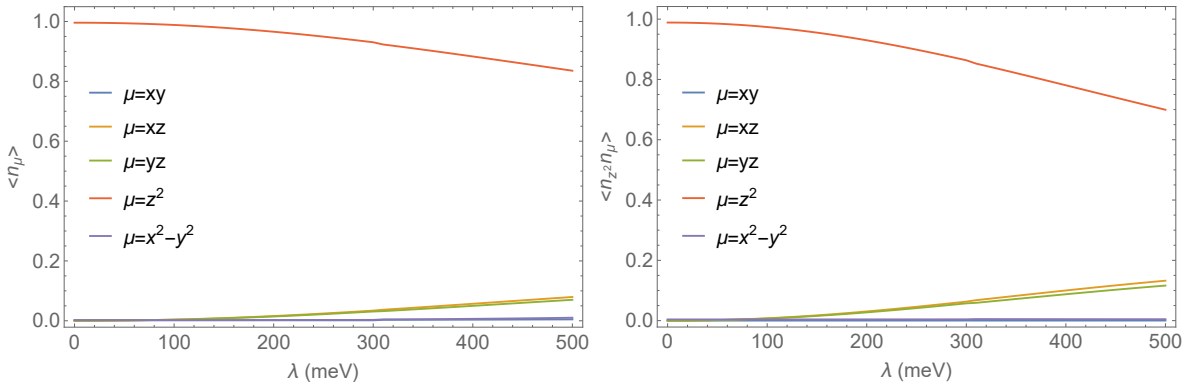

Figure 3.5: Local density charge (left) and charge correlations (right) as function of SOC

3.3 ED results

3.3.1 ED results for local electronic density and charge correlations

In Fig. 3.5, we report the local electronic density $\langle n_\mu \rangle$ (left panel) and charge correlations $\langle n_{z^2} n_\mu \rangle$ (right panel) as function of SOC. Charge is predominantly in the z^2 orbital, this is the reason why we choose to reproduce the correlations of this orbitals with the others. Local density is smoothly reduced from the integer value $< n_{z^2} >=1$, in the absence of SOC, to a not-integer value, which is around 0.9 at $\lambda = 300$ meV, by the small unquenched local angular momentum. Weak correlations with xz and yz orbitals emerge at $\lambda \sim 150$ meV and these become a little stronger increasing λ.

3.3.2 ED results for spin and orbital moment

In Fig. 3.6, we report the squared spin components per site $\langle S_\gamma^2 \rangle$ (left panel) and squared orbital components per site $\langle L_\gamma^2 \rangle$ (right panel) as functions of

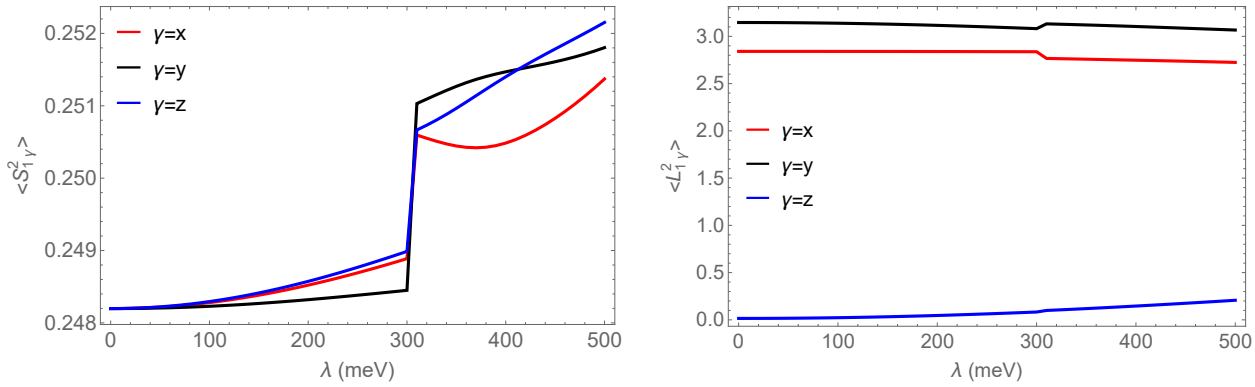

Figure 3.6: Squared spin components per site $\langle S_\gamma^2 \rangle$ (left) and squared orbital components per site $\langle L_\gamma^2 \rangle$ (right) as functions of the SOC λ, with $J_H = 0.3$ eV

λ for $J_H = 0.3$ eV. The system has a fully isotropic spin without SOC: all components are equal and their value is slightly smaller than 0.25 due to quantum fluctuations. This outcome is expected due to the unlifted Kramers degeneracy at each Os site. As regards instead the angular momentum, the quantum number $L = 2$ imposes a sum rule to the squares of its components (they sum up to 6), the x and y components assume very close values (they just feel the differences between the homologous hopping integrals) and the z component is completely quenched, due to the favorable occupation of the d_{z^2} orbitals.

3.3.3 ED results for spin and orbital correlations

In Fig. 3.7, we report the spin correlations $\langle S_{1\gamma} S_{2\gamma} \rangle$ (left panel) and the orbital correlations $\langle L_{1\gamma} L_{2\gamma} \rangle$ (right panel) between homologous components at the two sites as functions of λ for J_H=0.3 eV. The spin correlations are isotropic and antiferromagnetic for $\lambda = 0$: in these conditions, the system

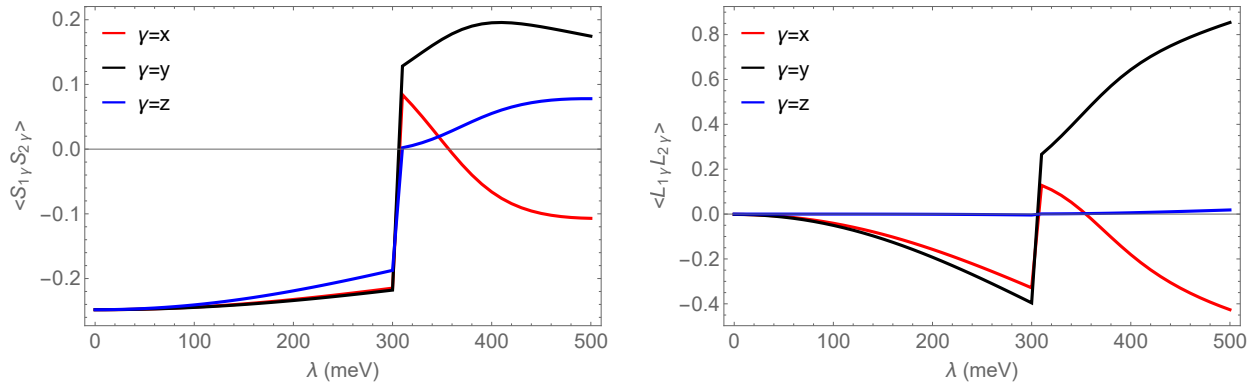

Figure 3.7: Spin correlations $\langle S_{1\gamma} S_{2\gamma} \rangle$ (left) and orbital correlations $\langle L_{1\gamma} L_{2\gamma} \rangle$ (right) between homologous components at the two sites as functions of the SOC λ with $J_H = 0.3$ eV

reproduces the conventional $S = \frac{1}{2}$ Heisenberg antiferromagnet. On increasing λ, a strong anisotropy is induced. In the physical realistic regime of 200 meV$< \lambda <$300 meV, spin correlations are slightly canted along the z direction. This feature is indicative of the SOC-induced anisotropic behavior of the AFM in-plane/out-of-plane spin-correlations, which develops together with weak AF orbital correlations among the modest activated orbital angular momentum.

It is also important to point out that, increasing λ, ferromagnetic (FM) spin correlations appear in the y and z components and the in-plane symmetry is completely broken with the x component of the spin correlations staying antiferromagnetic.

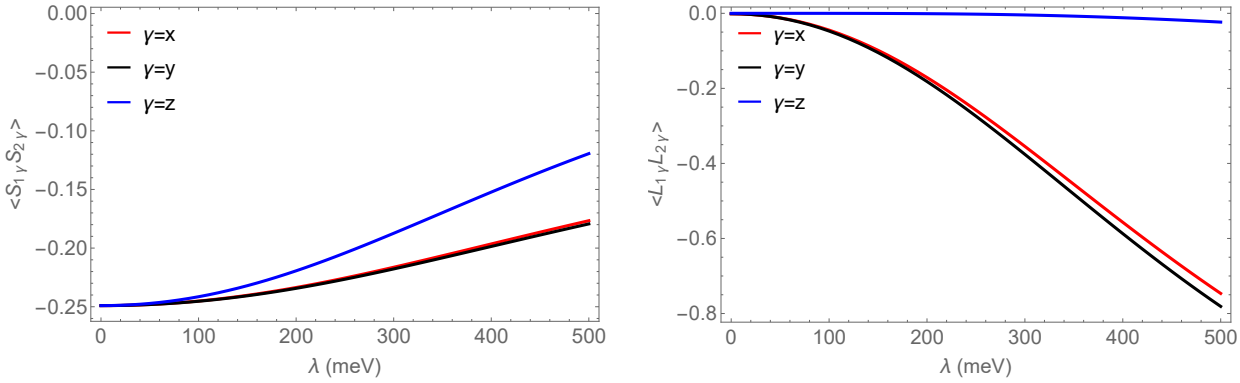

Figure 3.8: Spin correlations $\langle S_{1\gamma}S_{2\gamma}\rangle$ (left) and orbital correlations $\langle L_{1\gamma}L_{2\gamma}\rangle$ (right) between homologous components at the two sites as functions of the SOC λ with $J_H = 0.3$ eV and with $t_{xy,z^2} = 0$ eV

3.4 The role of the hopping parameters and the Hund's exchange

In order to analyze the microscopic mechanism that triggers the proximity to FM correlations, we perform an analysis in the space of the hopping parameters and singled out the dominant role played by the biggest among the e-t_2 parameters in Table 3.2, namely $t_{xy,z^2} = -138$ meV, in setting FM correlations. If the t_{xy,z^2} is assumed to be vanishing, the quantum phase transition is suppressed and one gets canted AFM correlations, as we can see in Fig. 3.8, where we report spin (left) and orbital (right) correlations as a function of SOC assuming $t_{xy,z^2} = 0$ meV.

On the contrary, in the presence of substantial SOC and Hund's coupling, this parameter greatly enhances the FM exchange gain associated with the virtual transitions $d_i^1 d_j^1 \longrightarrow d_i^0 d_j^2 \longrightarrow d_i^1 d_j^1$ from and towards the majority orbital d_{z^2} through the t_2 orbital intermediate state, where the orbital angular momentum is unquenched and the SOC and Hund's energy gain are

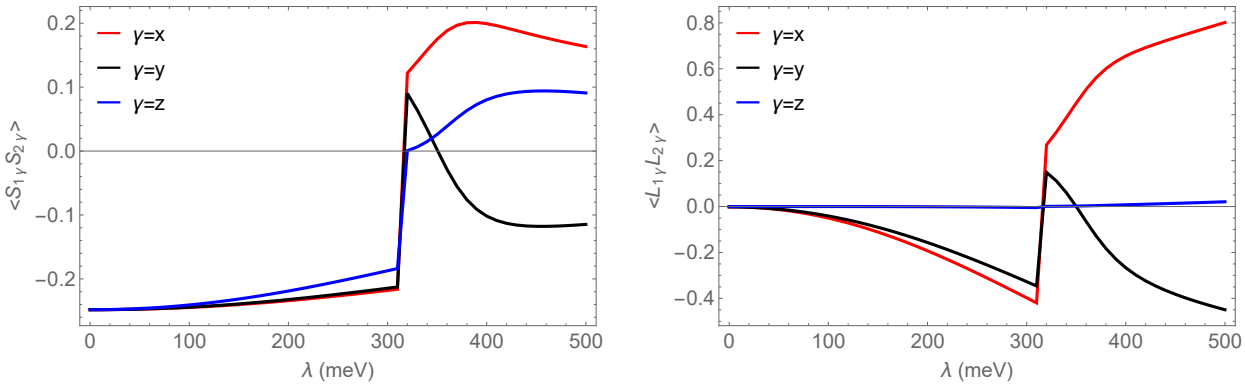

Figure 3.9: Spin correlations $\langle S_{1\gamma} S_{2\gamma} \rangle$ (left) and orbital correlations $\langle L_{1\gamma} L_{2\gamma} \rangle$ (right) between homologous components at the two sites as functions of the SOC λ with $J_H = 0.3$ eV along the yz direction

maximized. The bonding direction also contributes to the final result: if we change the hopping direction, which means that we use the hopping parameters along the yz direction reported in Table 3.3 instead of those of Table 3.2, the x and y components of all the physical quantities get reversed. In order to give an evidence of that, we report in Fig. 3.9 the ED results for spin and orbital correlations as function of SOC substituting in the Hamiltonian the hopping parameters along the yz direction; if we compare this figure with Fig. 3.7, it is evident that this change does not alter neither the qualitative picture nor the quantitative behavior of the physical quantities, if not for the fact that x and y components have exchanged their trend. Such spin correlations are very peculiar and prefigure a link between the bond direction and the sign (FM-AFM) of the exchange coupling per spin component that reminds a Kitaev-type of coupling where all components are active at the same time.

We have also analyzed the evolution of the characteristic value of λ setting the quantum transition from the AFM to the anisotropic FM phase, which

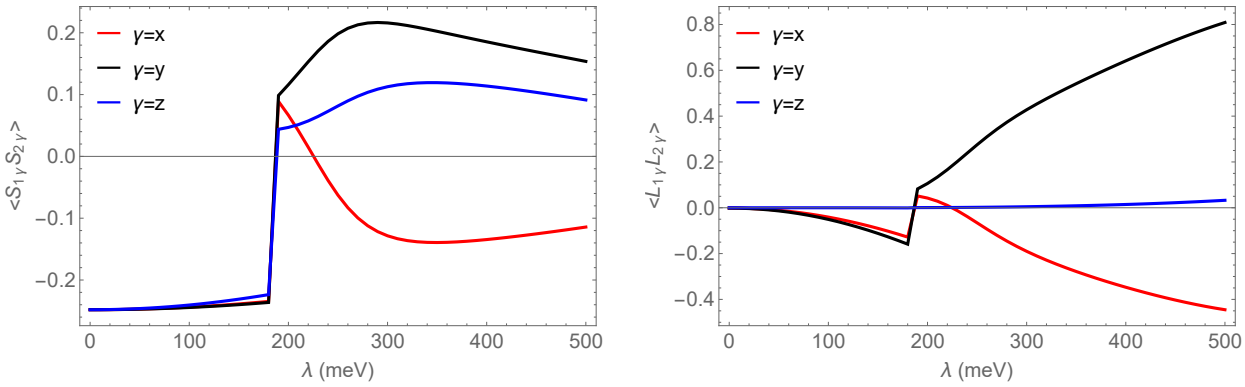

Figure 3.10: Spin correlations $\langle S_{1\gamma} S_{2\gamma} \rangle$ (left) and orbital correlations $\langle L_{1\gamma} L_{2\gamma} \rangle$ (right) between homologous components at the two sites as functions of the SOC λ with J_H=0.4 eV

turns out to be rescaled to lower values by increasing the Hund's coupling, as shown in Fig. 3.10: here, we choose the value $J_H = 0.4$ eV and the transition occurs at smaller value of SOC ($\lambda \sim 180$ meV) than the previous case.

This means that the Hund's exchange endorses the effect of the SOC: on increasing the value of J_H, the anisotropy occurs at smaller value of λ and it is definitely more pronounced.

Such feature reveals an interesting competition among the different quantum configurations contributing to the ground state in systems where those energy scales are actually comparable.

3.5 Summary and conclusions

We have analyzed the consequences of a substantial SOC with respect to the appearance of a non-vanishing orbital momentum and a magnetic anisotropy in the $KOsO_4$. Ab-initio calculations confirm that this compound is an interesting case of study, since the CF splitting is modest respect to the typical

value of the SOC fo $5d$ TM ions. Distortions are an essential ingredient, because SOC has a relevant effect on the lowest e energy levels only if they are not degenerate [67]. We have used the DFT results as microscopic parameters for the Hubbard Hamiltonian which describes the system. Then, we have performed an exact diagonalization of this Hamiltonian, analyzing the evolution of relevant static correlators and magnetic order parameters in order to characterize the magnetic exchange regimes and the occurence of magnetocrystalline anisotropy. It turns up that an entangled spin/orbital state emerges, characterized by an AFM phase with a non-vanishing orbital angular momentum and anisotropy among the in-plane and out-of-plane AFM correlations. In addition, we have demonstrated that SOC plays an active role in setting the boundary between AFM and anisotropic partially-FM correlations, which emerges bond-direction dependent. We demonstrate that this proximity, in a system like $KOsO_4$, is driven by the interplay between substantial SOC and Hund's exchange, and by the hopping connectivity across e-t_2 orbitals. To this end, the actual values of the Hamiltonian parameters are crucial. In particular, the Hund's exchange amplifies the effect of the SOC: on increasing the value of J_H, anisotropy occurs at smaller value of λ.

Chapter 4

Symmetry-protected nodal semimetal in layered systems

In this chapter, we consider an ideal trilayer structure that reminds Ruddlesden-Popper-type compounds, consisting of an almost isolated building block of three heavy TM ions stacked along the z direction. The unit cell is characterized by a low connectivity, which allows to emphasize the local energy scales and particularly the effect of the intrinsic SOC. The study is inspired by the possibility to realize structures which are almost disconnected. This requirement can be realized by considering, for example, systems in which the TM-anionic blocks have not a direct corner or edge sharing configuration. $Sr_xLa_{(11-x)}Ir_4O_{24}$ *(SLIO) compounds are good candidate for this purpose: the structure and the magnetic properties of such new iridate compounds have been very recently reported [74], where the d-electrons count of Ir can be tuned continuously from* $5d^5$ *(*Ir^{4+}*) to* $5d^4$ *(*Ir^{5+}*). The* IrO_6 *octahedra in SLIO are rather isolated from each other and from other TM elements,*

thus minimizing itinerancy. Another path to low kinetic energy is provided by double-perovskite platforms. In general, a double-perovskite material presents two different atoms alternating at the center of the octahedra. Therefore, in the case of a $5d^n$ atom and one with d^0 electronic configuration, the connectivity is reduced, enhancing the electronic correlation. The Hamiltonian model we address possesses several symmetries: besides the time-reversal and the spatial inversion symmetries, which determine the Kramer's degeneracy of the energy levels, the peculiar structure of the trilayer allows an additional symmetry, namely a layer-interchange symmetry. As a consequence, non-trivial topological aspects emerge. By analyzing the evolution of the energy bands, as a function of the microscopic parameters of the model, we verify that symmetry-protected nodal lines arise from the crossing between bands belonging to different layer-interchange symmetry sectors. This analysis may be considered as the starting point for the search of novel topological nodal semimetals, protected by layer-interchange symmetry. We also investigate how the topology of these nodal line changes in the momentum space, by simulating different crystal field local environments and in the limit of weak and strong SOC regime. We identify several kinds of transitions between different topological configurations, characterized by a modification of the shape of the nodal lines .

4.1 Symmetry in topological semimetals

The understanding of topological states of matter has grown enormously in recent years [75]. Topological phases represent new kinds of orders which are

beyond the Landau-Ginzburg paradigm which characterizes different states of matter by the symmetry that they break. There is no local order parameter for topological states of matter, and they distinguish from other phases by the nontrivial topology in their quantum wave functions, which is usually measured in terms of a quantized topological invariant [76]. One of the most striking consequences is the existence of protected gapless surface states, which are insensitive to small perturbations unless passing through a quantum phase transition which destroys the nontrivial topology.

Symmetry also plays an important role for the topology of a quantum state, but not in the way it is intended in symmetry breaking theory. Namely, there exist symmetry protected topological (SPT) phases whose nontrivial topology relies on the presence of symmetries [77, 78, 79]. The most well-known case is represented by topological insulators induced by strong spin-orbit coupling, which represent a classic example of topological band insulators [8]. In these systems strong spin-orbit interactions open up a bulk band gap and give rise to an odd number of band inversions, thereby altering the wave function topology. The nontrivial wave function topology manifests itself at the boundary as an odd number of helical edge states or Dirac cone surface states, which are protected by time-reversal symmetry [80] .

In making a distinction between spin-orbit-induced topological insulators and ordinary insulators, time-reversal symmetry is crucial. However, SPT quantum states can also arise from spatial symmetries, i.e., symmetries that act non locally in position space, such as rotation, reflection, or other space-group symmetries [81].This aspect is particularly relevant when one wants to investigate the topology of non fully gapped nodal systems, such as semimetals

and nodal super-conductors, where the bulk gap closes at certain points in the Brillouin zone (BZ). Nodal systems can exhibit nontrivial band topology. For example, topological semimetals are defined as systems where the conduction and the valence bands cross each other in the Brillouin zone, and the crossing is non-accidental, i.e., cannot be removed by perturbations on the Hamiltonian without breaking any of its symmetries. In those systems, symmetry enforces multiple bands to come together and to become degenerate at a point or along a line in momentum space. In the former case, they are classified as Weyl semimetals [82, 83] and Dirac semimetals [84], that have been intensively studied in theory as well as in experiment. In the latter case, the curve where the bands cross is called a nodal line [85], which may either take the form of an extended line running across the BZ, whose ends meet at the BZ boundary [86], or wind into a closed loop inside the BZ [87], or even form a chain consisting of several connected loops (nodal chain) [88]. Topological semimetals with such line band crossings are called topological nodal line semimetals (TNLSM). The stability of these lines is preserved by the symmetries, especially in systems which present SOC [89]; indeed, TNLSM can be protected by non-spatial symmetries (i.e., time-reversal or particle-hole symmetry) as well as spatial lattice symmetries, or a combination of the two [86]. A schematic illustration of different topological semimetals is given in Fig. 4.1, taken from Ref. [90]. We specify that the previous description is not exhaustive. Several proposal of topological semimetals have shown other possibilities for band degeneracies, stemming from topology. In these cases, a band gap closes at generic $\mathbf{k}$ points and this closing originates not from symmetry, but from topological reason [91]. However, in our case of

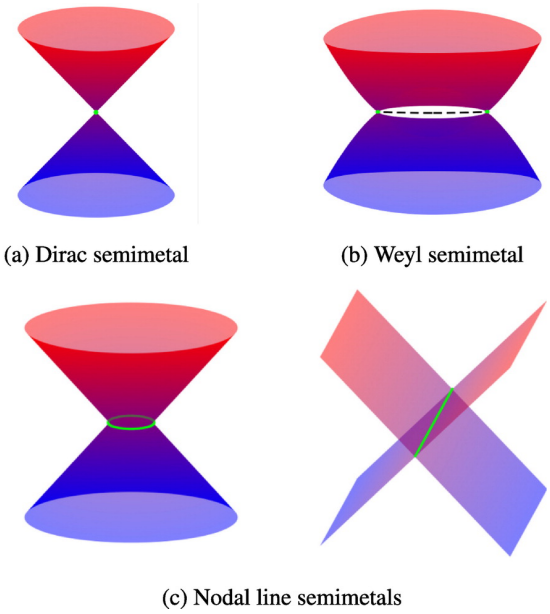

Figure 4.1: Schematic illustration of Dirac node, Weyl node and Nodal line/ ring in momentum space. (a) Schematic of a Dirac semimetal where the bands are linearly dispersed around the Dirac point.(b) Weyl semimetal, in which the Weyl points with opposite chirality are connected by the characteristic Fermi arc. (c) Nodal line semimetals where valence and conduction bands cross along special lines in momentum space forming either a ring-shaped line or 1D line, shown by the green circle/line. [90]

interest symmetries represent a crucial element in order to identify the band crossings. TNLMS may be classified by the behavior of the nodal lines on a symmetry-related plane in the BZ. More generally, different configurations of nodal lines are associated with the topology of Fermi surface, and the transitions between them can be understood as Lifshitz transitions. Originally I.M. Lifshitz [92] introduced the topological transitions in metals, at which the connectedness of the Fermi surface changes. Very recently, they have been applied to TNLSM where a plethora of transitions may be found [93], describing the sudden change of the topology of the Fermi surface between a variety of topologically non equivalent configurations. A schematic illus-

tration of a Lifshitz transition is given in Fig. 4.2, taken from Ref. [93].

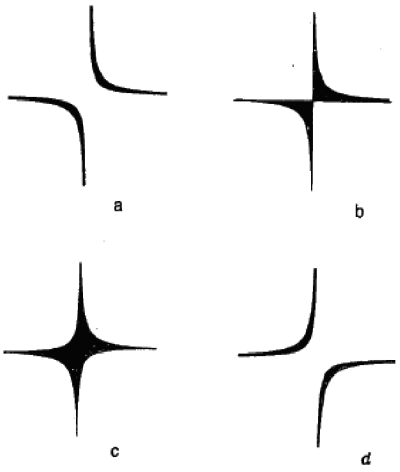

Figure 4.2: An example of a series of Lifshitz transitions with formation and evolution of the flat bands near the saddle point of a 2D spectrum [93]

In this thesis work, we consider a specific problem based on a noninteracting Hamiltonian in presence of intrinsic spin-orbit coupling, describing a trilayer structure, that reminds Ruddlesden-Popper-type compounds, which consists of an almost isolated building block of three heavy TM ions stacked along the z direction. The unit cell is characterized by a low connectivity, which allows to emphasize the local energy scales and particularly the effect of the intrinsic SOC and CF splitting, which cooperate in lifting the orbital degeneracy. Besides the time-reversal and the inversion symmetries, which determine the Kramer's degeneracy of the energy levels, the peculiar structure of the trilayer is responsible for another symmetry, defined as layer-interchange symmetry, which allows to attribute an additional quantum number to the energy levels. In the presence of such symmetries, it is

expected that crossing between bands that have different quantum numbers may occur, which are symmetry protected. On the contrary, in case of no additional symmetry is present, bands with the same quantum numbers hybridize with each other and maintain a gap in-between, through a mechanism known as the band repulsion . In our study, we analyze the quantum phase transitions at which the topology of the energy spectrum changes as a function of the microscopic parameters. In our case, this is easily realized through the tuning of the microscopic tight-binding parameters and the dominating local energy scales set by the CF and SOC. In the specific, we explore the locus of band-crossing momenta over the BZ, without fixing the filling. We show that symmetry preserving topological transitions are possible, through which independent nodal lines can be connected, disconnected, or linked. Here, the term "topological" is referred to the emerging nodal structure of the analyzed system, as we will explain in detail. Our work constitutes an heuristic approach for the search of novel topological nodal semimetals, protected by layer-interchange symmetry. In addition, the exploration from weak up to strong SOC regime may help to scan different topological phases, where nodal lines are either fully gapped or gapped into several nodal points. We specify that the following study constitutes a preliminar analysis of the model, in which ideas for further investigations can be found.

4.2 Trilayered structure and Hamiltonian model

The Ruddlesden-Popper series is a class of layered perovskite structure consisting of two-dimensional perovskite slabs interleaved with cations. The

general formula of the series is $A_{n+1}B_nX_{3n+1}$, where A and B are cations and A is generally constituted by a rare earth element while B is a transition metal, X is the anion, usually the oxygen; n is the number of the layers of octahedra in the perovskite-like stack. In Fig. 4.3, we report an example of this kind of structure: the first image on the left shows a single layer, where n=1; in the center, there in an example of bilayer, where n=2, and the last image on the right represents the trilayer, where n=3.

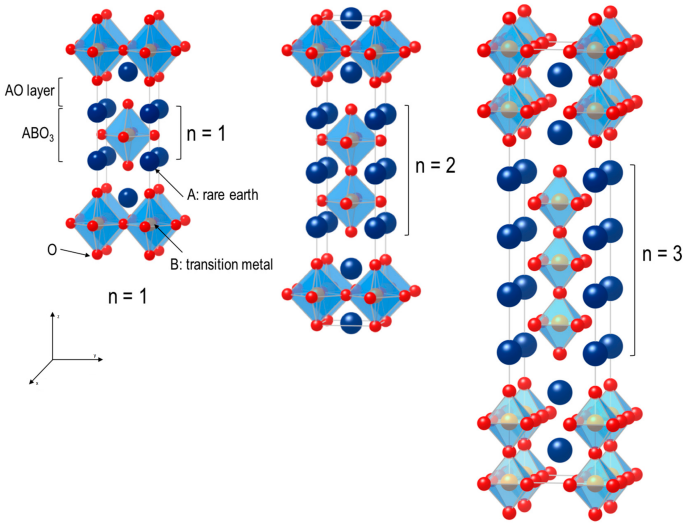

Figure 4.3: Illustration of the Ruddlesden-Popper series, with n equal to 1 (single layer,left), 2 (bilayer,center) and 3 (trilayer,right).

The trilayered system we consider for our study recalls this typical structure: it is constituted by a building block made by TM ions, which are stacked in the z direction and, along this direction, they have a bulk structure in order to avoid boundary effects between the vacuum and the substrate.
Since the trilayered structure is repeated periodically along the z direction, we focus our attention on the unit cell, constituted by three layers. Hereafter, we label the outer layers by indices 2 and 3, the inner layer by index

1. In the ideal cubic structure, the perovskite is characterized by a cation, which is the TM ion, surrounded by an octahedron of anions. We know from Chapter 2 that the five-fold degenerate d levels of a TM ion are split by the CF energy into an upper doublet e_g and a lower triplet t_{2g}. When the system is less than half-filled, one can consider only the t_{2g} orbitals in the study of the energy levels, because their occupation is naturally preferred: this is the reason why the e_g orbitals are "out of picture" of our model. If the cubic symmetry is preserved, this corresponds to three degenerate t_{2g} orbital states for each layer of the unit cell, resulting in 2×9 states, once the spin up and down degeneracy is taken into account. The model we address has the typical structure of a single particle tight binding Hamiltonian and it is constituted by the following contributions:

$$H_k = H_{t_p} + H_{t_o} + H_{\Delta_I} + H_{\Delta_O} + H_{SOC} \tag{4.1}$$

The first term in (4.1) represents the hopping in the (x,y) plane; assuming that it is limited to nearest-neighbors only, it is equal to:

$$H_{t_p} = \sum_{\mathbf{k}} [-4t_{xy}(\cos k_x + \cos k_y) - 4t_{xz} \cos k_x - 4t_{yz} \cos k_y] c^{\dagger}_{\mathbf{k}} c_{\mathbf{k}} \tag{4.2}$$

The next term of (4.1) is constituted by the intra-cell hopping, which only involves hopping between the γz orbitals (xz,yz) of different layers. It

can be written as follows:

$$H_{t_o} = t_o \sum_{\alpha=\gamma z,\sigma} c^{\dagger}_{\alpha\sigma} c_{\alpha\sigma} + h.c. \tag{4.3}$$

The other contributions are related to the on-site energies, which are tuned to simulate CF splitting in the trilayered structure and can be expressed as:

$$H_{\Delta_I} = \sum_{\alpha,\sigma} \varepsilon_\alpha n_{\alpha_1\sigma} \qquad H_{\Delta_O} = \sum_{\alpha,\sigma} \varepsilon_\alpha n_{\alpha_2\sigma} + \sum_{\alpha,\sigma} \varepsilon_\alpha n_{\alpha_3\sigma} \tag{4.4}$$

where α labels the xy and γz orbitals, σ is the spin index and the indices 1,2,3 are related to the inner and the outer layers respectively.

Recalling the T-P equivalence explained in Chapter 2, The SOC Hamiltonian can be written as:

$$H_{SOC} = \lambda \tilde{\mathbf{l}} \cdot \mathbf{S} \tag{4.5}$$

where S=$\frac{1}{2}$ and $\tilde{l}$=1 is the effective orbital angular momentum.

By assuming that the eighteen basis state are ordered in the following way: $|xy_{1\uparrow}, xz_{1\uparrow}, yz_{1\uparrow}, xy_{2\uparrow}, xz_{2\uparrow}, yz_{2\uparrow}, xy_{3\uparrow}, xz_{3\uparrow}, yz_{3\uparrow}, xy_{1\downarrow}, xz_{1\downarrow}, yz_{1\downarrow}, xy_{2\downarrow}, xz_{2\downarrow}, yz_{2\downarrow}, xy_{3\downarrow}, xz_{3\downarrow}, yz_{3\downarrow}>$, we can write separately the contributions to the matrix representation of the terms constituting the Hamiltonian (4.1) . The in-plane hopping matrix can be written in blocks:

$$H_{t_p} = \begin{pmatrix} P & 0 & 0 & 0 & \dots & 0 \\ 0 & P & 0 & 0 & \dots & 0 \\ 0 & 0 & P & 0 & \dots & 0 \\ 0 & \dots & 0 & P & 0 & 0 \\ 0 & \dots & 0 & 0 & P & 0 \\ 0 & \dots & 0 & 0 & 0 & P \end{pmatrix} \tag{4.6}$$

Where P is a 3×3 matrix equal to:

$$P = \begin{pmatrix} -4t_{xy}(\cos k_x + \cos k_y) & 0 & 0 \\ 0 & -4t_{xz}\cos k_x & 0 \\ 0 & 0 & -4t_{yz}\cos k_y \end{pmatrix} \tag{4.7}$$

Hereafter, we assume t_{xy}=t_{xz}=t_{yz}=t_p.

The intra-cell hopping cannot be written in blocks, because it connects states belonging to different layers. The typical structure of its matrix representa-

tion in a fixed spin sector is:

$$H^{\sigma}_{t_o} = \begin{pmatrix} 0 & 0 & 0 & 0 & 0 & 0 & 0 & 0 & 0 \\ 0 & 0 & 0 & 0 & t_o & 0 & 0 & t_o & 0 \\ 0 & 0 & 0 & 0 & 0 & t_o & 0 & 0 & t_o \\ 0 & 0 & 0 & 0 & 0 & 0 & 0 & 0 & 0 \\ 0 & t_o & 0 & 0 & 0 & 0 & 0 & 0 & 0 \\ 0 & 0 & t_o & 0 & 0 & 0 & 0 & 0 & 0 \\ 0 & 0 & 0 & 0 & 0 & 0 & 0 & 0 & 0 \\ 0 & t_o & 0 & 0 & 0 & 0 & 0 & 0 & 0 \\ 0 & 0 & t_o & 0 & 0 & 0 & 0 & 0 & 0 \end{pmatrix} \tag{4.8}$$

where $\mathrm{H}_{t_o ij} \neq 0$ if i and j correspond to two analogous γz orbitals of different layers.

The CF contribution(4.4) assumes the form:

$$H_{\Delta_I} + H_{\Delta_O} = \begin{pmatrix} D1 & 0 & 0 & 0 & \dots & 0 \\ 0 & D2 & 0 & 0 & \dots & 0 \\ 0 & 0 & D3 & 0 & \dots & 0 \\ 0 & \dots & 0 & D1 & 0 & 0 \\ 0 & \dots & 0 & 0 & D2 & 0 \\ 0 & \dots & 0 & 0 & 0 & D3 \end{pmatrix} \tag{4.9}$$

Where

$$D1 = \begin{pmatrix} \Delta_I & 0 & 0 \\ 0 & 0 & 0 \\ 0 & 0 & 0 \end{pmatrix} \quad D2 = \begin{pmatrix} \Delta_{O2} & 0 & 0 \\ 0 & 0 & 0 \\ 0 & 0 & 0 \end{pmatrix} \quad D3 = \begin{pmatrix} \Delta_{O3} & 0 & 0 \\ 0 & 0 & 0 \\ 0 & 0 & 0 \end{pmatrix} \tag{4.10}$$

In this expressions, Δ_{O2} and Δ_{O3} are two positive constants measuring the energy gap between the xy and γz orbitals of the outer layers, Δ_I is the corresponding quantity relative to the inner layer. We are then assuming that there is a compression/elongation of the octahedra along the z axis and that it is different in principle for the outer and the inner layer. Moreover, in writing (4.9), we assumed that the energy of the t_{2g} orbitals is measured with respect to the γz orbitals, then Δ_I is identified with the energy of the xy orbital of the inner layer, while Δ_{O2} and Δ_{O3} represent the xy orbital energies of the outer layers.

The SOC term (4.5) mixes the spin and orbital angular momenta and its matrix form was already given for a single ion in Eq. (2.39) of Chapter 2.

4.2.1 Symmetry properties of the model

The peculiar structure of the trilayer and the adopted model Hamiltonian may have an influence on the energy spectrum through the symmetry properties which characterize it. Time reversal and inversion symmetry hold in the chosen model.

Time reversal operator is given by the antiunitary operator

$$\tau = e^{i\Phi}\sigma_y \tag{4.11}$$

where σ_y is the Pauli matrix and Φ is an arbitrary phase which depends on the chosen basis. The choice of Φ has no physical consequence and does not change the value of any physical observables. For spin $\frac{1}{2}$ electrons, τ has the property τ^2=-1.

The inversion $\mathscr{P}$ is a unitary operator which flips the sign of the spatial coordinates:

$$\mathscr{P}\Psi(r) = e^{i\frac{\Phi}{2}}\Psi(-r) \tag{4.12}$$

The operator $\mathscr{P}$ maps $\mathbf{k} \to -\mathbf{k}$ and satisfies $\mathscr{P}^2$=1. Since the Hamiltonian (4.1) has both inversion symmetry $\mathscr{P}$ and time-reversal τ, we get a global antiunitary symmetry $\tau \otimes \mathscr{P}$, which leads to an important constraint, known as Kramer's theorem, which asserts that all eigenstates of the Hamiltonian are at least twofold degenerate for every value of $\mathbf{k}$.

In the case of equivalent outer layers $\Delta_{O2} = \Delta_{O3}$, the Hamiltonian shows an additional symmetry, which we call layer-interchange symmetry $\mathscr{F}$.Such symmetry is associated to a transformation which consists in the "exchange" of the homologous orbital states belonging to the outer layers, by conserving the spin. Since $\mathscr{F}^2$=1, the eigenstates of the Hamiltonian may be classified in two subspaces satisfying:

$$\mathscr{F}\left|\Psi\right\rangle = -\left|\Psi\right\rangle, \qquad \mathscr{F}\left|\Psi\right\rangle = \left|\Psi\right\rangle \tag{4.13}$$

respectively. The states for which $\mathscr{F}$=-1 are called non- bonding states, while the states for which $\mathscr{F}$=1 are the bonding and antibonding states. This observation implies that we can classify each state with an extra quantum number, defined as the layer parity f of such state, which assumes values ± 1.

In summary, by diagonalizing the Hamiltonian (4.1) we obtain nine energy bands which are doubly degenerate as stated by the Kramer's theorem. If the outer layers are equivalent, according to the layer- interchange symmetry, we can classify these nine bands by layer parity f, associating to each of them $f = \pm 1$ depending on the eigenvalue of the layer-interchange operator.

4.3 Preliminary analysis in the unit cell

Hereafter, we assume Δ_{O2}=Δ_{O3}, then the layer-interchange symmetry is valid. Therefore, the classification of the states by parity (bonding, anti-bonding, non-bonding) is used. In the following, we explore the transition across different topological phases that may arise by changing the microscopic parameters and which are protected by the layer-interchange symmetry.

4.3.1 Lifting of the orbital degeneracy driven by inner and outer CF

In this section, we perform a preliminary characterization of the local energy levels of a single unit cell in terms of the layer- interchange symmetry. We point out that, in the ideal cubic structure, the bonding, non bonding and antibonding sectors are still degenerate, due to the threefold t_{2g} subspace. The introduction of the CF splitting and SOC terms may reduce the orbital degeneracy, by opening a gap among states belonging to the same layer- interchange symmetry sectors. In the next sections, we will demonstrate how those gap openings may manifest in the band structure across the BZ, once

the in-plane itinerancy is restored in a perturbative way.

We start the analysis by considering an ideal undistorted geometry in absence of SOC. The diagonalization of the Hamiltonian (4.1) for t_p=0 gives as output only three different eigenvalues, which build up three degenerate blocks schematically shown on the left side of Fig. 4.4 .

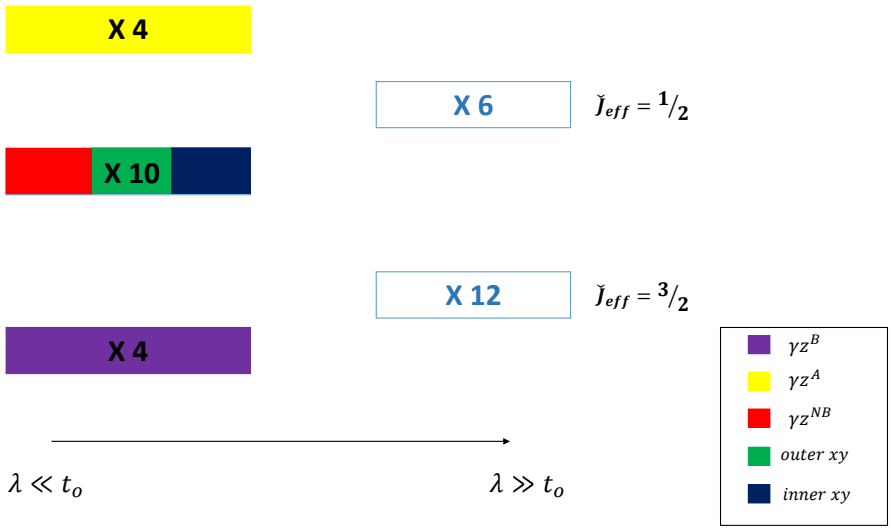

Figure 4.4: Schematic evolution of the energy levels of the unit cell Hamiltonian as functions of orthogonal hopping t_o and SOC λ without CF distortions. When λ«t_o, three degenerate energy levels emerge, while in the limit of λ»t_o, the system evolves into two blocks, constituted by two multiplets consisting of six and twelve levels respectively. The values of the effective total angular momentum $\tilde{J}_{eff}$, which are referred to each layer, are also indicated.

The lower block is constituted by the bonding γz states γz^B, while the upper block is composed by the antibonding γz states γz^A (each of them with spin up and down); in the central block, there are non-bonding γz states γz^{NB} and the six xy local energy states.

Adding the crystal field contributions Δ_O and Δ_I, we may simulate different

local environments and partially lift the orbital degeneracy. In particular, we can obtain different distorted geometries, where the octahedra are elongated or compressed along the z axis, depending on the sign attributed to Δ_O and Δ_I. Since we choose to measure the one-site orbital energy with respect to the γz orbitals, positive (negative) values of Δ_O and Δ_I will raise (lower) the energy of the outer and inner xy orbitals with respect to the γz^{NB}. In Figure 4.5 and 4.6, we report the schematics of all the possible configurations that can be obtained by considering different choices of the CF terms Δ_O and Δ_I.

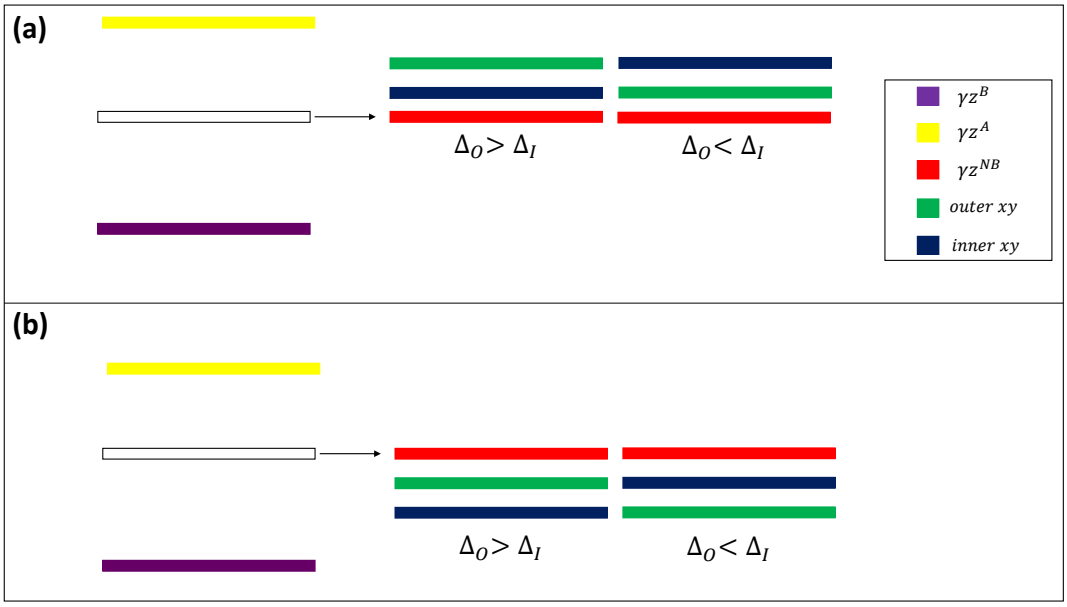

Figure 4.5: Schematic representation of the orbital configurations obtained by diagonalizing the Hamiltonian (4.1) at t_p=0 with Δ_O and Δ_I concordant and positive (a) or negative (b).

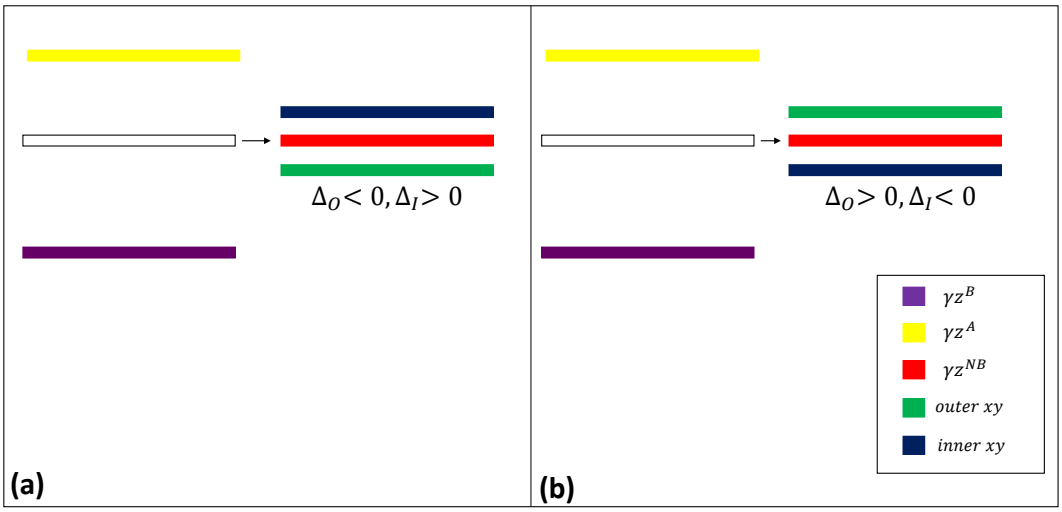

Figure 4.6: Schematic representation of the orbital configurations obtained by diagonalizing the Hamiltonian (4.1) at t_p=0 with Δ_O<0 and Δ_I>0 (a) or Δ_O>0 and Δ_I<0 (b).

4.3.2 Lifting of the orbital degeneracy driven by Spin Orbit Coupling

In the next step of our analysis, we consider the effect of the SOC on the evolution of the energy levels of the Hamiltonian describing the unit cell. In particular, we discuss two representative cases, where Δ_I and Δ_O are assumed to be unequal and discordant as depicted in Fig. 4.6 (a) and (b). We choose to express all the parameters of the model in units of t_o. Fig. 4.7 and 4.8 show the evolution of the energy levels as function of λ for the specific cases of $\frac{\Delta_I}{t_o}$=-0.2, $\frac{\Delta_O}{t_o}$=0.5 and $\frac{\Delta_I}{t_o}$=0.2, $\frac{\Delta_O}{t_o}$=-0.5. Each level is marked with a color which is representative of its layer parity value *f*. As one can see, by adding the SOC, the orbital degeneracy which characterizes the local energy states at

λ=0 is fully removed. However, the splitting and the hierarchy of the energy levels are very specific for a given choice of the inner and outer CF, meaning that the interplay between those two parameters is highly nontrivial.

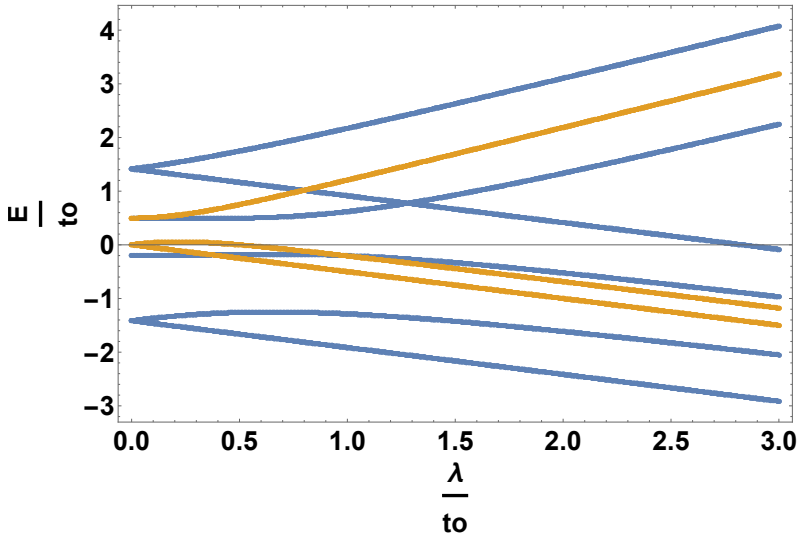

Figure 4.7: Evolution of the energy levels as function of λ. Blue energy levels are characterized by f=1, while orange ones have f=-1. All the parameters are expressed in unit of t_o. Here, $\frac{\Delta_I}{t_o}$=-0.2 and $\frac{\Delta_O}{t_o}$=0.5

We also observe that for such choice of the CF parameters, levels from the 3^{rd} to the 8^{th} in ascending order meet at degeneracy points, when λ is increased. Levels with opposite parity become degenerate at some value of λ, thus determining the subsequent exchange of f in the sequence of the parity of levels. We distinguish two regions: for small values of λ, Fig. 4.7 shows a crossing between levels 3 and 4, while in Fig. 4.8 crossing between levels 6 and 7 arises; for moderate/large value of SOC, crossing is obtained for 4,5 and 7,8 levels in both cases. The detected crossings between energy levels in this analysis will be the starting point of the next exploration, which includes the introduction of the in-plane hopping.

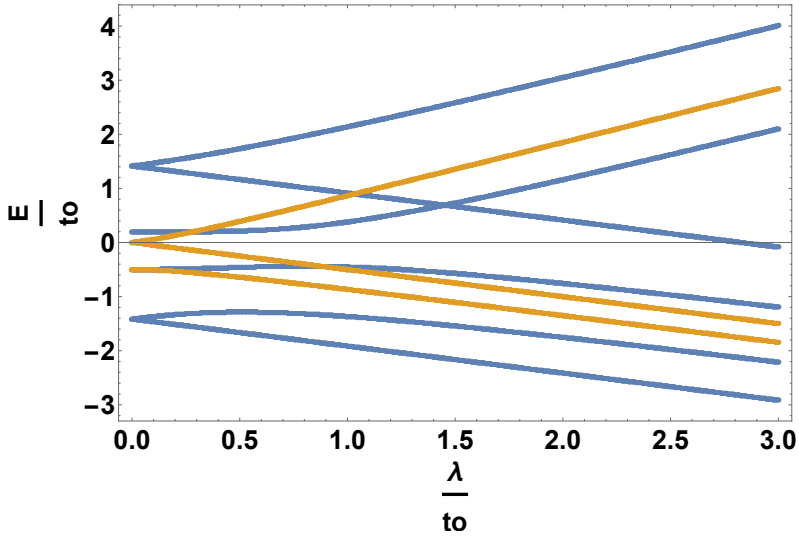

Figure 4.8: Evolution of the energy levels as function of λ. Blue energy levels are characterized by f=1, while orange ones have f=-1. All the parameters are expressed in unit of t_o. Here, $\frac{\Delta_I}{t_o}$=0.2 and $\frac{\Delta_o}{t_o}$=-0.5.

4.4 Nodal lines of the trilayer structure

4.4.1 Topology of the band structure

When $t_p \neq 0$, electrons can move in the xy plane and this give us the possibility to explore the electronic band structure of the trilayer, searching for crossing points between two bands with opposite layer parity. Crossing points between bands which belong to different layer-interchange symmetry sectors are relevant, because they may be symptomatic of a symmetry-protected topological phase of the system. We perform preliminary calculations obtaining band structure plots, which show the eigenvalues $E_n(\mathbf{k})$ of the Hamiltonian (4.1) for different values of $\mathbf{k}=(k_x,k_y)$ along straight lines connecting high symmetry points. For the trilayered structure, the high symmetry points of the Brioullin zone associated to the lattice are represented by the Γ point,

which has coordinates (0,0), the X point, which has coordinates (π,0), and the M point, which has coordinates (π,π). They are schematically reported in Fig. 4.9. The appearance of a crossing point between two bands with

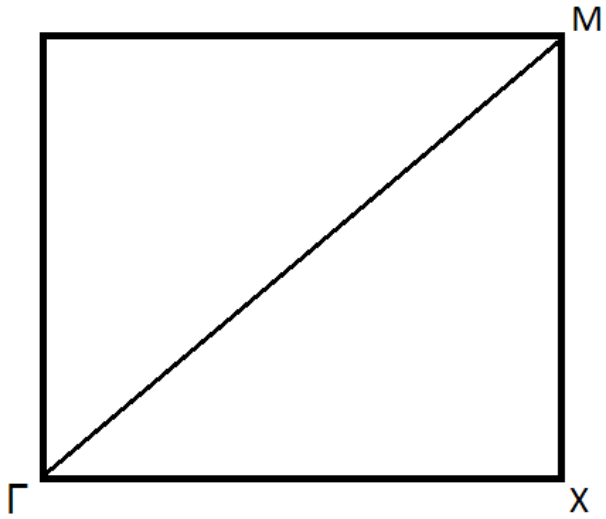

Figure 4.9: Part of the Brioullin zone of the square lattice which characterizes the trilayer. Γ point has coordinate (0,0), the X point has coordinate (π,0), the M point has coordinate (π,π).

opposite f means that, along the chosen direction, an inversion of the layer parity associated to the mentioned bands has happened.

Hereafter, we fix the value of the in-plane hopping t_p in unit of t_o to $\frac{t_p}{t_o}$=0.1. The relative small value of t_p makes the trilayered structure almost "disconnected", in the sense that the connectivity of the system is highly lowered. However, the kinetic energy gain is such that gap closings, which are symmetry-protected, may occur at some **k**.

We have performed a careful exploration of all the band crossings that may occur in various regimes of the microscopic parameters. By way of example, we reproduce band structure plots along the ΓX ,XM and ΓM direc-

tions,respectively, in Fig. 4.10 and 4.11 for a representative case in which $\frac{\Delta_I}{t_o}$=-0.2 , $\frac{\Delta_O}{t_o}$=0.5 and $\frac{\lambda}{t_o}$=0.2.

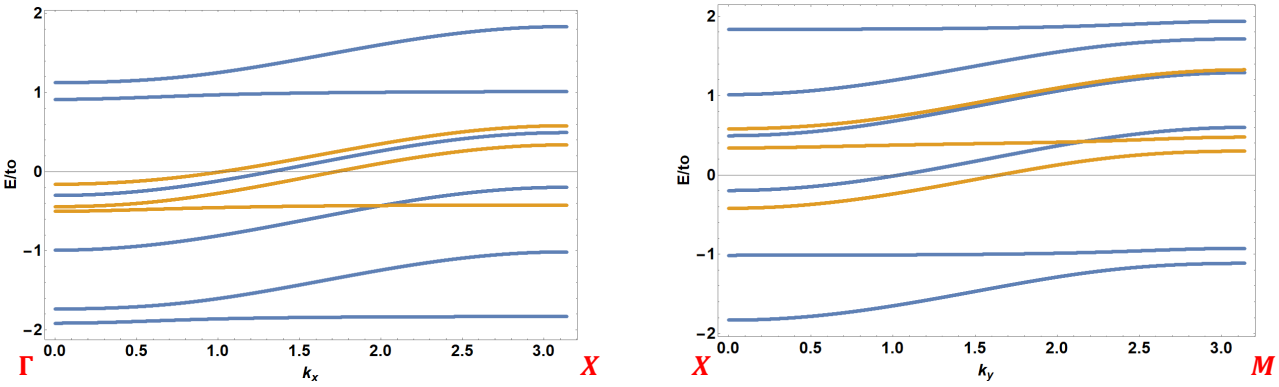

Figure 4.10: Band structure plot along ΓX (left) and XM (right) direction with $\frac{t_p}{t_o}$=0.1, $\frac{\Delta_I}{t_o}$=-0.2 , $\frac{\Delta_O}{t_o}$=0.5 and $\frac{\lambda}{t_o}$=0.2. Blue energy bands are characterized by f=1, while orange ones have f=-1.

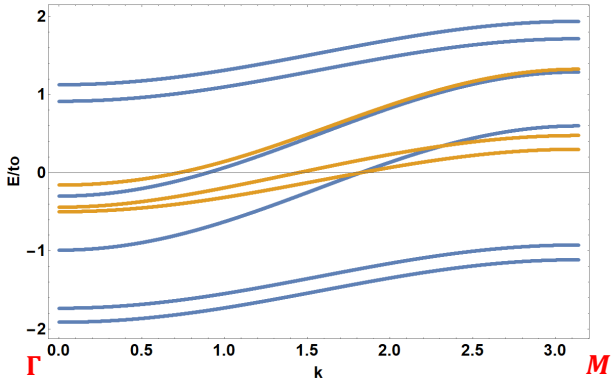

Figure 4.11: Band structure plot along ΓM direction with $\frac{t_p}{t_o}$=0.1, $\frac{\Delta_I}{t_o}$=-0.2 , $\frac{\Delta_O}{t_o}$=0.5 and $\frac{\lambda}{t_o}$=0.2. Blue energy bands are characterized by f=1, while orange ones have f=-1.

4.4.2 Phase diagrams

For each pair of bands which manifest crossing points in the band structure plots that were explored as explained in the previous section, we have ex-

amined the corresponding evolution by varying Δ_I and λ and by keeping fixed the value of Δ_O and t_p. We attribute to each band crossing an integer, namely an invariant $\mathscr{I}$, which is defined as the total number of band inversions of the pair of bands we are interested in. This invariant is equal to zero when two bands have no crossings or cross an even number of times, while it is equal to 1 if there is an odd number of crossings.In topological semimetals, one can associate with each band crossing a topological invariant, whose form depends on the symmetry group that protects the nodal structure [94].This invariant gives a quantitative description of the topology of the system. In this context, we do not refer to this specific kind of topological invariant, namely it is not constituted by $\mathscr{I}$, but our analysis may be considered as a preliminary study in order to calculate it. We report in specific phase diagrams the contour maps describing the regions of the parameter space, characterized in terms of the invariant $\mathscr{I}$ for each of the high symmetry paths: we denote by $\mathscr{I}_{\Gamma X}$ the invariant evaluated along the ΓX direction,$\mathscr{I}_{XM}$ the invariant evaluated along the XM direction and $\mathscr{I}_{\Gamma M}$ its value along the ΓM direction.

Fig. 4.12, 4.13 and 4.14 represent the phase diagrams relative to band 4 and band 5 along ΓX, XM and ΓM directions, respectively, for the specific case of $\frac{\Delta_O}{t_o}$=0.5 and $\frac{t_p}{t_o}$=0.1. Looking at the phase diagrams, we can recognize the alternation of two sections: in one of them, the invariant is equal to zero, in the other the invariant is equal to 1.

The value of the fixed parameters has a crucial role: if we change the value of $\frac{\Delta_O}{t_o}$=-0.5, the phase diagrams which we obtain for the same pair of bands (band 4 and 5) look very different. They are reported in Fig. 4.15 and 4.16.

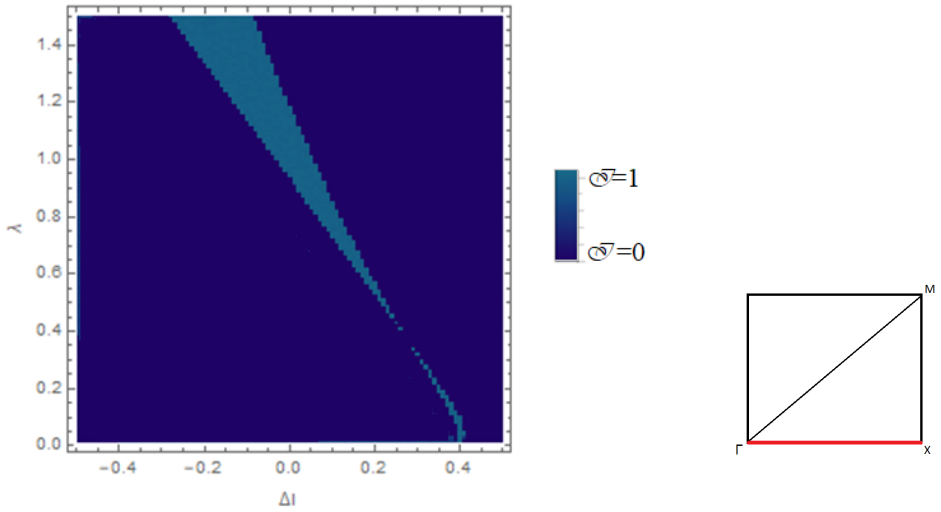

Figure 4.12: Phase diagram of band 4 and 5 along ΓX direction, as indicated by the red line in the figure on the right, for $\frac{\Delta_O}{t_o}$=0.5 and $\frac{t_p}{t_o}$=0.1. The blue zone corresponds to the value 0 of the invariant, while the light blue zone is relative to the value 1 of the invariant.

4.4.3 Analysis of the transitions

By varying the λ and Δ_I parameters in the previous phase diagrams, one describes the quantum phase transitions between phases characterized by a different topology of the energy spectrum. The local topology of each nodal structure involving a particular pair of crossing bands has been characterized by means of the invariant $\mathscr{I}$ evaluated along every high- symmetry path ($\mathscr{I}_{\Gamma X}$,$\mathscr{I}_{XM}$,$\mathscr{I}_{\Gamma M}$). In this section, we will look at several kinds of symmetry preserving transitions through which the nodal lines may evolve, when moving across different regions of the phase diagrams. We will consider both weak and strong SOC limit.

We start by considering the phase diagrams of Fig.4.12,4.13 and 4.14. For $\frac{\lambda}{t_o}$=0.2, we vary Δ_I in the interval 0.34≤ $\frac{\Delta_I}{t_o}$ ≤0.35. Along this evolution,

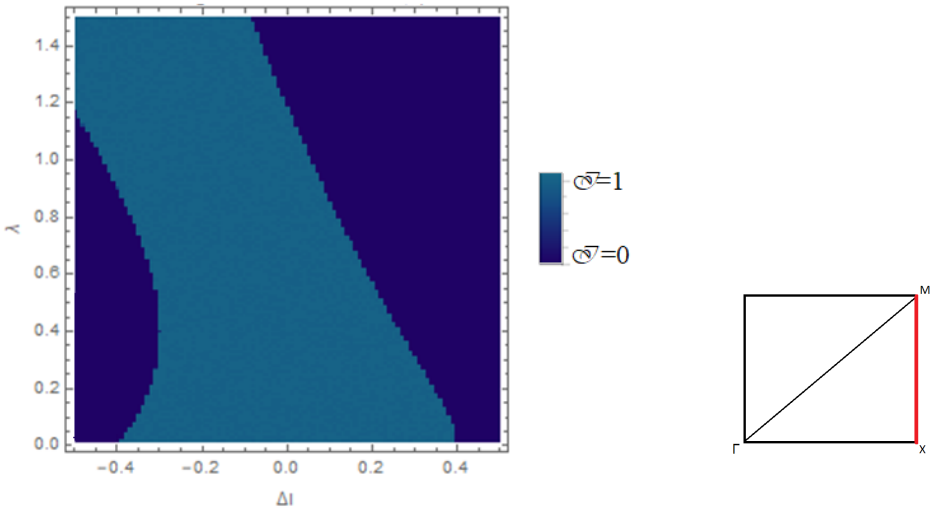

Figure 4.13: Phase diagram of band 4 and 5 along XM direction, as indicated by the red line in the figure on the right, for $\frac{\Delta_O}{t_o}$=0.5 and $\frac{t_p}{t_o}$=0.1. The blue zone corresponds to the value 0 of the invariant, while the light blue zone is relative to the value 1 of the invariant.

we can distinguish three distinct kinds of transition: $\mathscr{I}_{\Gamma X}$ goes from 0 to 1, $\mathscr{I}_{XM}$ goes from 1 to 0 while $\mathscr{I}_{\Gamma M}$ remains equal to 1. We encode such transition as 011 → 101, where each of the three numbers represent the value of the invariant along the ΓX, XM and ΓM direction, respectively. One can follow the evolution of the nodal points associated to each band crossing in the chosen region of parameters. Results of this analysis are shown in Fig. 4.17.

In the first panel on the left, $\frac{\Delta_I}{t_o}$=0.34 and the nodal line intercepts the XM and the ΓM direction, which means that band 4 and 5 have a crossing point and thus an inversion along those directions. This is coherent with the mapping 011 which we extract from the phase diagrams of Fig. 4.12,4.13 and 4.14. In the second panel, $\frac{\Delta_I}{t_o}$=0.343 and the topology of the line has changed: the nodal line collapses in the ΓX direction. This means that, along

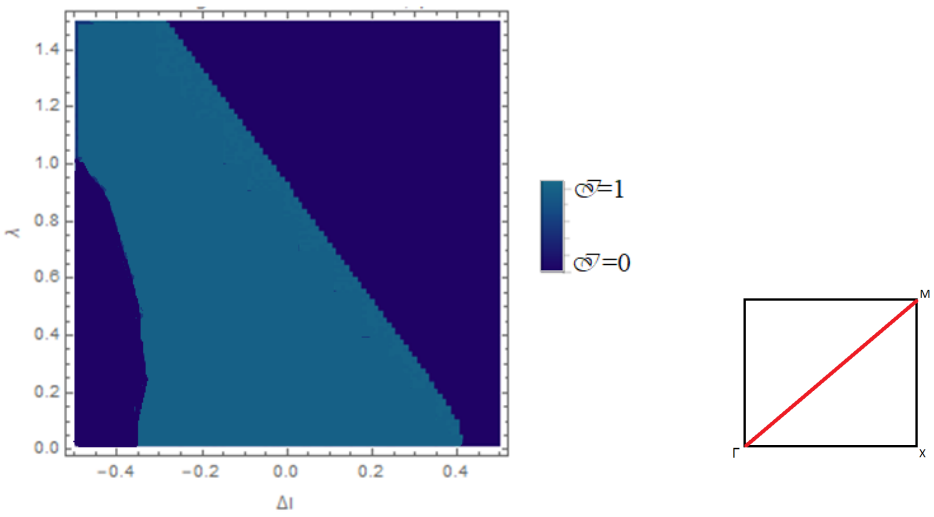

Figure 4.14: Phase diagram of band 4 and 5 along ΓM direction, as indicated by the red line in the figure on the right, for $\frac{\Delta_O}{t_o}$=0.5 and $\frac{t_p}{t_o}$=0.1. The blue zone corresponds to the value 0 of the invariant, while the light blue zone is relative to the value 1 of the invariant.

Γ X, band 4 and 5 have two subsequent intersections, that is the reason why the total number of inversion, namely $\mathscr{I}_{\Gamma X}$, is equal to 0. The pocket around the X point, which is appearing in this range of parameters, disappears when the value of $\frac{\Delta_I}{t_o}$ is increased. In the last panel on the right, $\frac{\Delta_I}{t_o}$=0.35 and there is only one pocket around the Γ point. This reproduces correctly the final values of the invariant 101, where the bands have no more intersections along XM direction. In summary, when moving across such kind of transition, a nodal line (first panel on the left of Fig. 4.17) separates in two distinct (central panels of Fig. 4.17) nodal lines by collapsing on the k_x axis. During that transition, the invariant $\mathscr{I}_{\Gamma X}$ is initially conserved, until one nodal line disappears and $\mathscr{I}_{\Gamma X} \rightarrow$1. The transition is defined as topological because it is characterized by a modification of the shape of the nodal line.

A similar transition can be obtained in the limit of strong SOC for the same

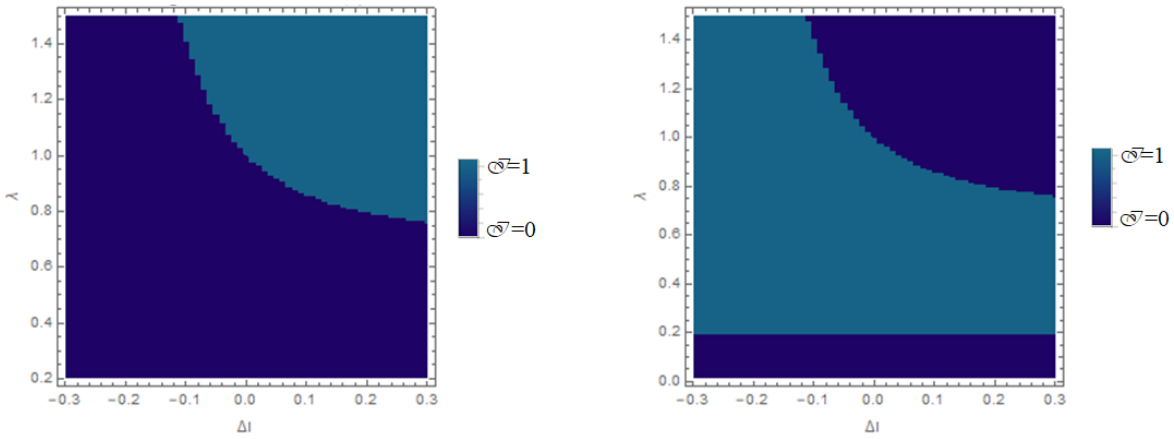

Figure 4.15: Phase diagrams of band 4 and 5 along the ΓX (left) and XM (right) direction for $\frac{\Delta_O}{t_o}$=-0.5 and $\frac{t_p}{t_o}$=0.1.The blue zone corresponds to the value 0 of the invariant, while the light blue zone is relative to the value 1 of the invariant.

pair of bands. We consider the phase diagrams of Fig. 4.12,4.13 and 4.14 and, by fixing the value of λ to $\frac{\lambda}{t_o}$=0.8, we find a modification of the shape of the nodal lines for 0.05≤ $\frac{\Delta_I}{t_0}$ ≤0.1 which is mapped as 011→110. In that transition, shown in Fig. 4.18, a starting pocket around the M point collapses along the ΓX direction and subsequently disappears by closing itself around the Γ point, while another pocket around the X point is formed.

However, the evolution of the nodal lines is not always the same: if we refer to the phase diagrams 4.15 and 4.16, for example, we can fix the value of $\frac{\Delta_I}{t_o}$=0.1 and draw a "vertical" line in the phase diagrams; by increasing λ, it is evident that the value of the invariant $\mathscr{I}_{\Gamma X}$ goes from 0 to 1, while $\mathscr{I}_{\Gamma M}$ goes from 1 to 0 on the ΓM phase diagram for 0.7≤ $\frac{\lambda}{t_o}$ ≤0.95 and the value of the invariant $\mathscr{I}_{XM}$ remains equal to 1. This corresponds to a transition of the kind 011 → 101. In this case, the evolution of nodal lines is obtained by increasing the value of λ and it is shown in Fig. 4.19. In the first panel on

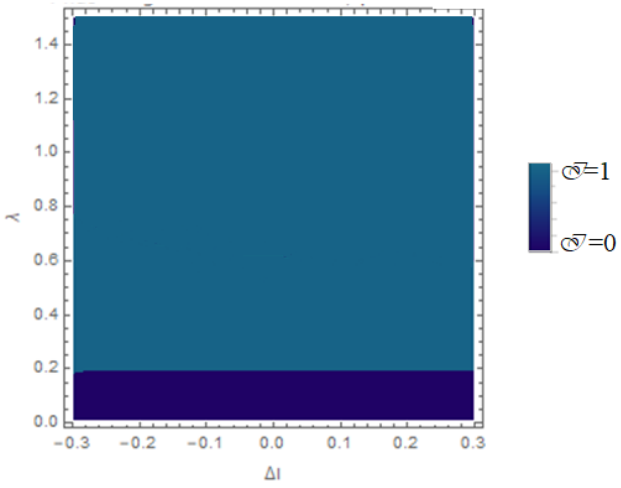

Figure 4.16: Phase diagram of band 4 and 5 along the ΓM direction for $\frac{\Delta_O}{t_o}$=-0.5 and $\frac{t_p}{t_o}$=0.1.The blue zone corresponds to the value 0 of the invariant, while the light blue zone is relative to the value 1 of the invariant.

the left, $\frac{\lambda}{t_o}$=0.7 and the nodal line is initially constituted by a pocket around the M point, recovering the invariant sequence 011. Increasing the value of λ, this pocket moves along the diagonal direction, changing its concavity. In the second panel, $\frac{\lambda}{t_o}$=0.8, in the third panel $\frac{\lambda}{t_o}$=0.86 and the topology of the nodal line has changed; in the last panel on the right, $\frac{\lambda}{t_o}$=0.95 and the pocket has formed around the Γ point. There is not a zero along the XM direction, while a zero along the ΓX direction appears, so that we find the final invariant mapping 101. In summary, in this second kind of transition the nodal line is not separated along a specific direction but it moves continuously in the BZ

.

In light of all the results which we have obtained, we individuate several distinctive evolutions of the nodal lines which we briefly describes in the following list:

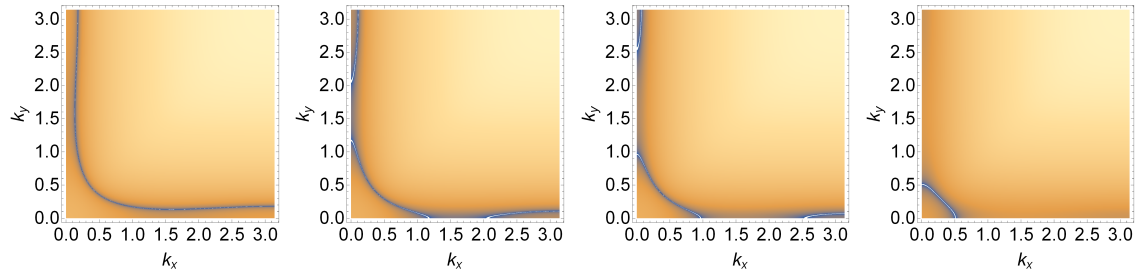

Figure 4.17: Topological transition in the momentum space relative to band 4 and 5 with $\frac{t_p}{t_o}$=0.1,$\frac{\Delta_O}{t_o}$=0.5 . The figure show a density plot of the logarithm of the difference between the energies of band 4 and 5 increasing the value of Δ_I for $\frac{\lambda}{t_o}$=0.2; in the first picture on the left, $\frac{\Delta_I}{t_o}$=0.34, in the second picture $\frac{\Delta_I}{t_o}$=0.343, in the third picture $\frac{\Delta_I}{t_o}$=0.344, in the last picture $\frac{\Delta_I}{t_o}$=0.35

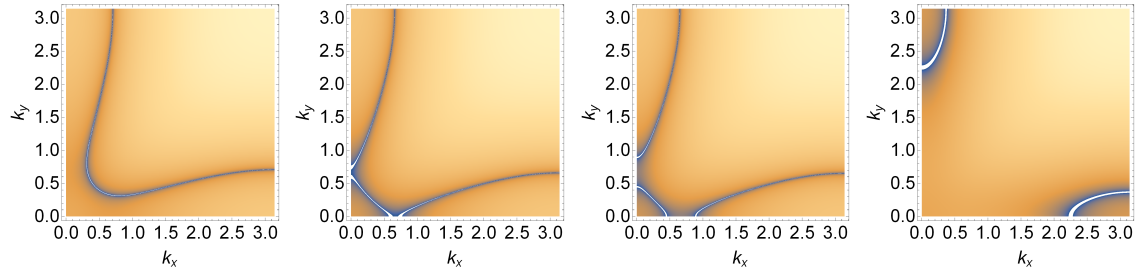

Figure 4.18: Topological transition in the momentum space relative to band 4 and 5 with $\frac{t_p}{t_o}$=0.1,$\frac{\Delta_O}{t_o}$=0.5 . The figure show a density plot of the logarithm of the difference between the energies of band 4 and 5 increasing the value of Δ_I for $\frac{\lambda}{t_o}$=0.8; in the first picture on the left, $\frac{\Delta_I}{t_o}$=0.05, in the second picture $\frac{\Delta_I}{t_o}$=0.0588, in the third picture $\frac{\Delta_I}{t_o}$=0.06, in the last picture $\frac{\Delta_I}{t_o}$=0.1

- type A: a nodal line is located around an high symmetry point (panel (a) of Fig. 4.20). By varying the value of one of the two parameters reported on the phase diagram, another pocket which is located around another high symmetry point emerges (panel (b) of Fig. 4.20) . Those pockets came closer until they merge (panel (c) of Fig. 4.20). During this evolution, the value of the $\mathscr{I}$ is zero due to a double band inversion along the direction of the BZ that connects those points. The resulting nodal line subsequently moves far from that direction and approaches

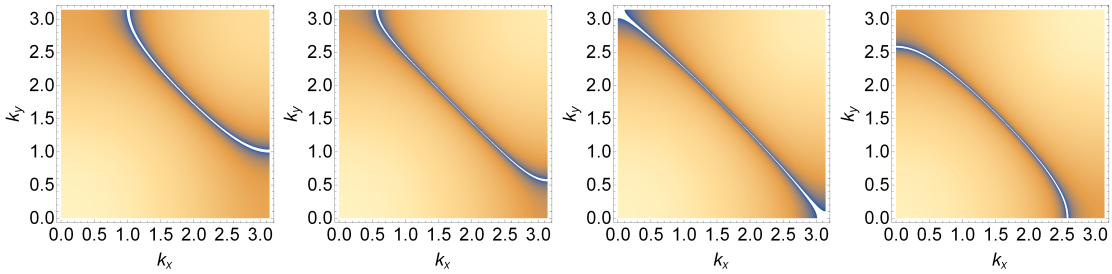

Figure 4.19: Topological transition in the momentum space relative to band 4 and 5 with $\frac{t_p}{t_o}$=0.1,$\frac{\Delta_O}{t_o}$=-0.5 . The figure show a density plot of the logarithm of the difference between the energies of band 4 and 5 increasing the value of λ for $\frac{\Delta_I}{t_o}$=0.1; in the first picture on the left, $\frac{\lambda}{t_o}$=0.7, in the second picture $\frac{\lambda}{t_o}$=0.8, in the third picture $\frac{\lambda}{t_o}$=0.86, in the last picture $\frac{\lambda}{t_o}$=0.95

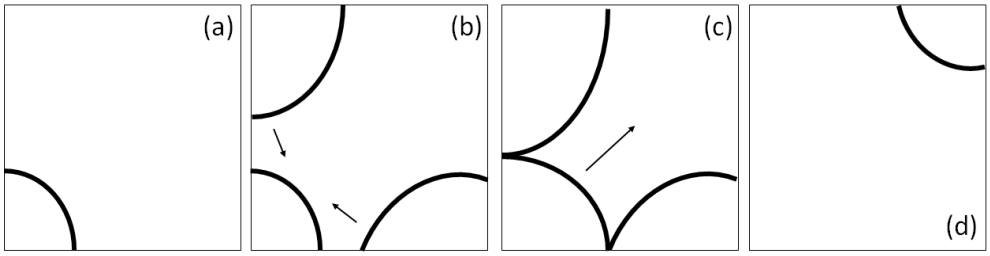

Figure 4.20: Schematic evolution of type A transition

the remaining point (panel (d) of Fig. 4.20).

- type B: we start from a pocket around an high symmetry point (panel (a) of Fig. 4.21). By varying the value of one of the two parameters the nodal line goes far from the original point and passes through the adjacent corners (panel (b) of Fig. 4.21); finally, it evolves around the point which is at the opposite site (panel (c) of Fig. 4.21).In doing that, it changes its concavity up to reverse it.

The transitions described above are respectively of type A and B. In our accurate exploration, we have found different transitions and analyzed them as a function of the driving microscopic parameters . Our results are

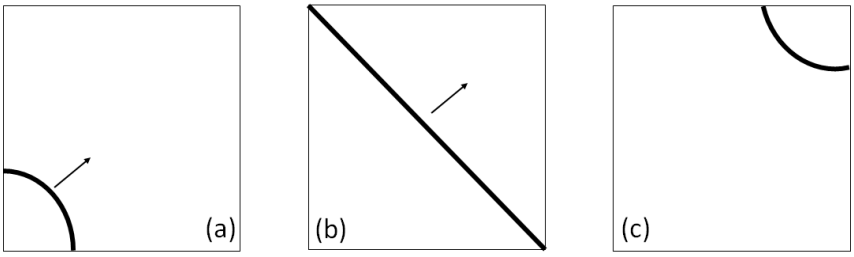

Figure 4.21: Schematic evolution of type B transition

summarized in Table 4.1.The first column of the table includes all pairs of bands which manifests the transition, then we specify the invariant value relative to the transition and the type of transition, according to the previous list; then, the following columns are occupied by the values of the parameters at which the transition occurs. The topological aspects of these transitions

Table 4.1: Topological transitions

Bands	Crossing	Type	$\frac{\Delta_O}{t_0}$	$\frac{\lambda}{t_0}$	$\frac{\Delta_I}{t_o}$
b3b4	011→101	type B	0.5	0.2	-0.48$\leq \frac{\Delta_I}{t_o} \leq$-0.2
b4b5	011→101	type A	0.5	0.2	0.34$\leq \frac{\Delta_I}{t_o} \leq$0.35
b4b5	011→110	type A	0.5	0.8	0.05$\leq \frac{\Delta_I}{t_o} \leq$0.1
b7b8	011→101	type A	0.5	0.65$\leq \frac{\lambda}{t_o} \leq$0.77	0.2
b4b5	011→101	type B	-0.5	0.7$\leq \frac{\lambda}{t_o} \leq$0.95	0.1
b5b6	011→101	type B	-0.5	0.1	-0.42$\leq \frac{\Delta_I}{t_0} \leq$-0.37
b6b7	011→101	type B	-0.5	0.2	0.2$\leq \frac{\Delta_I}{t_0} \leq$0.49
b7b8	110→101	type A	-0.5	0.95$\leq \frac{\lambda}{t_o} \leq$1	0

are intended to be referred to the nodal structure of the system, which evolves in the BZ by changing the values of the microscopic parameters. In the case in which other symmetries, such as the chiral symmetry, force the system to

be locked at the Fermi level, the topological transition of the nodal structure may be considered as Lifshitz one.

4.5 Summary and conclusions

We have analyzed emerging topological phases in a "disconnected" trilayered structure, which recall the Ruddlesden-Popper series. The associated Hamiltonian obeys time-reversal, inversion symmetries and also a layer interchange symmetry in the case of equivalent outer layers due to the characteristic structure of the trilayer. A preliminary analysis in the unit cell reveals that inner and outer CF in presence of SOC lift the orbital degeneracy in a non-trivial way. Introducing the in-plane hopping t_p, which is treated as a subdominant energy scale with respect to CF and SOC, one gets the energy band structure where crossing points between bands with opposite parity emerge. We have associated a local invariant $\mathscr{I}$ to each pair of crossing bands, which gives the total number of crossings between them in correspondence of fixed values of the microscopic parameters of the model. We have analyzed and characterized the evolution of emerging symmetry-protected nodal lines and have observed that a modification of the shape of the nodal lines occurs whenever $\mathscr{I}$ changes its value. Of course, the appearance of that transitions is strongly influenced by the interplay between CF, SOC and hopping parameters.

Chapter 5

Conclusions

The main purpose of this thesis is to analyze the effects of a substantial SOC in TMOs by following two different paths. In the first part of the thesis,we have focused the attention on the study of heavy TMOs with a strong SOC; in particular,we have analyzed the effects of SOC on the magnetic state of a d^1 TM ion with tetrahedral configuration, in which the occupancy of the lower e manifold is naturally favored. We have analyzed the effect of the interplay between SOC and CF splitting demonstrating that, while in the ideal undistorted tetrahedral symmetry SOC acts only as a perturbation on the lowest energy levels set by the CF splitting, its effect can be strongly enhanced in the case of a distorted geometry. We have considered a configuration where the tetrahedron is squashed along the z axis and proved that the interplay between SOC and CF parameters is responsible of a significant growth of the gap within the set of the lowest energy levels involved in the magnetic exchange and also of the manifestation of magnetic anisotropy.
We have considered the specific case of the $KOsO_4$ compound to investigate

the competition between strong electron correlations, SOC and tetrahedral deformations in the nominally e^1 configuration of the Os^{7+} ions. Ab-initio calculations show that $KOsO_4$ is characterized by a modest tetrahedral CF splitting within the e and t_2 orbitals which is comparable to the typical value of the SOC in $5d$ TM ions; in addition, due to the structural deformations, SOC has a relevant effect on the lowest e levels. We have addressed a specific Hubbard Hamiltonian and have performed an ED study on dimers which lie along different directions in the unit cell. We have demonstrated that SOC plays an active role in setting the boundary between AFM/ferro-orbital and anisotropic partially-FM correlations, which emerge to be bond-direction dependent. This proximity is driven by the interplay between substantial SOC, Hund's exchange and also by the hopping connectivity across e-t_2 orbitals. The peculiar and SOC-assisted magnetic superexchange brings the system towards a Kitaev-like physics, where the interplay between the SOC and the bonding geometry is a crucial element.

In the second part of the thesis, we have analyzed a disconnected trilayered structure composed by TM ion blocks stacked along the z direction, in which the in-plane itinerancy has been supposed to be highly damped and, then, the competition between the local energy scale is dominant.We have analyzed in detail the symmetries of the tight-binding Hamiltonian associated to the trilayer, which include the time-reversal and the layer- interchange ones, and we have demonstrated that, in presence of these specific symmetries, the SOC may have a role in determining the topology of the electronic structure. We have analyzed the evolution and eventually the closing of the energy gaps in a weakly dispersive electronic structure by using SOC as driv-

ing parameter in lifting the degeneracy of the spin/orbital entangled states. The result of this exploration has been the discovery of symmetry-protected nodal lines, which arise from the crossing between bands belonging to different layer-interchange symmetry sectors. In the limit of weak and strong SOC, we have identified several kinds of transitions between different topological configurations, which resemble Lifshitz-like behavior for nodal lines.

Appendix A

Spin Orbit Coupling

In this Appendix, we give an analytical derivation of SOC whose starting point is the relativistic Dirac equation. General remarks about the effect of SOC in solids are given in the subsequent section, including qualitative description of the Dresselhaus, Rashba effect, Dzyaloshinskii-Moriya interaction and magnetocrystalline anisotropy.

A.1 Analytical derivation of Spin Orbit Coupling

The analitical derivation of SOC follows from the study of the Dirac equation, which simbolizes the perfect union between the quantum mechanic theory and the special relativity theory [95].Let us start from the Hamiltonian function for a free particle, which is the non-relativistic equation for its energy:

$$H = \frac{\mathbf{p}^2}{2m} \tag{A.1}$$

The quantum expression of $\mathbf{p}$ and H are given by the operators

$$\mathbf{p} = -i\hbar \bigtriangledown \qquad H = i\hbar \frac{\partial}{\partial t} \tag{A.2}$$

Substituting these expressions in(A.1), we obtain the well-known non-relativistic Schrödinger equation:

$$i\hbar\dot{\psi} = -\frac{\hbar^2}{2m} \bigtriangledown^2 \psi \tag{A.3}$$

Eq. (A.3) written here is not relativistically invariant; therefore, we would transform it in a new equation which is consistent with relativistic theory. In the special relativity theory, a generic point is specified by four coordinates, one for time and the other three for the space, so we write it as (x_0, x_1, x_2, x_3), where $x_0 = ct$ stands for the time coordinate. In this context, distance is defined as:

$$s^2 = x_0^2 - x_1^2 - x_2^2 - x_3^2 \tag{A.4}$$

Transformations which leave (A.4) invariant are called Lorentz transformations; these type of transformations are peculiar also because they leave Maxwell's equations for the electromagnetic field unchanged in form under the assumption to consider the scalar potential $A_0 = \Phi$ and the vector potential $\bar{A} = (A_x, A_y, A_z)$ as the four coordinates of a four-vector , which is then given by (A_0, A_x, A_y, A_z).

Special relativity theory states that not only the electromagnetic equation but also the correct mechanical equations have to be invariant in form un-

der Lorentz transformations; in order to satisfy this statement, first of all we have to generalize the expression for the mechanical momentum (A.2), because it has only three components and, in addition, it involves the differentiation with respect to a coordinate t rather than with respect to a scalar. These two apparent difficulties can be overcome adding the time component p_0 being c^{-1} times the energy E of the system, so we have the four-vector $(\frac{E}{c}, p_x, p_y, p_z)$ whose relativistic expression is given by:

$$p_\mu = m_0 c \frac{dx_\mu}{ds} \qquad \mu = 0, 1, 2, 3 \tag{A.5}$$

where m_0 is the mass of the particle measured in a frame of reference in which it is at rest. The explicit expression of each component of this four-vector is:

$$p_0 = Ec^{-1} = c^{-1} i\hbar \frac{\partial}{\partial t} = i\hbar \frac{\partial}{\partial x_0} \tag{A.6}$$

$$p_1 = -i\hbar \frac{\partial}{\partial x_1} \tag{A.7}$$

$$p_2 = -i\hbar \frac{\partial}{\partial x_2} \tag{A.8}$$

$$p_3 = -i\hbar \frac{\partial}{\partial x_3} \tag{A.9}$$

The definition (A.5) is consistent with the original one (A.3) .
Now, we rewrite the Schrödinger equation (A.3) with the relativistic formalism that we have introduced in the last passages. It is natural assume that the energy of the particle is the Hamiltonian and, in order to obtain an equation for this, we have to consider the scalar connected with p_μ using (A.4)

and (A.5):

$$p_0^2 - p_1^2 - p_2^2 - p_3^2 = m_0^2 c^2 [(\frac{dx_0}{ds})^2 - (\frac{dx_1}{ds})^2 - (\frac{dx_2}{ds})^2 - (\frac{dx_3}{ds})^2] = m_0^2 c^2 \quad \text{(A.10)}$$

Allowing (A.10) to operate on a function Ψ according to (A.6),(A.7),(A.8) and (A.9), we obtain the relativistic equation for a free particle

$$(p_0^2 - p_1^2 - p_2^2 - p_3^2 - m_0^2 c^2)\Psi = 0 \quad \text{(A.11)}$$

which is called Klein Gordon equation and represents the first relativistic generalization of the Schrödinger equation [95].However, this equation presents several problems:first of all, it does not describe correctly the spectrum of the hydorgen atom; then, it is mathematically puzzling, because it is a second order differential equation in t, so we require the initial value of Ψ and $\dot{\Psi}$ to solve it, while the Schroedinger equation requires only the initial value of Ψ. In order to obtain a result which satisfies this last require, Dirac proposed to factorize (A.11) in two linear factors in this way:

$$\begin{aligned} &(p_0^2 - p_1^2 - p_2^2 - p_3^2 - m_0^2 c^2) = \\ &(p_0 - \alpha_1 p_1 - \alpha_2 p_2 - \alpha_3 p_3 - \beta m_0 c)(p_0 + \alpha_1 p_1 + \alpha_2 p_2 + \alpha_3 p_3 + \beta m_0 c) \end{aligned} \quad \text{(A.12)}$$

If the α_i and β coefficients commute with the p_μ and satisfy the following

relations:

$$\alpha_1^2 = \alpha_2^2 = \alpha_3^2 = \beta^2 = 1 \tag{A.13}$$

$$\{\alpha_i, \alpha_j\} = 0 \qquad i = 1, 2, 3 \tag{A.14}$$

$$\{\alpha_i, \beta\} = 0 \qquad i = 1, 2, 3 \tag{A.15}$$

then, any solution of the linear equation

$$(p_0 + \alpha_1 p_1 + \alpha_2 p_2 + \alpha_3 p_3 + \beta m_0 c)|\Psi\rangle = 0 \tag{A.16}$$

is a solution of (A.11).

It is evident from (A.13),(A.14) and (A.15) that the α_i and β coefficients cannot be numbers; they are matrices. The first reasonable choice of these matrices is constituted by the Pauli matrices σ_x,σ_y,σ_z and the identity matrix $\mathbb{1}$, because any 2×2 matrix can be expressed as a linear combination of them with complex coefficients.

$$\sigma_x = \begin{bmatrix} 0 & 1 \\ 1 & 0 \end{bmatrix} \qquad \sigma_y = \begin{bmatrix} 0 & -i \\ i & 0 \end{bmatrix} \qquad \sigma_z = \begin{bmatrix} 1 & 0 \\ 0 & -1 \end{bmatrix} \qquad \mathbb{1} = \begin{bmatrix} 1 & 0 \\ 0 & 1 \end{bmatrix} \tag{A.17}$$

These matrices satisfy (A.13) and (A.14) but, if we put $\beta = \mathbb{1}$, the relation (A.15) leads to have $\alpha_i = 0$, that is not possible. Then, one considers this

second set of quantities:

$$\alpha_1 = \rho_x \sigma_x \tag{A.18}$$

$$\alpha_2 = \rho_x \sigma_y \tag{A.19}$$

$$\alpha_3 = \rho_x \sigma_z \tag{A.20}$$

$$\beta = \rho_z \tag{A.21}$$

where ρ_x and ρ_z are given by:

$$\rho_x = \begin{bmatrix} 0 & 1 \\ 1 & 0 \end{bmatrix} \qquad \rho_z = \begin{bmatrix} 1 & 0 \\ 0 & -1 \end{bmatrix} \tag{A.22}$$

With this new set of matrices, the relations (A.13),(A.14) and (A.15) are satisfied and, with $\boldsymbol{\sigma} = (\sigma_x, \sigma_y, \sigma_z)$ and $\mathbf{p} = (p_1, p_2, p_3)$, Dirac equation (A.16) can be written as:

$$(p_0 + \rho_x \boldsymbol{\sigma} \cdot \mathbf{p} + \rho_z m_0 c)|\Psi\rangle = 0 \tag{A.23}$$

which is clearly:

$$(p_0 \begin{bmatrix} 1 & 0 \\ 0 & 1 \end{bmatrix} + \boldsymbol{\sigma} \cdot \mathbf{p} \begin{bmatrix} 0 & 1 \\ 1 & 0 \end{bmatrix} + m_0 c \begin{bmatrix} 1 & 0 \\ 0 & -1 \end{bmatrix})|\Psi\rangle = 0 \tag{A.24}$$

From (A.24), we deduce that $|\Psi\rangle$ has to be a vector:

$$|\Psi\rangle = \begin{bmatrix} \Psi_1 \\ \Psi_2 \end{bmatrix} \tag{A.25}$$

and then, following Eq. (A.24), we obtain these two simultaneous equations:

$$\begin{aligned}(p_0 + m_0c)\Psi_1 + \boldsymbol{\sigma} \cdot \mathbf{p}\Psi_2 = 0 \\ (p_0 - m_0c)\Psi_2 + \boldsymbol{\sigma} \cdot \mathbf{p}\Psi_1 = 0\end{aligned} \tag{A.26}$$

These equations can be improved by the fact that the electron has a charge $-e$ and may be in an electromagnetic field, whose potential is given by the four-vector (A_0, A_x, A_y, A_z). We introduce this information by replacing p_μ with $p_\mu + (\frac{e}{c})A_\mu$ in equations (A.26), which becomes [95]:

$$\begin{aligned}(p_0 + m_0c + \frac{e}{c}A_0)\Psi_1 + \boldsymbol{\sigma} \cdot (\mathbf{p} + \frac{e}{c}\mathbf{A})\Psi_2 = 0 \\ (p_0 - m_0c + \frac{e}{c}A_0)\Psi_2 + \boldsymbol{\sigma} \cdot (\mathbf{p} + \frac{e}{c}\mathbf{A})\Psi_1 = 0\end{aligned} \tag{A.27}$$

These equations represent Dirac equations written in a form which is most useful for our purpose.

Let's multiply each equations (A.27) by c and replace cp_0 with the eigenvalues W of the energy. We also take in consideration that

$$W = E + m_0c^2 \tag{A.28}$$

where E is the energy of the system omitting the rest mass. Equations (A.27) become:

$$\begin{aligned}(E + 2m_0c^2 + eA_0)\Psi_1 + c\boldsymbol{\sigma} \cdot (\mathbf{p} + \frac{e}{c}\mathbf{A})\Psi_2 = 0 \\ (E + eA_0)\Psi_2 + c\boldsymbol{\sigma} \cdot (\mathbf{p} + \frac{e}{c}\mathbf{A})\Psi_1 = 0\end{aligned} \tag{A.29}$$

Introducing the quantity [95]

$$f = \frac{2m_0c^2}{2m_0c^2 + E + eA_0} \tag{A.30}$$

we can derive from the first of Eq. (A.29) the expression of Ψ_1:

$$\Psi_1 = -\frac{f}{2m_0c}\boldsymbol{\sigma} \cdot (\mathbf{p} + \frac{e}{c}\mathbf{A})\Psi_2 \tag{A.31}$$

and, substituting (A.31) in the second of Eq. (A.29) , we obtain an equation for Ψ_2 and E:

$$(\frac{1}{2m_0}\boldsymbol{\sigma} \cdot (\mathbf{p} + \frac{e}{c}\mathbf{A})f\boldsymbol{\sigma} \cdot (\mathbf{p} + \frac{e}{c}\mathbf{A}) - eA_0 - E)\Psi_2 = 0 \tag{A.32}$$

Looking at Eq. (A.30), it is evident that f is a very small quantity, so we can expand it to the first order:

$$f = 1 - \frac{E + eA_0}{2m_0c^2}, \qquad \frac{\partial f}{\partial x_i} = -\frac{e}{2m_0c^2}\frac{\partial A_0}{\partial x_i} \tag{A.33}$$

where x_i is a spatial coordinate. If we stopped at the lowest order, taking only the first term $f = 1$ of (A.33), from (A.32) we would obtain a non-relativistic equation which is not interesting for our purpose. Then, we retain the first-order term arising from f, setting $\mathbf{A} = 0$ and considering A_0 as a function of r alone, therefore implementing the spherical symmetry of the electrostatic field. Under this hypothesis, Eq. (A.32) becomes:

$$\{\frac{1}{2m}(\boldsymbol{\sigma} \cdot \mathbf{p})f(\boldsymbol{\sigma} \cdot \mathbf{p}) - eA_0 - E\}\Psi_2 = 0 \tag{A.34}$$

Using the rule for differentiating a product ,we can transform the term

inside (A.34) in this way:

$$(\sigma \cdot \mathbf{p}) f (\boldsymbol{\sigma} \cdot \mathbf{p}) = (\boldsymbol{\sigma} \cdot \mathbf{p})^2 f - (\boldsymbol{\sigma} \cdot \mathbf{p}) \boldsymbol{\sigma} \cdot (\mathbf{p} f) = X_1 - X_2 \tag{A.35}$$

Now, we expand separately each term of this last equation,using the formula:

$$(\boldsymbol{\sigma} \cdot \mathbf{B})(\boldsymbol{\sigma} \cdot \mathbf{C}) = \mathbf{B} \cdot \mathbf{C} + i \boldsymbol{\sigma} \cdot \mathbf{B} \wedge \mathbf{C} \tag{A.36}$$

where $\mathbf{B}$ and $\mathbf{C}$ are any vectors which commute with $\boldsymbol{\sigma}$. If $\mathbf{B} = \mathbf{C}$, then (A.36) is modified into:

$$(\boldsymbol{\sigma} \cdot \mathbf{B})(\boldsymbol{\sigma} \cdot \mathbf{B}) = (\boldsymbol{\sigma} \cdot \mathbf{B})^2 = B^2 + i \boldsymbol{\sigma} \cdot \mathbf{B} \wedge \mathbf{B} \tag{A.37}$$

Taking X_1 form (A.35), using (A.37) with $\mathbf{B} = \mathbf{p}$ and substituting the expression of f from (A.33), we have:

$$X_1 = (\boldsymbol{\sigma} \cdot \mathbf{p})^2 f = p^2 f = p^2 (1 - \frac{E + eA_0}{2m_0 c^2}) \tag{A.38}$$

We are searching for a Ψ_2 which satisfies (A.32); this means that, at zero order,namely when $f = 1$, and under our hypothesis for which $\mathbf{A} = 0$, Ψ_2 satisfies:

$$(\frac{1}{2m} \mathbf{p}^2 - eA_0 - E) \Psi_2 = 0 \tag{A.39}$$

From (A.39), we have

$$\frac{1}{2m} \mathbf{p}^2 = eA_0 + E \tag{A.40}$$

and finally, substituting this expression in (A.38), we obtain:

$$X_1 = \mathbf{p}^2(1 - \frac{\mathbf{p}^2}{4m_0^2c^2}) = \mathbf{p}^2 - \frac{\mathbf{p}^4}{4m_0^2c^2} \tag{A.41}$$

Now, we use (A.36) in order to expand the expression of X_2; taking $\mathbf{B} = \mathbf{p}$ and $\mathbf{C} = \mathbf{p}f$, we have:

$$X_2 = (\boldsymbol{\sigma} \cdot \mathbf{p})\boldsymbol{\sigma} \cdot (\mathbf{p}f) = \mathbf{p} \cdot (\mathbf{p}f) + i\boldsymbol{\sigma} \cdot \mathbf{p} \wedge (\mathbf{p}f) \tag{A.42}$$

Substituting in (A.42) the explicit expression (A.2) of $\mathbf{p}$:

$$\begin{aligned} X_2 &= (-i\hbar)^2\nabla \cdot (\nabla f) + i(-i\hbar)^2\sigma \cdot \nabla \wedge (\nabla f) \\ &= -\hbar^2\nabla^2 f - \hbar^2(\nabla f) \cdot \nabla + i(-i\hbar)^2\sigma \cdot [-(\nabla f) \wedge \nabla + \nabla \wedge (\nabla f)] \\ &= -\hbar^2(\nabla f) \cdot \nabla - \hbar\sigma \cdot (\nabla f) \wedge \mathbf{p} \end{aligned} \tag{A.43}$$

where in the last equality we have considered that A_0 satisfies Laplace's equation, then $\nabla^2 A_0 = 0$, and that the curl of the gradient of f is equal to zero. Recalling (A.33) and the fact that A_0 is a function of r alone, we can easily calculate

$$\nabla f = \frac{\mathbf{r}}{r}\frac{df}{dr} \tag{A.44}$$

With this element, X_2 is finally equal to:

$$\begin{aligned} X_2 &= -\frac{\hbar^2}{r}\frac{df}{dr}\mathbf{r} \cdot \nabla - \frac{\hbar}{r}\frac{df}{dr}\boldsymbol{\sigma} \cdot \mathbf{r} \wedge \mathbf{p} \\ &= -\hbar^2\frac{df}{dr}\frac{\partial}{\partial r} - \frac{\hbar}{r}\frac{df}{dr}\boldsymbol{\sigma} \cdot \mathbf{l} \end{aligned} \tag{A.45}$$

In addition, we know that $\frac{df}{dr} = -\frac{e}{2m_0c^2}\frac{dA_0}{dr}$. Collecting all the results and substituting them in Eq. (A.34), we finally have:

$$\{\frac{1}{2m}\mathbf{p}^2-\frac{1}{8m_0^3c^2}\mathbf{p}^4-eA_0-\frac{e\hbar}{4m_0^2c^2r}\frac{dA_0}{dr}\boldsymbol{\sigma}\cdot\mathbf{l}-\frac{e\hbar^2}{4m_0^2c^2}\frac{dA_0}{dr}\frac{\partial}{\partial r}\}\Psi_2 = E\Psi_2 \quad \text{(A.46)}$$

This is the Schödinger equation written with relativistic corrections; in particular, the fourth term of the term on the left of Eq. (A.46) is the spin-orbit coupling energy. Considering that $\mathbf{s} = \frac{\hbar}{2}\sigma$ and solving the equation for a Coulomb field, namely $A_0 = \frac{Ze}{r}$, we have that this contribution to the Hamiltonian is:

$$h_{SOC} = \frac{Ze^2}{2m_0^2c^2r^3}\mathbf{l}\cdot\mathbf{s} \quad \text{(A.47)}$$

A.2 Spin Obit Coupling in solids

A.2.1 Non-magnetic solids

When an electron moves in a solid, the situation is deeply different respect to the atomic case; in a solid, the valence electrons arrange to optimize the chemical bonding and the splitting of the energetic levels is determined by the crystal field. As a consequence, at the Γ- point, where the crystal momentum is zero, the effect of SOC is quite similar to the atomic case, but away from the Γ- point new effects arise, which strongly depend on the symmetry of the crystal.

In a system without internal or external magnetic field, time reversal symmetry holds, which means that the properties of the system do not change inverting the direction of time. When the transformation t→ -t is implemented, a particle moving with momentum $\mathbf{k}$ is exchanged with a particle

moving with momentum -**k** ; in addition, time reversal also inverts the spin of electrons. All these considerations can be summed up in the following relation between energies of a right-moving spin up particle and a left-moving spin down one:

$$\varepsilon(\mathbf{k},\uparrow) = \varepsilon(-\mathbf{k},\downarrow) \tag{A.48}$$

In a crystal with inversion symmetry, the following relation additionally holds, both for spin up and spin down electrons:

$$\varepsilon(\mathbf{k}) = \varepsilon(-\mathbf{k}) \tag{A.49}$$

This means that band structure is symmetric around the center of Brioullin zone **k**=0, that in this point all bands are degenerate and that they are doubly degenerate in their evolution. In a crystal without inversion symmetry, obviously:

$$\varepsilon(\mathbf{k},\uparrow) \neq \varepsilon(\mathbf{k},\downarrow) \tag{A.50}$$

The degeneracy of the bands can be lifted as a consequence of SOC ; in these systems, a lack of inversion symmetry, which implies V(**r**) $\neq$ V(-**r**),will result in a non-vanishing potential gradient or electric field **E**(**r**). Dresselhaus was the first to emphasize [96] that SOC may have important consequences for one electron energy levels in bulk semiconductors ; he observed that in a zinc blende structure, occurring in semiconductors like GaAs (Fig. A.1, on the left), we can have a spin splitting of electron and hole states at nonzero

wave vectors **k** even if **B**=0; this is called Dresselhaus effect. For the lowest conduction band, the corresponding Dresselhaus Hamiltonian is given by [97]:

$$H_D = \alpha_D[\sigma_x p_x(p_y^2 - p_z^2) + \sigma_y p_y(p_z^2 - p_x^2) + \sigma_z(p_x^2 - p_y^2)] \tag{A.51}$$

where σ_x,σ_y and σ_z are the Pauli matrices and p_x,p_y and p_z are the momentum components in the crystallographic directions [100], [010] and [001] respectively. The Dresselhaus constant α_D is small if lighter elements are present in the semiconductor (for GaAs, it is 27.6 eV/$\mathring{A}^3$) while it is larger for heavier elements (it is 760.1 eV/$\mathring{A}^3$ for InSb) [98]. Hamiltonian (A.51) produces a spin splitting which is proportional to k^3. This corrections is not always in third-order in k: in crystal with wurzite structure such as ZnO (Fig. A.1, on the right), for example, the splitting due to (A.51) is linear in k. This result was achieved by Rashba in 1959 [99, 100].

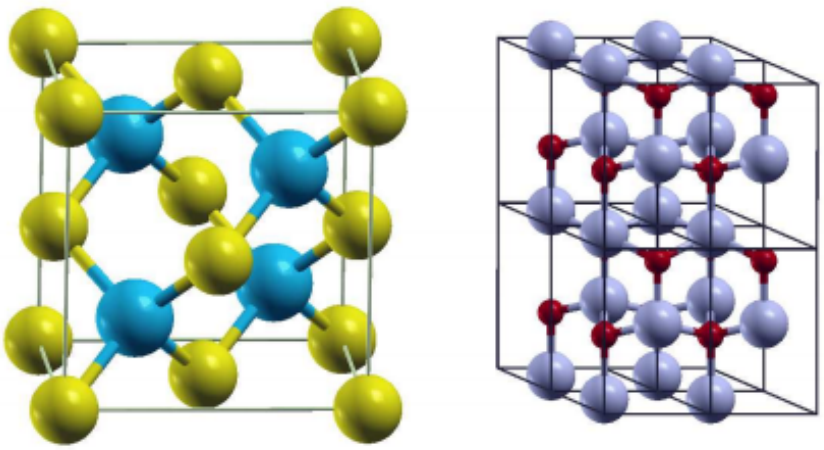

Figure A.1: Crystal structure of GaAs (zinc blende, left) and ZnO (wurzite, right).

In Fig. A.1, crystal zinc blende structure of GaAs and wurzite structure of ZnO are shown: both structures have no cener of inversion and this leads to spin orbit splitting for each of them, which is third-order in k for the former (Dresselhaus effect), and first order for the latter (Rashba effect). Termination of the crystal by a surface breaks the 3D inversion symmetry. Performing a Taylor expansion of the potential V($\mathbf{r}$), in lowest order its inversion asymmetry is characterized by an electric field $\mathbf{E}(\mathbf{r})$; when electrons with an effective mass m* move with velocity $\mathbf{v} = \frac{d\varepsilon}{d\mathbf{p}} = \frac{1}{m^*}\mathbf{k}$ in an external electric field $\mathbf{E}$ defined in a global frame of reference, then the relativistic Lorentz transformation give rise to magnetic field $\mathbf{B}=\frac{1}{c}(\mathbf{v}\wedge\mathbf{E})=(\frac{1}{m^*c}(\mathbf{k}\wedge\mathbf{E})$ in local frame of the moving electron. The interaction of the spin with this magnetic field leads to the Rashba Hamiltonian [98, 101, 102]:

$$H_R = \alpha_R \boldsymbol{\sigma} \cdot (\mathbf{p} \wedge \mathbf{E}) \tag{A.52}$$

The splitting is a combined effect of atomic spin-orbit coupling and asymmetry of the potential in the direction perpendicular to the two-dimensional plane. Remarkably, this effect can drive a wide variety of novel physical phenomena even when it is a small correction to the band structure of the two-dimensional metallic state.

A.2.2 Magnetic solids

The case of a bulk or a surface of magnetic metal is different; in this context, the exchange interaction is the dominant energetic scale and all spins align accordingly. However, if the exchange coupling is weak and SOC is strong,

non-trivial effects can arise. Dzyaloshinskii-Moriya (DM) interaction is one of them; its name derives from the fact that in 1960 Dzyaloshinskii constructed a model to describe weak ferromagnetism [103] and he introduced an asymmetrical term that brings also the name of Moriya because he found that the mechanism behind the interaction is partly based on SOC [104]. DM interaction is due to a lack of inversion symmetry of the compound and a strong SOC; without going into detail, we can consider the example of MnSi (manganese silicide), which is a compound in which inversion symmetry is broken into the unit cell. In addition, the compound has a strong SOC. Here, inversion symmetry can be broken in different directions, leading to different DM interaction: this means that the magnetization of the compound will be different in each case. Focusing the attention on only two spins, DM interaction assumes the following form:

$$H_{DM} = -\mathbf{D}_{12} \cdot (\mathbf{S}_1 \wedge \mathbf{S}_2) \tag{A.53}$$

where $\mathbf{S}_1$ and $\mathbf{S}_2$ are the atomic spins. The resulting DM interaction emerging from the interplay between two atomic spin with neighboring atoms having a large SOC in a thin film and pointing outwards from the plane of the atoms is shown in Fig. A.2.

It is evident that resulting magnetic structure depends on the direction of the $\mathbf{D}$ vector, which in turn depends on the way in which the symmetry in the compound is broken. Furthermore, an interaction of the type (A.53) will favor spin-spiral structure, which can be found on surfaces [105], or in domain walls [106] of thin magnetic films: DM interaction gives these spiral-

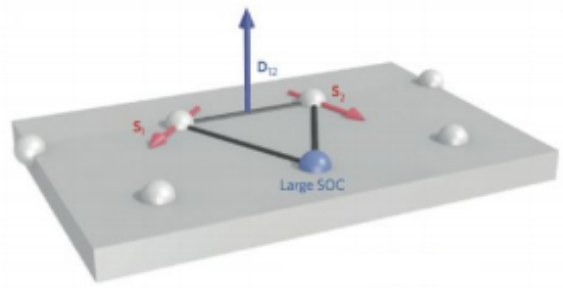

Figure A.2: Schematic representation of the DM interaction of two spins

ing magnetic structures a unique sense of rotation.

Another relevant effect which can arise in magnetic solids is the so-called magnetic anisotropy, that is the directional dependence of a material's magnetic properties.In particular, one kind of magnetic anisotropy is the magnetocrystalline anisotropy, which derives from the fact that the atomic structure of a crystal introduces preferential directions for the magnetization, which are usually related to the principal axes of its crystal lattice; this principally characterizes a ferromagnetic material when it takes more energy to magnetize in a direction rather than in another. SOC is the principal responsible of that, since it is basically the orbital motion of the electrons which couples with crystal field to determine the first order contribution to magnetocrystalline anisotropy [107]. One observable effect of magnetocrystalline anysotropy is the magnetostriction, which takes place when a ferromagnetic material change its shape or dimensions under the application of a magnetic field.

Appendix B

Löwdin tecnique

Lowdin tecnique is generally employed to map a starting eigenvalue problem in another one of lower dimensionality. This method, that we propose in the present appendix, was shown by P. Löwdin [108], who discussed the solution of an eigenvalue problem considering the case in which a set of approximated eigenfunctions is given; the connotative idea of the method is that, dividing this set into two classes, it is possible to obtain a formula in which the solution of the initial problem is expressed in terms of only one class of eigenfunctions, considering the other one as a perturbation.
The classical eigenvalues problem can be expressed as:

$$H\Psi = \epsilon\Psi \tag{B.1}$$

In the classical perturbation theory, the Hamiltonian H is generally equal to H_0+V, where V is a potential that can be expressed as a power series in a perturbation parameter. Using the Löwdin method, on the other hand,

it is not necessary that the Hamiltonian has such a specific form, the only assumption under which it is possible to use the procedure is that a set of orthonormalized functions $\Psi_n^{(0)}$ (with n=1,2...,N), which are approximate eigenfunctions of H, is known. It follows that the best eigenfunctions of H can be written as a linear combinations of them:

$$\Psi = \sum_{n=1}^{N} \Psi_n^{(0)} c_n \tag{B.2}$$

The element of the Hamiltonian H in the chosen basis are:

$$H_{mn} = \int \Psi_n^{*(0)} H \Psi_n^{(0)} d\tau \tag{B.3}$$

Then, coefficients c_n in Eq. (B.2) can be expressed using the variational principle, which states that the integral

$$E = \frac{\int \Psi^* H \Psi d\tau}{\int \Psi^* \Psi d\tau} \tag{B.4}$$

that can be also expressed in a discrete form, substituting Eq. (B.2) in it and using Eq. (B.3):

$$E = \frac{\sum_{mn} c_m^* H_{mn} c_n}{\sum_{mn} c_m^* \delta_{mn} c_n} \tag{B.5}$$

gives an approximate value of ϵ in Eq. (B.1) and that the best approximation is the one in correspondence of which δE=0. Assuming that, in the current case, E is a ratio of two quantities E=$\frac{W}{V}$, where W=$\sum_{mn} c_m^* H_{mn} c_n$

and V=$\sum_{mn} c_m^* \delta_{mn} c_n$ as established in Eq. (B.5), then:

$$\delta E = \frac{\delta W - E\delta V}{V} \tag{B.6}$$

Substituting in Eq. (B.6) the explicit expression of W and V, we obtain a system of linear equations for the coefficients c_n, which is:

$$\sum_{n=1}^{N} (H_{mn} - E\delta_{mn}) c_n = 0, \qquad m = 1, 2, .., N \tag{B.7}$$

Let us now turn on the crucial point of the Löwdin method: we divide the eigenfunctions $\Psi_n^{(0)}$ into two classes, indicated by (A) and (B). We are interested in the class (A) and want to treat the class (B) as a perturbation: in this way, we reduce the dimensionality of the problem (B.1), making it easier to solve. Under this assumption, the system (B.7) can be written as:

$$(E - H_{mn}) c_m = \sum_{n}^{A} H'_{mn} c_n + \sum_{n}^{B} H'_{mn} c_n \tag{B.8}$$

where

$$H'_{mn} = H_{mn}(1 - \delta_{mn}) \tag{B.9}$$

Eq. (B.8) is also equal to:

$$c_m = \sum_{n}^{A} h'_{mn} c_n + \sum_{n}^{B} h'_{mn} c_n \tag{B.10}$$

where the term h_{mn} is given by:

$$h_{mn} = \frac{H_{mn}}{(E - H_{mn})} \tag{B.11}$$

The next step of the method provides for using the formula (B.10) to rewrite c coefficients in the sum over (B), substituting (B.10) in itself, starting thus a process of iteration, which reproduces the Neumann series expansion. In this way, we formally eliminate the states in the class (B); the result of this process, in accordance with the notation of the original paper [108], is:

$$c_m = \sum_n^A (h'_{mn} + \sum_\alpha^B h'_{m\alpha} h'_{\alpha n} + \sum_{\alpha\beta}^B h'_{m\alpha} h - \alpha\beta' h'_{\beta n} + ...) c_n \tag{B.12}$$

Defining the following quantity:

$$U^A_{mn} = H_{mn} + \sum_\alpha^B \frac{H'_{m\alpha} H'_{\alpha n}}{E - H_{\alpha\alpha}} + \sum_{\alpha\beta}^B \frac{H'_{m\alpha} H'_{\alpha\beta} H'_{\beta n}}{(E - H_{\alpha\alpha})(E - H_{\beta\beta})} \tag{B.13}$$

and recalling also the relation (B.9), we obtain that Eq. (B.10) can be definitively written as:

$$c_m = \sum_n^A \frac{U^A_{mn} - H_{mn}\delta_{mn}}{E - H_{mm}} c_n \tag{B.14}$$

Eq. (B.14) shows that any coefficients appearing in the starting expression (B.2) can be expressed as a finite linear combination of coefficients c_n which belongs to the subspace (A). As a final result, we have that when $m \in (A)$ Eq. (B.7) becomes equal to:

$$\sum_n^A (U^A_{mn} - E\delta_{mn}) c_n = 0 \tag{B.15}$$

while when $m \in (B)$ it is equal to:

$$c_m = \sum_n^A \frac{U^A_{mn}}{E - H_{mm}} c_n \tag{B.16}$$

Looking at these last equations, it is evident that Eq. (B.15) is identical to Eq. (B.7) in form, differing from that for the fact that it is limited only to the subspace (A): using the Löwdin method, we have reduced an eigenvalue problem belonging initially to two classes (A) and (B) only to the class (A), replacing the matrix elements H_{mn} by the elements U^A_{mn}; the influence of the class (B) is taken into account by expansion of U^A_{mn} explicitly written in (B.13).

The initial problem is then dimensionally reduced, since it has been restricted only to the (A) subspace. However, the fact that the matrix U depends on its eigenvalues E is a non-trivial problem in resolving Eq. (B.15). The obstacle can be overcome linearizing the U^A_{mn} terms in (B.15), namely inserting in (B.13) the Taylor expansion of E about $E^{(0}_n$. The effective Hamiltonian is then written as [109]:

$$U^A_{mn} = H^{AA}_{mn} + \sum_\alpha^B \frac{H^{AB}_{m\alpha} H^{BA}_{\alpha n}}{E - H^{BB}_{\alpha\alpha}} = H^{AA}_{mn} + H^{AA(1)}_{mn} \tag{B.17}$$

With this last passage, the simplification of the initial problem is then evident.

Appendix C

Normal modes of a tetrahedron

C.1 Vibrations in one dimension

A normal mode of a system is an oscillation in which all parts of the system move sinusoidally with the same frequency and a fixed phase relation. The simplest case to study the normal modes is the one dimensional one, where there is only one degree of freedom. In order to implement vibrations of a one-dimensional system, this one has to be perturbed, namely it has to been moved from its stable equilibrium position. The latter corresponds to a position of the system in which the potential energy V(q), where q is a generalized coordinate, assumes a minimum value. Calling $\tilde{q}$ the equilibrium value of the generalized coordinate, for small deviations from the equilibrium position it is sufficient to consider only the first non- vanishing terms in the expansion of the difference V(q)-V($\tilde{q}$) in powers of $q-\tilde{q}$. The expansion gives back:

$$V(q) - V(\tilde{q}) \simeq \frac{1}{2}k(q-\tilde{q})^2 \tag{C.1}$$

Putting V($\tilde{q}$)=0 and using the new variable x, defined as the deviation of q from its equilibrium position value:

$$q - \tilde{q} = x \tag{C.2}$$

we have:

$$V(x) = \frac{1}{2}kx^2 \tag{C.3}$$

where k= U$''$($\tilde{q}$).

The kinetic energy of a system with one degree of freedom,in the same approximation used for the potential energy, has the form:

$$T = \frac{1}{2}a(q)\dot{q}^2 = \frac{1}{2}a(q)\dot{x}^2 \tag{C.4}$$

here a(q)=a($\tilde{q}$) and we can for brevity indicate it with m. Then:

$$T = \frac{1}{2}m\dot{x}^2 \tag{C.5}$$

The Lagrangian of the system is given by:

$$\mathscr{L} = T - V = \frac{1}{2}m\dot{x}^2 - \frac{1}{2}kx^2 \tag{C.6}$$

From Eq. (C.6), it is immediate to extract the equation of motion by the Euler- Lagrange equation:

$$\frac{d}{dt}\frac{\partial \mathscr{L}}{\partial \dot{x}} - \frac{\partial \mathscr{L}}{\partial x} = 0 \tag{C.7}$$

That is:

$$\ddot{x} + \omega^2 x = 0 \tag{C.8}$$

with $\omega = \sqrt{\frac{k}{m}}$. Eq. (C.8) is a well-known linear differential equation which describes an harmonic motion. The general solution is given by a linear superposition of its two independent solutions:

$$x(t) = c_1 \cos \omega t + c_2 \sin \omega t \tag{C.9}$$

which can be also written as:

$$x(t) = A \cos(\omega t + \Phi) \tag{C.10}$$

where A is the amplitude of oscillations and is equal to A=$\sqrt{c_1^2 + c_2^2}$, Φ is the phase of oscillations with $\tan \Phi = -\frac{c_2}{c_1}$ and ω is called angular frequency of oscillation.

A more general form of the solution (C.10) is given by considering it as a real part of a complex expression:

$$x(t) = Re[Be^{i\omega t}] \tag{C.11}$$

Putting B=Ae$^{i\Phi}$, and using Euler's formula, the expression (C.10) and (C.11) are equivalent, but the advantage of using the last one is that exponential factors are mathematically simpler than trigonometrical ones, since they are unchanged in form by diffferentiation.

All these passages show us that the system executes harmonic oscillations near a position of stable equilibrium with frequency ω.

C.2 Vibrations of molecules

The arguments reported in the previous section can be easily extended to a molecular environment, in which there are N nuclei and, then, we have 3N degrees of freedom, which is the number of coordinates we need in order to describe their motion. However, if one is interested in describing the vibrational motion of the system, it is convenient to remove the translational and rotational degrees of freedom. The former can be eliminated by equating to zero the total momentum of the molecule; as a result, the coordinates of the center of mass of the system remain constant during the oscillation. The latter can be removed by equating to zero the angular momentum of the system. Since the translation and the rotation of a system are respectively described by three coordinates, after this operation the system has 3N-6 degrees of freedom. If the system is linear, only two coordinates are required to describe rotations, then there are 3N-5 degrees of freedom at all.
The analytical method required to obtain the normal modes of a molecule is analogous of the one stated in one dimension. We assume to have a set of generalized coordinates:

$$(q_1, q_2, q_3, \ldots, q_n)$$

where n is the number of degrees of freedom of the system. The kinetic energy is a quadratic function of the velocities, while the potential energy is assumed to be a function of the generalized coordinates alone:

$$V = V(q_1, q_2, q_3, \ldots, q_n) \tag{C.12}$$

The potential energy (C.12) has a minimum for $q = \tilde{q}$, in correspondence of which the system assume a static position that is the equilibrium configuration; this set of coordinates $(\tilde{q}_1, \ldots, \tilde{q}_n)$ satisfies the n non linear equations

$$\frac{\partial V}{\partial q_\sigma}\Big|_{q=\bar{q}} = 0 \tag{C.13}$$

Once one has found the equilibrium position, he expands around it, introducing a new set of coordinates $(x_1, \ldots, x_\sigma)$ in this way:

$$q_\sigma = \tilde{q}_\sigma + x_\sigma \tag{C.14}$$

As it is evident from Eq. (C.14), x_σ are the displacements relative to equilibrium. Expanding the potential energy V as a function of x_σ, we obtain a positive definite quadratic form:

$$V = \frac{1}{2}\sum_{\sigma\sigma'} V_{\sigma\sigma'} x_\sigma x_{\sigma'} \tag{C.15}$$

Here, as in the one dimensional case, $V(\tilde{q})=0$. In addition, $V_{\sigma\sigma'} = V_{\sigma'\sigma}$, since they multiply the same quantities in the sum [110] and are equal to:

$$V_{\sigma\sigma'} = \frac{\partial^2 V}{\partial q_\sigma \partial q_{\sigma'}}\Big|_{q=\bar{q}} \tag{C.16}$$

The kinetic energy written in terms of the new coordinates is:

$$T = \sum_{\sigma,\sigma'=1}^{n} \frac{1}{2} T_{\sigma\sigma'}(x_1, \ldots, q_n)\dot{x_\sigma}\dot{x_{\sigma'}} \tag{C.17}$$

Coefficients $T_{\sigma\sigma'}$ are defined as:

$$T_{\sigma\sigma'} = \frac{\partial^2 T}{\partial \dot{q}_\sigma \partial \dot{q}_{\sigma'}}\Big|_{q=\bar{q}} \tag{C.18}$$

As it is evident that from (C.18), these coefficients are regarded to be symmetric. The Lagrangian of the system is then:

$$\mathscr{L} = \sum_{\sigma,\sigma'=1}^{n} \frac{1}{2} T_{\sigma\sigma'}(x_1, \ldots, x_n)\dot{x_\sigma}\dot{x_{\sigma'}} - \frac{1}{2} V_{\sigma\sigma'} x_\sigma x_{\sigma'} \tag{C.19}$$

Using the Euler- Lagrange equations:

$$\frac{d}{dt}\frac{\partial L}{\partial \dot{x}_i} - \frac{\partial L}{\partial x_i} = 0 \tag{C.20}$$

the equation of motion of the system are:

$$\sum_{\sigma'} T_{\sigma\sigma'}\ddot{x}_{\sigma'} + \sum_{\sigma'} V_{\sigma\sigma'} x_{\sigma'} = 0 \tag{C.21}$$

where $\sigma = 1, \ldots, n$. We search for function $x(t)$ with the form expressed in (C.11), that in this case is:

$$x_{\sigma'}(t) = C_{\sigma'} e^{-i\omega t} \tag{C.22}$$

Substituting Eq. (C.22) in Eq. (C.21), we obtain a set of linear homogeneous algebraic equations which have to be satisfied by $C_{\sigma'}$:

$$\sum_{\sigma} (-\omega^2 T_{\sigma\sigma'} + V_{\sigma\sigma'}) C_{\sigma'} = 0 \tag{C.23}$$

Non trivial solutions of the system can be achieved with the passage

$$det(-\omega^2 T_{\sigma\sigma'} + V_{\sigma\sigma'}) = 0 \tag{C.24}$$

Since T and V are of rank n, the above determinant yields an n^{th} order polynomial in ω^2 , whose n roots are the squared eigenvalues $(\omega_1, \ldots, \omega_n)$, namely the frequencies of the system. Once these frequencies are known, substituting their value in (C.23) also the corresponding coefficients $C_{\sigma'}$ are found. If all the frequencies ω_α are different, the coefficients $C_{\sigma'}$ are proportional to the minors of the determinant (C.24), with $\omega = \omega_\alpha$ [110]. If we denote by $\Delta_{\sigma'\alpha}$ the minors, the general solution of (C.21) is the real part of a superposition of all the particular solutions of the form $x_{\sigma'} = \Delta_{\sigma'\alpha}\ C_\alpha\ e^{-i\omega_\alpha t}$:

$$x_{\sigma'} = Re[\sum_{\alpha=1}^{n} \Delta_{\sigma'\alpha} C_\alpha e^{-i\omega_\alpha t}] = \sum_{\alpha} \Delta_{\sigma'\alpha}\theta_\alpha \tag{C.25}$$

Where

$$\theta_\alpha = Re[C_\alpha e^{-i\omega_\alpha t}] \tag{C.26}$$

The general solution of Eq. (C.21) is then a superposition of n simple periodic oscillations with definite frequencies ω_α. At this point, it is evident that one can choose a set of generalized coordinate in a way in which each of them execute only one simple oscillation. We can express $\theta_1 \ldots \theta_n$ in terms of the coordinates $x_1 \ldots x_n$; in this way,the coordinate θ_α are defined to satisfy the equations:

$$\ddot{\theta}_\alpha + \omega_\alpha^2 \theta_\alpha = 0 \qquad \alpha = 1, \ldots, n \tag{C.27}$$

Using these coordinates, which are called normal coordinates, the equations of motion are given by a set of n independent equations, which are equation of simple harmonic oscillators. Corresponding eigenvectors are immediately calculated with the standard procedure.

The vibration energy must be invariant with respect to symmetry transformation of the system [111]; this means that, under any transformation belonging to the point symmetry group of the molecule, the normal coordinates are transformed into linear combination of themselves. These considerations allow us to have the possibility to classify the eigenvibrations of a molecule according to its irreducible representation of its symmetry group.

C.3 Tetrahedral configuration

In this section, we apply the procedure shown in previous sections to a tetrahedral molecule, shown in Fig. C.1.

A tetrahedron is a polyhedron composed of four triangular faces, six straight edges, and four vertex corners. A regular tetrahedron is one in which all four faces are equilateral triangles, where all faces are the same size and shape and all edges have the same length. We want to study vibrations of a tetrahedron, with one mass in each vertex. The system is in a *(x,y,z)* Cartesian coordinate system. In order to study the normal modes, we imagine that in that tetrahedron there are springs which connect each pair

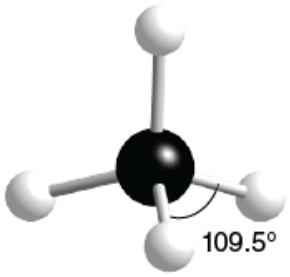

Figure C.1: Schematic picture of an ideal tetrahedron

,

of masses.

Suppose that all the spings are unstretched and of length a at the equilibrium.In addition, suppose that the equilibrium position of the tetrahedron is the particular configuration shown in the Figure C.2, where the coordinates of the four vertices are:

$$\begin{aligned} P_1 &= (\frac{a}{2}, \frac{a}{2}\tan\theta, 0) \qquad P_2 = (\frac{-a}{2}, \frac{a}{2}\tan\theta, 0) \\ P_3 &= (0, \frac{-a}{2}\tan\theta, \frac{a}{2}) \qquad P_4 = (0, \frac{-a}{2}\tan\theta, \frac{-a}{2}) \\ P_5 &= (0, 0, 0) \end{aligned} \tag{C.28}$$

We are assuming that the tetrahedron is centered in the origin of our Cartesian axes and that at the beginning there are no deformations; in this way the angle formed by the edges of the tetrahedron is equal to the ideal one and is 109.5°. As a direct result, the angle formed by the edge of the tetrahedron and the Cartesian axes is equal to $\theta = 35.26°$ for evident geometrical reason.

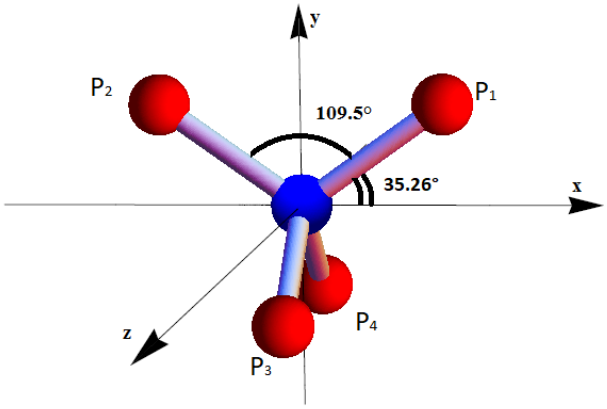

Figure C.2: Equilibrium position of tetrahedron

,

In that description, we imagine that each point is connected to the other four with a springs. The initial length of these springs is the same for all the springs, because in a tetrahedron each point is equidistant from the others.Then, we perturb the system, imaging to "stretch" it , for example, to the right. If we indicate with x_i,y_i and z_i with $i = 1, \ldots, 5$ the deviations from the equilibrium position, looking at Fig. C.2 we have that the vertexes of the tetrahedron have these new coordinates:

$$P_1 = (\frac{a}{2} + x_1, \frac{a}{2}\tan\theta + y_1, z_1) \qquad P_2 = (\frac{-a}{2} + x_2, \frac{a}{2}\tan\theta + y_2, z_2)$$
$$P_3 = (x_3, \frac{-a}{2}\tan\theta + y_3, \frac{a}{2} + z_3) \qquad P_4 = (x_4, \frac{-a}{2}\tan\theta + y_4, \frac{-a}{2} + z_4)$$
$$P_5 = (x_5, y_5, z_5) \tag{C.29}$$

We have to construct the T and V matrices. Let d_{ij} be the distance

between the points P_i and P_j:

$$d_{ij}^2 = (x_j - x_i)^2 + (y_j - y_i)^2 + (z_j - z_i)^2 \tag{C.30}$$

For each pair of points, we have:

$$d_{12}^2 = (-a + x_2 - x_1)^2 + (y_2 - y_1)^2 + (z_2 - z_1)^2 \tag{C.31}$$

$$d_{13}^2 = (\frac{-a}{2} + x_3 - x_1)^2 + (-a\tan\theta + y_3 - y_1)^2 + (\frac{a}{2} + z_3 - z_1)^2 \tag{C.32}$$

$$d_{14}^2 = (\frac{-a}{2} + x_4 - x_1)^2 + (-a\tan\theta + y_4 - y_1)^2 + (\frac{-a}{2} + z_4 - z_1)^2 \tag{C.33}$$

$$d_{15}^2 = (x_5 - \frac{a}{2} - x_1)^2 + (y_5 - \frac{a}{2}\tan\theta - y_1)^2 + (z_5 - z_1)^2 \tag{C.34}$$

$$d_{23}^2 = (\frac{a}{2} + x_3 - x_2)^2 + (-a\tan\theta + y_3 - y_2)^2 + (\frac{a}{2} + z_3 - z_2)^2 \tag{C.35}$$

$$d_{24}^2 = (\frac{a}{2} + x_4 - x_2)^2 + (-a\tan\theta + y_4 - y_2)^2 + (\frac{-a}{2} + z_4 - z_2)^2 \tag{C.36}$$

$$d_{25}^2 = (x_5 + \frac{a}{2} - x_2)^2 + (y_5 - \frac{a}{2}\tan\theta - y_2)^2 + (z_5 - z_2)^2 \tag{C.37}$$

$$d_{34}^2 = (x_4 - x_3)^2 + (y_4 - y_3)^2 + (-a + z_4 - z_3)^2 \tag{C.38}$$

$$d_{35}^2 = (x_5 - x_3)^2 + (y_5 + \frac{a}{2}\tan\theta - y_3)^2 + (z_5 - \frac{a}{2} - z_3)^2 \tag{C.39}$$

$$d_{45}^2 = (x_5 - x_4)^2 + (y_5 + \frac{a}{2}\tan\theta - y_4)^2 + (\frac{a}{2} - z_4)^2 \tag{C.40}$$

The potential energy of the system is given by:

$$\begin{aligned} V &= \frac{1}{2}k[(d_{12}-a)^2+(d_{13}-a)^2+(d_{14}-a)^2+(d_{15}-a)^2 \\ &\quad +(d_{23}-a)^2+(d_{24}-a)^2+(d_{25}-a)^2+(d_{34}-a)^2 \\ &\quad +(d_{35}-a)^2+(d_{45}-a)^2] \end{aligned} \tag{C.41}$$

In order to find the explicit expression of T and V, we neglect higher order terms, because oscillations are small. Therefore, we have to expand all the distances in the potential energy (C.41) to linear order.

We define $\Delta x_{ij} = x_i - x_j$, $\Delta y_{ij} = y_i - y_j$, $\Delta z_{ij} = z_i - z_j$, $i, j = 1, \ldots, 5$ and $i \neq j$. Expansion is made for $\Delta x_{ij} = 0$, $\Delta y_{ij} = 0$ and $\Delta z_{ij} = 0$ because, in our convention, x_i, y_i and z_i are deviation from the equilibrium position. We obtain at the first order:

$$d_{12} = a + x_1 - x_2 \tag{C.42}$$

$$d_{13} = \frac{a(1+2\tan^2\theta) - (x_3 - x_1) - 2\tan\theta(y_3 - y_1) - (z_1 - z_3)}{\sqrt{2(1+2\tan^2\theta)}} \tag{C.43}$$

$$d_{14} = \frac{a(1+2\tan^2\theta) - (x_4 - x_1) - 2\tan\theta(y_4 - y_1) - (z_4 - z_1)}{\sqrt{2(1+2\tan^2\theta)}} \tag{C.44}$$

$$d_{15} = \frac{a(1+\tan^2\theta) - 2(x_5 - x_1) - 2\tan\theta(y_5 - y_1)}{2\sqrt{(1+\tan^2\theta)}} \tag{C.45}$$

$$d_{23} = \frac{a(1+2\tan^2\theta) - (x_2 - x_3) - 2\tan\theta(y_3 - y_2) - (z_2 - z_3)}{\sqrt{2(1+2\tan^2\theta)}} \tag{C.46}$$

$$d_{24} = \frac{a(1+2\tan^2\theta) - (x_2 - x_4) - 2\tan\theta(y_4 - y_2) - (z_4 - z_2)}{\sqrt{2(1+2\tan^2\theta)}} \tag{C.47}$$

$$d_{25} = \frac{a(1+\tan^2\theta) - 2(x_2 - x_5) - 2\tan\theta(y_5 - y_2)}{2\sqrt{(1+\tan^2\theta)}} \tag{C.48}$$

$$d_{34} = a + z_3 - z_4 \tag{C.49}$$

$$d_{35} = \frac{a(1+\tan^2\theta) - 2\tan\theta(y_3 - y_5) - 2(z_5 - z_3)}{2\sqrt{(1+\tan^2\theta)}} \tag{C.50}$$

$$d_{45} = \frac{a(1+\tan^2\theta) - 2\tan\theta(y_4 - y_5) - 2(z_4 - z_5)}{2\sqrt{(1+\tan^2\theta)}} \tag{C.51}$$

Substituting the expansions in the (C.41), we obtain the potential energy at the first order.

Now, we have to construct the V matrix. Defining a set of generalized coordinates:

$$(q_1, q_2, q_3, q_4, q_5, q_6, q_7, q_8, q_9, q_{10}, q_{11}, q_{12}, q_{13}, q_{14}, q_{15}) =$$

$$= (x_1, y_1, z_1, x_2, y_2, z_2, x_3, y_3, z_3, x_4, y_4, z_4, x_5, y_5, z_5)$$

We construct the V matrix (C.16):

$$V_{\sigma\sigma'} = \frac{\partial^2 V}{\partial q_\sigma \partial q_{\sigma'}} \tag{C.52}$$

On the other side, the matrix T is trivial; in fact, from the (C.17) we have that:

$$T = \frac{1}{2} m \sum_{i=1}^{5} (\dot{x}_i^2 + \dot{y}_i^2 + \dot{z}_i^2) \tag{C.53}$$

This implies that

$$T_{ij} = \frac{\partial^2 T}{\partial \dot{x}_i \partial \dot{x}_j} = m\delta_{ij} \tag{C.54}$$

T is a multiple of the unit matrix and then the Eq. (C.23) will be

$$V\vec{\Psi}_\sigma = m\omega^2\vec{\Psi}_\sigma \tag{C.55}$$

We proceed with the Eq. (C.41), substituting in V all the expansions, and then calculating the derivatives that we need in order to construct the matrix elements (C.52) .

We obtain a 15 x 15 matrix, which are valid for a generic angle θ, whose eigenvalues are:

$$\begin{aligned}(0,0,0,0,0,0,5,\frac{2}{1+\tan^2\theta},\frac{4\tan^2\theta}{1+2\tan^2\theta},\\ \frac{3+7\tan^2\theta-\sqrt{9+2\tan^2\theta+9\tan^2\theta}}{2(1+\tan^2\theta)},\frac{3+7\tan^2\theta+\sqrt{9+2\tan^2\theta+9\tan^2\theta}}{2(1+\tan^2\theta)},\\ \frac{5+3\tan^2\theta-\sqrt{5+10\tan^2\theta+9\tan^4\theta}}{2(1+\tan^2\theta)},\frac{5+3\tan^2\theta-\sqrt{5+10\tan^2\theta+9\tan^4\theta}}{2(1+\tan^2\theta)},\\ \frac{5+3\tan^2\theta+\sqrt{5+10\tan^2\theta+9\tan^4\theta)}}{2(1+\tan^2\theta)},\frac{5+3\tan^2\theta+\sqrt{5+10\tan^2\theta+9\tan^4\theta}}{2(1+\tan^2\theta)})\end{aligned} \tag{C.56}$$

In this passage, we assume $k=1$, $m=1$ and $a=1$. Eq. (C.56) represents the frequencies of vibration of a tetrahedral molecule. Substituting the value $\theta = 35,26°$ in (C.56) and looking to a more careful treatment of the theory of the normal modes of a tetrahedron in Ref. [112], we can draw up the following classification:

- the eigenvalue 0 which is six times degenerate and corresponds to rotations and translations;
- the eigenvalue 5, which has no degeneration and corresponds to the

breathing mode ν_1;

- the eigenvalue 0.9989822118044377, which is doubly degenerate and corresponds to the *breathing mode* ν_2;
- the eigenvalue 1.0010177881955622, which is three times degenerate and corresponds to the *stretching mode* ν_3;
- the eigenvalues 3.333656411606072, which is three times degenerate and corresponds to the *bending mode* ν_4.

Excluding the first point, which is relative to translation and rotations, we have nine normal modes, that is coherent with theory, recalling that N=5 and that the number of the degrees of freedom 3N-5 coincide with the number of normal modes. The normal modes are shown in Figure C.3.

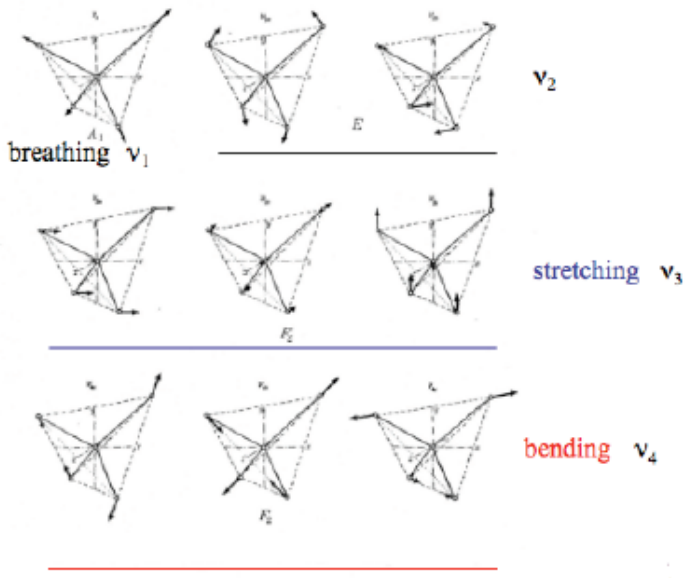

Figure C.3: Normal modes of a tetrahedron. Picture taken from Ref.[112]

Bibliography

[1] P.Fulde, *Correlated Electrons in Quantum Matter*,World Scientific (2012).

[2] M.Lorenz, J.Phys.D: Appl.Phys. **49**, 433001 (2016).

[3] J.Bednorz, K. Muller, Z.Phys. B **64**, 189 (1986).

[4] Y.Tokura, N.Nagaosa, Science **288**,462 (2000).

[5] E.Sela et al., Phys.Rev. B **90**, 035113 (2014).

[6] N.F.Mott, Rev.Mod.Phys.**40**,677 (1968).

[7] P. Fazekas,*Lecture Notes on Electron Correlation and Magnetism* World Scientific (1999).

[8] D.Pesin, L.Balents, Nature Physics **6**, 376 (2010).

[9] W. Witczak-Krempa et al., Annu. Rev. Condens. Matter Phys. **5**, 57 (2014).

[10] H.J. Xiang et al., Phys. Rev. B **75**, 052407 (2007).

[11] R. Arita et al., Phys.Rev.Lett. **108**, 086403 (2012).

[12] H.C.Jiang et al., Phys.Rev. B **83**, 245104 (2011).

[13] S.Raghu et al., Phys.Rev.Lett. **100**, 156401 (2008).

[14] Kargarian et al., Phys.Rev. B **83**, 165112 (2011).

[15] W.Witczak-Krempa, Y.B.Kim, Phys.Rev.B **85**,045124 (2012).

[16] A. Go et al., Phys.Rev.Lett. **109**,066401 (2012).

[17] J.Kim et al., Phys.Rev. Lett. **101**, 076402 (2008).

[18] Y.Singh,P.Gegenwart, Phys. Rev. B **82**,064412 (2010).

[19] S.K.Choi et al., Phys. Rev. Lett. **108**,127204 (2012).

[20] E.J.Cussen et al., Chem.Mater. **18**, 2855 (2006).

[21] T. Aharen et al., Phys.Rev. Lett. **80**,134423 (2009).

[22] Z.Y.Meng et al., Nature **464**, 847-851 (2010).

[23] H.H. Chen, P.M.Levy, Phys.Rev.Lett. **27**, 1383 (1971).

[24] G. Jackeli,G. Khaliullin, Phys. Rev. Lett. **102**, 017205 (2009).

[25] A.Kitaev, Ann.Phys. (NY) **321**,2 (2006).

[26] R.Morrow et al., Scientific Reports **6**, 32462 (2016).

[27] Y.Ueno et al., Phys.Rev.Lett. **111**,087002 (2013).

[28] A.M.Turner et al., Phys.Rev. B **85**, 165120 (2012).

[29] C.K.Chiu,A.P.Schnyder,J. Phys. Conf. Ser. **603**, 012002 (2015).

[30] B.J.Yang et al., Phys. Rev. B **95**,075135 (2017).

[31] J.J.Sakurai, *Advanced quantum mechanics*, Addison Wesley (1967).

[32] S. Blundell, *Magnetism in Condensed Matter*,Oxford University Press (2001).

[33] D.Khomskii, *Transition Metal Compounds*, Cambridge University Press (2014).

[34] C.J.Ballhausen, *Introduction to Ligand Field Theory*,McGraw-Hill (1962).

[35] C.Bradley, A.Cracknell, *The mathematical theory of symmetry in solids: representation theory for point groups and space groups*, Oxford University Press (2010).

[36] E.Pavarini, E.Koch, F.Anders and M. Jarrel, *Correlated Electrons:From Models to Materials Modeling and Simulation* Vol.2, Forschungszentrum Julich, 2012.

[37] S.Sugano, Y.Tanabe, H.Kamimura, *Multiplets of Transition -Metal Ions in Crystals*, Academic Press, London, 1970.

[38] Vamshi Mohan Katukuri,*Quantum chemical approach to spin-orbit excitations and magnetic interactions in iridium oxides*, Appendix A.

[39] A. Abragam,B. Bleaney, *Electronic paramagnetic resonance of transition ions*, Clarendon Press, 1970.

[40] S.Maekawa, T.Tohyama, S.E. Barnes, S. Ishihara, W. Koshibae, G. Khaliullin, *Physics of Transition Metal Oxides*, Springer (2004).

[41] B. Keimer, A. Aharony, A. Auerbach, R. J. Birgeneau, A. Cassanho, Y. Endoh, R. W.Erwin, M. A. Kastner, G. Shirane, Phys. Rev. B **45**, 7430 (1992).

[42] M.W. Haverkort, I.S. Elfimov, L.H. Tjeng,G.A.Sawatzky,A.Damascelli, Phys.Rev. Lett. **101**, 026406 (2008).

[43] G.Q. Liu, V.N. Antonov, O.Jepsen, O.K.Andersen, Phys.Rev.Lett. **101**, 026408 (2008).

[44] C.N. Veenstra et al., Phys.Rev.Lett. **112**,127002 (2014).

[45] A,Georges,L.De Medici, J.Mravlje, Annu. Rev. Condens.Matter Phys. **4**, 137 (2013).

[46] D. Stricker et al., Phys. Rev. Lett. **113**, 087404 (2014).

[47] B. Andlauer, J. Schneider, W. Tolksdorf, Phys. Stat. Sol. B **73**, 533 (1976).

[48] D. Mandrus et al., Phys. Rev. B **63**, 195104 (2001).

[49] Y. G. Shi et al., Phys. Rev. B **80**, 161104 (2009).

[50] J. Yamaura et al., Phys. Rev. Lett. **108**, 247205 (2012).

[51] S. Calder et al., Phys. Rev. Lett. **108**, 257209 (2012).

[52] F.Forte, D. Guerra, A. Avella, C. Autieri, A. Romano, C. Noce, Phys. B **537**,184-187 (2018).

[53] G. Kresse, J.Furthmüller, Computational Materials Science **6**,15 (1996) .

[54] G. Kresse, D. Joubert, Phys. Rev. B *59*,1758 (1999).

[55] H. J. Monkhorst, J. D. Pack, Phys. Rev. B *13*,5188 (1976)

[56] J. P. Perdew, A. Zunger, Phys. Rev. B *23*, 5048 (1981).

[57] D. M. Ceperley, B. J. Alder, Phys. Rev. Lett. *45*, 566 (1980).

[58] P. E. Blöchl, O. Jepsen, O. K. Andersen, Phys. Rev. B *49*,16223 (1994).

[59] N. Marzari, D. Vanderbilt, Phys. Rev. B *56*,12847 (1997).

[60] I. Souza, N. Marzari, D. Vanderbilt, Phys. Rev. B *65*,035109 (2001).

[61] A. A. Mostofi, J. R. Yates, Y.-S. Lee, I. Souza, D. Vanderbilt, N. Marzari, Computer Physics Communications 178, 685 (2008).

[62] V. I. Anisimov, J. Zaanen, O. K. Andersen, Phys. Rev. B *44*,943 (1991).

[63] A. I. Liechtenstein, V. I. Anisimov, J. Zaanen, Phys. Rev. B *52*,R5467 (1995).

[64] Y.J. Song, K.-H. Ahn, K.-W. Lee, W. E. Pickett, Phys. Rev. B **90**, 245117 (2014) .

[65] Z. Hiroi et al., Phys. Rev. B **76**, 014523 (2007).

[66] W. Levason, M. Tajik, M. Webster, J. Chem. Soc., Dalton Trans.,1735 (1985) .

[67] F. Forte, D. Guerra, A. Avella, C. Autieri, A. Romano, C. Noce, Acta Physica Polonica A,394-397 (2018).

[68] A. M. Oles, G. Khaliullin, P. Horsch, L. F. Feiner, Phys. Rev. B **72**, 214431 (2005).

[69] G. Cao, L. De-Long, *Frontiers of 4d- and 5d- Transition Metal Oxides*,World Scientific (2013).

[70] X. Ming, C. Autieri, K. Yamauchi, S. Picozzi, Phys. Rev. B **96**, 205158 (2017).

[71] E. Sasioglu, C. Friedrich, S. Blügel, Phys. Rev. B **83**, 121101 (2011).

[72] Bo Yuan et al., Phys. Rev. B **95**, 235114 (2017).

[73] P.A. Cox, *Transition Metal Oxides, An Introduction to Their Electronic Structure and Properties*,Oxford University Press (1992).

[74] B.F.Phelan et al., Phys.Rev. B **91**, 155117 (2015).

[75] J.Wang, S.C. Zhang, Nature Materials **16**, 1062-1067 (2017).

[76] E.Witten, arXiv:1510.07698v2 (2016).

[77] Z.C. Gu, X.G. Wen, Phys. Rev. B **80**, 155131 (2009).

[78] F.Pollmann et al., Phys.Rev.B **85**, 075125 (2012).

[79] X.Chen et al., Phys.Rev. B **83**, 035107 (2011).

[80] Z.Song, Z. Fang, C.Fang, hys.Rev. Lett. **119**, 246402 (2017).

[81] C.Chiu,J.C.Y.Teo, A.P.Schnyder, S.Ryu, Rev.Mod.Phys. **88**, 035005 (2016).

[82] S.Murakami, New Journal of Physics **9**, 356 (2007).

[83] X.Wan, A.M.Turner, A.Vishwanath, S.Y.Savrasov, Phys. Rev. B **83**, 205101 (2011).

[84] Z.Wang et al., Phys. Rev. B **85**, 195320 (2012).

[85] A.A.Burkov, M.D.Hook, L.Balents, Phys.Rev. B **84**, 235126 (2011).

[86] Y.Chen et al., Nano.Lett. **15**, 6974 (2015).

[87] G.Xu et al., Phys.Rev.Lett. **107**, 186806 (2011).

[88] T.Bzdušek et al., Nature (2016).

[89] J.M.Carter et al., Phys.Rev. B **85**, 115105 (2012).

[90] S.Y. Yang et al., Advances in Physics, **X**, 3:1,1414631 (2018).

[91] S.Murakami et al., Science Advances **3**, 1602680 (2017).

[92] M.Lifshitz, Sovietic Physics Jetp **11**, 5 (1960).

[93] G.E.Volovik , arXiv:1606.08318v6 (2016).

[94] C.Fang et al., Chinese Physics B **25**,117106 (2016).

[95] J.S.Griffith, *The theory of Transition-Metal ions*, Cambridge Press, 1971.

[96] G.Dresselhaus, Phys. Rev. **100**, 580 (1955).

[97] R.Winkler, *Spin orbit coupling effects in two-Dimenional Electron and Hole systems*, Springer (2003).

[98] G.Bihlmayer, *Relativistic effects in solids*, Lecture notes of the 45^{th} IFF Spring School "Computing Solids-Models, ab-initio methods and supercomputing", Forschungszentrum Julich, 2014.

[99] E.I.Rashba, Sov. Phys. Solid State **1**, 368 (1959).

[100] E.I.Rashba, V.I.Sheka, Fiz. Tverd. Tela **2**, 162 (1959).

[101] Y.A. Bychkov, E.I.Rashba, J. Phys.C, Solid State Phys. **17**, 6039 (1984).

[102] Y.A. Bychkov, E.I.Rashba,Sov.Phys. JETP Lett. **39**,78 (1984).

[103] I.E. Dzyaloshinskii, JETP, Vol. **10**, 3 (1959).

[104] T. Moriya, Phys. Rev. **120**,91 (1960).

[105] M.Heide, G.Bihlmayer, S.Blugel, Phys.Rev. B **78**, 140403(R) (2008).

[106] S.Heinze,K.V.Bergmann,G.Bihlmayer, Physik in unserer Zeit **43**, 6 (2012).

[107] B.D.Cullity,C.D.Graham,*Introduction to Magnetic Materials,Second Edition*,Wiley (2009).

[108] P.Löwdin, The Journal of Chemical Physics **19**, 1396 (1951).

[109] G.L.Manni, F.Aquilante, L.Gagliardi, The Journal of Chemical Physics **134**, 034114 (2011).

[110] L.D. Landau, M.Lifshitz, *Course of Theoretical Physics*, Vol.**1**,Elsevier (1976).

[111] L.D. Landau, M.Lifshitz, *Course of Theoretical Physics*, Vol.**3**,Pergamon Press (1973).

[112] G.Herzberg, *Molecular Spectra and molecular structure II*, Van Nostrand Co (1950).